GaN Quantum Dots for Room Temperature Excitonic Physics

Thèse N° 9580

Présentée le 19 juillet 2019

à la Faculté des sciences de base
Laboratoire en semiconducteurs avancés pour la photonique et l'électronique
Programme doctoral en photonique

pour l'obtention du grade de Docteur ès Sciences

par

Sebastian Pascal TAMARIZ KAUFMANN

Acceptée sur proposition du jury

Prof. J.-E. Moser, président du jury
Prof. N. Grandjean, directeur de thèse
Dr H. Mariette, rapporteur
Dr B. Damilano, rapporteur
Prof. E. Matioli, rapporteur

2019

ÉCOLE POLYTECHNIQUE
FÉDÉRALE DE LAUSANNE

An experiment is a question which science poses to nature
and a measurement is a recording of nature's answer.
— Max Planck

Acknowledgements

I am thankful to several persons, without whose help, guidance and support, this work would not have happened. First of all, I would like to acknowledge Nicolas Grandjean for allowing me to join his lab and pursue this adventure. Throughout this work his mentorship motivated me greatly and his guidance helped me staying focused. I am delighted to have learned nitrides from such an outstanding expert in the field. I am also greatful for the flexibility and leeway I enjoyed when performing the experiments. It has been a pleasure to work in LASPE under his tutorship.

I would also like to thank Denis Martin for all the effort he put in developing the growth on silicon and teaching me all the details of the MBE reactor. Thanks to his guidance I was able to prepare the three hundred samples that fueled the thesis. Accordingly, I am grateful to Gordon Callsen for guiding me in all spectroscopic exploits and the understanding in quantum dot optics I gained is hugely due to him. I also recognize Kanako Shojiki for her unfaltering enthusiasm, cheerfulness and determination, I am thankful to have worked with her. I am also indebted to Raphaël Butté and Jean-François Carlin for their scientific feedback.

The LASPE always enjoyed a friendly atmosphere. It was possible through the cheerfulness and amiability of its members to whom I am thankful: Marco, Lorenzo, Joachim, Jean-Michel, Mauro, Jonas, Etienne, Hironori, Wei, Pirouz, Ian, Camille, Hezhi, Thomas, Yao and Johann. A special mention goes to Ian, Camille and Pirouz for the support during dire times and the countless conversations and fun times we spent together. Some of the better moments of my time at EPFL were spent at Sat having long discussions with Pirouz.

Cruzar el atlántico para perseguir la realización profesional implicó, a mi pesar, perderme bodas y momentos importantes con mis amigos y familiares en México. Me entusiasma tener la seguridad que las amistades y lazos son más fuertes que las distancias.

Finally and most importantly I will always be beholden to my family. Their support and love have been the cornerstone of my path.

Lausanne, July 4, 2019

Abstract

Quantum dots (QDs) are the result of quantum confinement in the three spatial directions, as such they exhibit remarkable properties, of which the most important is perhaps the absence of a continuum of states. The allowed energetic levels are discrete, similarly to the energy dispersion in single atoms. As a result, for an individual QD, single photon emission can be achieved. In particular, GaN QDs display an enhanced thermal robustness in comparison to conventional III-V QDs and remain bright even at room temperature. Furthermore, as opposed to other thermally stable QD systems such as colloidal QDs, GaN QDs are epitaxially grown and hence can be easily integrated into photonic devices. However, III-nitride technology is comparatively less mature than traditional III-V QDs and several challenges remain regarding material quality, particularly in terms of structural defects, point defects, and doping of high Al content AlGaN.

With the aim of integrating GaN QDs into photonic nanostructures such as waveguides and cavities based on membrane photonic crystals (PhC), the thesis is oriented towards the development of GaN QDs on thin AlN layers on Si(111). III-nitrides enjoy a high etching selectivity with Si, which allows the fabrication of membrane PhC. The thesis begins by developing high quality AlN on Si(111) and describing the growth of AlN by NH_3-molecular beam epitaxy (MBE) at temperatures above 1000 °C. At the limit between layer by layer and step flow growth, very smooth AlN can be achieved even for thin layers on Si(111). These layers, together with the knowledge acquired in the growth of AlN serve as a stepping stone for the growth of GaN QDs.

GaN QDs have been produced by NH_3-MBE since the first demonstration in 1999 [1], by a modified Stranski-Krastanov (m-SK) growth that relies on a growth interruption. Here we develop the growth of GaN on AlN so that a spontaneous transition into a SK growth occurs. This is analogous to the seminal InAs/GaAs system and as such, the same principles for QD size and density control hold. III-nitrides are often grown heteroepitaxially and the resulting layers have a large threading dislocations density (TDD) (10^9 - 10^{10} cm $^{-2}$). Dislocations offer nucleation centers due to a strain dipole that limits the control over the size and density of the QDs. Then by employing, AlN single crystal substrates with TDD in the order of 10^3 cm $^{-2}$ this limitation is overcome. In this manner, we demonstrate size and density control by varying the amount of deposited GaN and the diffusion length. QD densities ranging from 10^8 to 10^{11} cm^{-2} are achieved. Finally, an approach capable of yielding low QD densities even on highly dislocated

substrates based on ripening and evaporation is presented.
The optical properties of GaN/AlN QDs were investigated. They display high internal quantum efficiencies at 300 K in the order of 40-60 %. The control over the QD size and density is demonstrated by PL measurements. Single QDs are inquired thanks to the possibility of low QD densities. A sample consisting of GaN QDs in AlN on Si(111) was studied in depth. These QDs exhibit multiexcitonic complexes and remain bright even when increasing the temperature to 300 K. At this temperature, single photon emission is revealed by second-order autocorrelation measurements ($g^{(2)}(\tau)$) with $g^{(2)}(0) = 0.17 \pm 0.03$. Finally, GaN QDs are demonstrated to be bright at room temperature with absolute counts in the order of 10^6 s^{-1}.

Résumé

Les boîtes quantiques (BQ) sont le résultat du confinement quantique dans les trois directions de l'espace. Elles présentent des propriétés remarquables, dont la plus importante est peut-être l'apparition de niveaux énergétiques discrets, à l'instar du spectre d'énergie des atomes. Par conséquent, pour une seule BQ, l'émission de photons uniques peut être réalisée. En particulier, les BQ de GaN sont plus résistantes à la température que les BQ III-V conventionnelles et gardent une forte intensité, même à température ambiante. De plus, contrairement à d'autres systèmes de BQ telles que les BQ colloïdales, les BQ de GaN peuvent être crues par épitaxie et peuvent donc être facilement intégrées à des systèmes photoniques. Cependant, la technologie basée sur les nitrures est moins aboutie que la technologie des semiconducteurs III-V traditionnelle. En effet, plusieurs problèmes subsistent concernant la qualité des matériaux. Des améliorations restent à trouver en ce qui concerne les défauts structuraux, les défauts ponctuels ou encore et le dopage de l'AlGaN à haute teneur en Al.

Les nitrures possèdent une forte sélectivité de gravure plasma par rapport au Si permettant la fabrication des crystaux photoniques (CPh) en membranes. Dans le but d'intégrer des BQ GaN dans des nanostructures photoniques, telles que des guides d'ondes et des cavités optiques à base de CPh à membrane, la thèse est orientée vers le développement de BQ de GaN dans des couches minces d'AlN crû sur Si(111). Dans un premier temps, nous présenterons les recherches visant à obtenir de l'AlN sur Si(111) de haute qualité par épitaxie à jet moléculaire (MBE) avec NH_3 à des températures supérieures à 1000°C. Des couches minces d'AlN très lisses peuvent être obtenues sur Si(111) en choisissant des conditions de croissance à la transition entre croissance couche par couche et croissance par avancement de marches atomiques. Ces couches, ainsi que les connaissances acquises dans la croissance de l'AlN, constituent la base nécessaires à la croissance des BQ GaN. Toutes les BQ de GaN produites par NH_3-MBE depuis la première démonstration en 1999 [1] ont été crues par la méthode de Stranski-Krastanov modifiée (m-SK) qui nécessite une interruption de croissance. Ici nous décrivons les conditions de croissance du GaN sur l'AlN indispensables à l'apparition d'une transition spontanée de type SK. Ceci est analogue au système InAs / GaAs et les mêmes principes de contrôle de la taille et de la densité des BQ s'y appliquent. La croissance des nitrures est souvent réalisée de manière hétéroépitaxiale et les couches résultantes présentent une grande densité de dislocations traversantes (DDT) (10^9 - 10^{10} cm^{-2}). Ces dernières offrent des centres de nucleation préférentiels en raison d'un dipôle de contrainte, ce que limite le contrôle de la taille et de

la densité des BQ. Cet obstacle est contourné en employant des substrats monocristallins d'AlN avec une DDT de l'ordre de 10^3 cm^{-2}. Nous démontrons de cette manière la possibilité de contrôler la taille et la densité des BQ en faisant varier la quantité de GaN déposé et la longueur de diffusion. Des densités de BQ s'étalant de 10^8 à 10^{11} cm^{-2} ont pu ainsi être obtenues. Une dernière approche permettant de générer des densités de BQ faibles, même sur des substrats à forte DDT, sera finalement présentée. Elle s'appuie sur la coalescence et l'évaporation des BQ.

Les propriétés optiques des BQ ont été ensuite examinées. Les BQ possèdent un rendement quantique interne à 300 K de l'ordre de 40 à 60%. Le contrôle de la taille et de la densité des BQ est également démontrée par des mesures de PL. Du fait des faibles densités atteintes, les BQ ont par ailleurs pu être individuellement analysées. Un échantillon constitué de BQ de GaN dans de l'AlN sur Si(111) a été étudié en détail. Ces BQ présentent des complexes multiexcitoniques et restent brillantes à température ambiante. Des mesures d'autocorrélation de photons ($g^{(2)}(\tau)$) ont été réalisées à 300 K pour mettre en évidence l'émission de photons uniques avec un $g^{(2)}(0) = 0.17 \pm 0.03$. Enfin, la forte luminosité des BQ à température ambiante a été confirmée, avec des taux d'émission de photons de l'ordre de 10^6 s^{-1}.

List of Acronyms

NH_3-MBE	Ammonia molecular beam epitaxy
a. u.	Arbitrary units
AFM	Atomic force microscopy
BEP	Beam equivalent pressure
XX	Biexciton
CL	Cathodoluminescence
EBL	Electron-beam lithography
X	Exciton
FSS	Fine structure splitting
FWHM	Full width at half maximum
HBT	Hanbury Brown and Twiss
LED	Light emitting diode
μ-PL	Micro-photoluminescence
MOVPE	Metalorganic vapor phase epitaxy
MBE	Molecular beam epitaxy
ML	Monolayer
PA-MBE	Plasma assisted molecular beam epitaxy
PL	Photoluminescence
PhC	Photonic crystal
P^{pz}	Piezoelectric polarization
QCSE	Quantum confined Stark effect
QD	Quantum dot
QW	Quantum well
RHEED	Reflection high-energy electron diffraction
r_{RMS}	Root mean squared surface roughness
P_{sp}	Spontaneous polarization
T_S	Substrate temperature
SEM	Scanning electron microscopy
SPE	Single photon emission
SK	Stranski-Krastanov
TEC	Thermal expansion coefficient

TDD	Threading dislocation density
UV	Ultraviolet
UHV	Ultra high vacuum
WL	Wetting layer
XRD	X-ray diffraction

Contents

1 Introduction

Photonics, the science of light, is nowadays a technologically paramount field due to its cutting edge applications such as lasers, fiber-optics, and electro-optical devices. Photonic devices are used for very diverse purposes: cutting and welding of metals and human tissue with lasers, fiber optics that enable broadband communications, and scientific research such as spectral analysis, among others. So far, all commonplace photonic technologies employ classical light, i.e., they do not take advantage of the quantum nature of the photon. Light itself is quantized, with the elemental minimum packet of electromagnetic radiation being the photon. The photon is massless, yet carries energy and momentum; it is indivisible and obeys the Bose-Einstien statistic.

Harnessing the quantum nature of light sprang the field of quantum optics around the 1960's. During the 1970's, the focus shifted towards photon-counting statistics, which culminated in the prediction and observation of photon antibunching [2]. Recent developments in the fabrication of optoelectronics and integrated photonic circuits have encouraged the pursuit of future photonic quantum communication and computing.

III-nitrides have established themselves as the second most important semiconductors, only behind silicon in market value as a result of the widespread use of light emitting diodes (LEDs) as the supreme general lighting solution. Actually, this success story is very recent and technological applications of III-nitrides have long overshadowed basic research in the field. Such has been the impact of III-nitride optoelectronics that the Royal Swedish Academy of Sciences awarded the 2014 Nobel Prize in Physics to I. Akasaki, H. Amano and S. Nakamura for the invention of the blue LED. The successful realization of high efficiency blue, and hence white, LEDs was mainly driven by an enhancement in the material quality. To this day, crystal growth remains as one of the most prominent aspects of III-nitride research.

In this work, the crystal growth and non-classical optical characteristics of quantum nanostructures based on III-nitrides is explored. The focus of the thesis is centered around the realization and study of GaN quantum dots (QDs), which, as will be demonstrated,

exhibit high efficiency, high operation temperature, and exciting physics.

1.1 III-Nitrides

1.1.1 Crystal structure

When atoms condense into a solid, they will adopt either random positions or ordered patterns known as crystals. Most solid state matter follows a crystalline ordering as it reduces the total energy of the system. At the core of the definition of a crystal lies the principle of translational symmetry, however, further symmetries will largely define the properties of the solid. In a crystal, the atomic lattice in a certain location is identical to any other remote position apart from structural or lattice defects. Crystals can be classified in seven families: cubic, hexagonal, trigonal, tetragonal, orthorhombic, monoclinic and triclinic [3]. III-nitride semiconductors, namely: AlN, GaN and InN and their alloys can crystallize both in a cubic and a hexagonal lattice. In this work, we will focus only on AlN and GaN in their hexagonal structure.

The hexagonal lattice of III-nitrides is the wurtzite crystal structure. It comprises two interpenetrating hexagonal closed packed lattices, each corresponding either to N or Ga(Al) atoms. The hexagonal closed packed lattice implies an A-B-A-B... stacking sequence. The distance between bilayers (AB), u, corresponding to the metal-nitrogen bond length is a useful parameter of the lattice $u \cdot c$. The wurtzite structure can be described by two lattice parameters: a and c which are schematized in figure 1.1. The atoms adopt a covalent bond and a sp^3-hybridization. The first neighbors of each atom form a tetrahedral arrangement. An important consequence of the wurtzite crystal structure and its lack of inversion symmetry is its high anisotropy. The barycenter of the positive and negative charges do not coincide, leading to an electric dipole that results in the so-called spontaneous polarization (P_{sp}) along the c axis. In a perfect wurtzite structure, where all the ions reside on equivalent tetrahedral sites, the ratio of the c and a lattice constants is equal to $c/a = \sqrt{8/3}$ and u has a value of 0.375. However, experimental and theoretical results have proven that in III-nitrides both c/a and u deviate from the ideal values. As a consequence, P_{sp} is enhanced [4]. Heterostructures commonly found in actual III-nitride devices consist in either InGaN/GaN quantum wells (QWs) (LEDs and laser diodes) or GaN channels with AlGaN or InAlN top barriers (electronic devices). In all of these cases, the abrupt change in the material composition will lead to a mismatch in P_{sp} and thus to the appearance of fixed charges at the interfaces. Additionally, when the crystal is subject to strain, piezoelectric effects appear as a result of the anisotropy as discussed hereafter.

The equilibrium a and c lattice constants along with other useful parameters of III-nitrides, such as Varshni coefficients and P_{sp} are summarized in table 1.1. The semi-empirical law of Varshni describes the bandgap as a function of temperature.

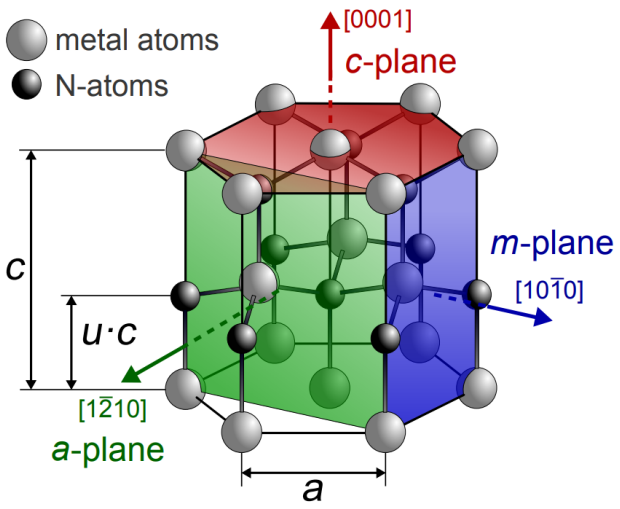

Figure 1.1 – Wurtzite crystal structure of GaN displaying the arrangement of the atoms and the major crystallographic planes and directions. All growths performed in this work were performed along the [0001] direction. Adapted from reference [5].

Due to their covalent bonds, III-nitrides possess a very high mechanical stability. Boasting values for Young's modulus and mechanical hardness of 295 and 15 GPa, respectively, for GaN [6] and 374 and 18 GPa for AlN [7], III-nitrides have become a contender for mechanical applications. For example, AlN has been employed for nanoelectromechanical actuators [8] and to fabricate piezoelectric cantilevers [9].

1.1.2 Band structure and electronic properties

When crystallizing in the wurtzite crystal structure, all III-nitrides enjoy a direct bandgap, i.e. the minimum of the conduction band and the maximum of the valence band are both at the Γ point of the Brillouin zone. For this reason, III-nitrides along with conventional III-V semiconductors such as GaAs, InAs and InP are often used for the realization of light-emitting devices. As illustrated in figure 1.2(a), the direct bandgap of III-nitrides spans from 0.64 to 6.00 eV, thus ranging from the infrared, through the whole visible range and deep into the ultraviolet. Spin-orbit coupling and the hexagonal crystal field in C_{6v} semiconductors result in a valence band splitting into three subbands, see figure 1.2 (b). These are labelled from higher to lower energies as A, B and C bands with symmetries Γ_9, Γ_7 and Γ_7 [13].

The bandgap of ternaries cannot be extrapolated linearly, and a bowing parameter b

Table 1.1 – Basic parameters of III-nitride compounds, all values are from reference [10] except those marked with † and ‡ which come from references [11] and [12], respectively.

Compound	AlN	GaN	InN
a (Å)	3.112	3.189	3.545
c (Å)	4.982	5.185	5.703
u	0.380	0.376	0.377
$\frac{1}{a}\frac{\partial a}{\partial T}$ (10^{-6} K^{-1})	2.9	5.59	3.70
E_g (eV) at 300K	6.00†	3.42	0.64‡
Varshni α (meV/K)	1.799	0.909	0.414‡
Varshni β (K)	1462	830	454‡
P_{sp} (C/m^2)	-0.090	-0.034	-0.042

must be introduced [10]:

$$E_{g,A_{(1-x)}B_{(x)}N}(x) = (1-x)E_g(A) + xE_g(B) - x(1-x)b, \tag{1.1}$$

where the III element is denoted either as A or B. The bowing parameters for InGaN, AlGaN and InAlN are 1.4, 0.7 and 2.5 eV, respectively [10]. To accurately reproduce experimental values of the emission energy, the variation of the bandgap as a function of temperature should also be accounted for, as a first approximation the empirical Varshni formula can be employed:

$$E_g(T) = E_g(0\text{K}) - \frac{\alpha T^2}{T+\beta}. \tag{1.2}$$

1.1.3 Piezoelectric polarization

Due to the lattice mismatch in III-nitrides, all heterostructures will be subjected to strain deformations, with the notable exception of InAlN, which when introducing the proper amount of In (17 %), can be grown lattice-matched to GaN [15]. The deformations due to the lattice mismatch will alter the electronic band structure and hence the bandgap and valence band ordering [4].

The linear bulk piezoelectric polarizations can be obtained for a given strain in the

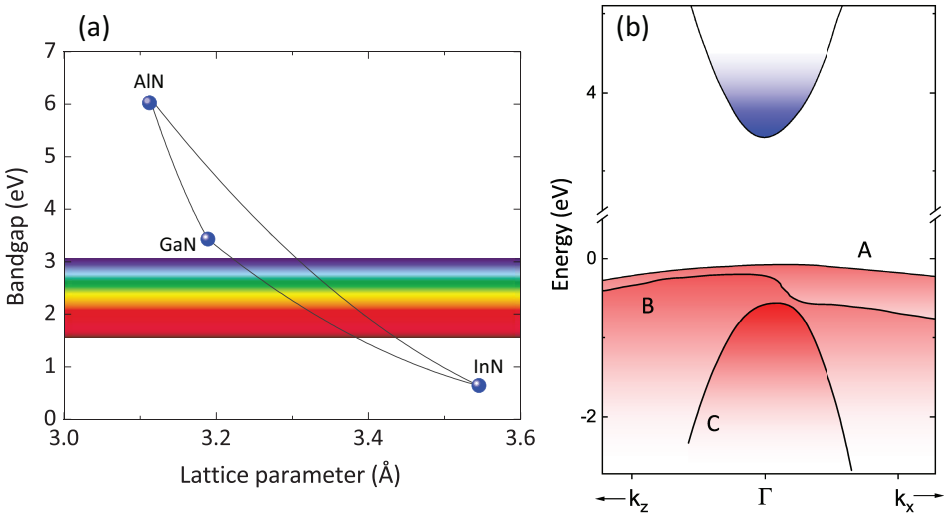

Figure 1.2 – (a) Room temperature bandgap of the binary III-nitrides as a function of in-plane lattice parameter. The lines connecting the dots correspond to equation 1.1 and the corresponding bowing parameters. (b) Band structure near the Γ point of wurtzite GaN. The splitting of the valence band is due to spin-orbit interaction. Based on the results from [14].

material (ϵ_j), where the subindex j represents each dimension, from the formula [16]:

$$P_i^{pz} = \sum_j e_{ij}\epsilon_j, \tag{1.3}$$

where e_{ij} is the piezoelectric tensor and P_i^{pz} the piezoelectric polarization in the i direction. Non-linear piezoelectric effects are also present, nevertheless, this can be accounted for in a compact and accurate manner [17]:

$$\begin{aligned}
P_{AlN}^{pz} &= -1.808\epsilon + 5.624\epsilon^2 \text{ for } \epsilon < 0,\\
P_{AlN}^{pz} &= -1.808\epsilon + 7.888\epsilon^2 \text{ for } \epsilon > 0,\\
P_{GaN}^{pz} &= -0.918\epsilon + 9.541\epsilon^2,\\
P_{InN}^{pz} &= -1.373\epsilon + 7.559\epsilon^2.
\end{aligned} \tag{1.4}$$

The piezoelectric polarization in III-nitrides follows Vegard's law for ternary alloys. Then,

Table 1.2 – Elastic stiffness and piezoelectric constants for III-nitrides. C_{ij} and e_{ij} are in units of GPa and C/m^2, respectively. [21].

Compound	C_{11}	C_{12}	C_{13}	C_{33}	C_{44}	e_{31}	e_{33}	e_{15}
AlN	396	137	108	373	116	-0.53	1.5	-0.48
GaN	390	145	106	398	105	-0.34	0.67	-0.30
InN	223	115	92	224	48	-0.41	0.69	-0.32

the polarization for a ternary III-nitride alloy (with the III element, Al, Ga or In, denoted as A or B) can be calculated using the following expression [18, 17]:

$$P^{pz}_{A_xB_{1-x}N}(x) = xP^{pz}_{AN}[\epsilon(x)] + (1-x)P^{pz}_{BN}[\epsilon(x)]. \tag{1.5}$$

The strain in the layers ϵ_{kl} and the electric field F_k will dictate the elements of the stress tensor σ_{ij} [19, 20]:

$$\sigma_{ij} = \sum_{k,l} C_{ijkl}\epsilon_{kl} - \sum_{k} e_{kij}F_k, \tag{1.6}$$

where the first term corresponds to Hooke's law tensor, with the elastic stiffness C_{ijkl} tensor and e_{kij} is the tensor with the constants for the piezoelectric effect. When applying the wurtzite symmetry (C_{6v}) to equation 1.6, the number of independent or non-zero elements makes the problem more tractable. The matrix notation becomes then a convenient way of displaying equation 1.6 when the C_{6v} symmetry is implemented:

$$\begin{pmatrix}\sigma_1\\ \sigma_2\\ \sigma_3\\ \sigma_4\\ \sigma_5\\ \sigma_6\end{pmatrix} = \begin{pmatrix} C_{11} & C_{12} & C_{13} & 0 & 0 & 0 \\ C_{12} & C_{11} & C_{13} & 0 & 0 & 0 \\ C_{13} & C_{13} & C_{33} & 0 & 0 & 0 \\ 0 & 0 & 0 & C_{44} & 0 & 0 \\ 0 & 0 & 0 & 0 & C_{55} & 0 \\ 0 & 0 & 0 & 0 & 0 & \frac{C_{11}-C_{12}}{2} \end{pmatrix} \cdot \begin{pmatrix}\epsilon_1\\ \epsilon_2\\ \epsilon_3\\ \epsilon_4\\ \epsilon_5\\ \epsilon_6\end{pmatrix} - \begin{pmatrix} 0 & 0 & e_{31} \\ 0 & 0 & e_{31} \\ 0 & 0 & e_{31} \\ 0 & e_{15} & 0 \\ e_{15} & 0 & 0 \\ 0 & 0 & 0 \end{pmatrix} \cdot \begin{pmatrix}F_1\\ F_2\\ F_3\end{pmatrix} \tag{1.7}$$

Here the convention $\sigma_{11} = \sigma 1, \sigma_{22} = \sigma 2...$ has been utilized. The relevant constants for the elastic stiffness C_{ij} and the piezoelectric effect e_{ij} for the binary III-nitrides are given in Table 1.2

1.2 From bulk to zero dimension - Quantum Dots

As will be described in this section, the electronic properties of semiconductors can be influenced by changing the dimensionality of the system, i.e., by confining the electrons and holes in 2D, 1D or 0D potentials. The objective of this section is to give a short description of the physics describing a GaN QD. It does not attempt to establish any solid theoretical framework for actual calculations as this thesis focuses on experimental measurements.

1.2.1 Particle in a box

A qualitative insight into the effects of quantum confinement on the electronic properties of matter is available by revising the fundamental problem in quantum mechanics of a particle in a box. Let us first consider the one dimensional problem of a particle (an electron in the conduction band), trapped in a square potential well of depth $-V_0$ and length $2a$. The solution of the problem will consist in solving Schrödinger's equation for the potential: $V(x) = 0$ for $x \leq \mid a \mid$ [22]:

$$i\hbar\frac{\partial}{\partial t}\phi = (-\frac{\hbar^2}{2m}\nabla^2 + V(x))\phi, \tag{1.8}$$

where m is the mass of the particle. Then, the solutions for $x \geq \mid a \mid$ is the same as the free particle equation:

$$\begin{aligned}\phi_{\mathrm{I}}(x) &= A\mathrm{e}^{\sqrt{2m\mathcal{E}}x/\hbar}, \text{ for } x < -a \\ \phi_{\mathrm{III}}(x) &= B\mathrm{e}^{-\sqrt{2m\mathcal{E}}x/\hbar}, \text{ for } x > a\end{aligned} \tag{1.9}$$

where the coefficients for the growing exponential terms have been set to zero so that the function remains normalizable. For $x < \mid a \mid$ the solutions are of the form:

$$\phi_{\mathrm{II}} = c_1\mathrm{e}^{\mathrm{i}\sqrt{2m(V_0-\mathcal{E})}x/\hbar} + c_2\mathrm{e}^{-\mathrm{i}\sqrt{2m(V_0-\mathcal{E})}x/\hbar} \tag{1.10}$$

and the eigenvalues of the Hamiltonian:

$$\mathcal{E} = V_0 - (k\pi)^2 \frac{\hbar^2}{2ma^2} \quad (k = 0, 1, 2, \ldots) \tag{1.11}$$

This simple model allows us to picture the discrete energy levels for a particle in a finite potential well. Then, by expanding the problem to three dimensions we obtain a first approximation to an electron in a QD. Similarly, discrete energy states will be obtained, for this reason, QDs have been dubbed artificial atoms.

A more realistic description of GaN QDs, should consider the specific geometry of the QD, the Coulomb interaction of the hole and electron (J_{eh}) and the electric field (F). The electric field is perhaps the most difficult to estimate; the strain field will lead to a non-negligible P_{pz} in addition to P_{sp}. The emission energy of the ground state exciton will then be written rather as [23]:

$$X^0 = E_g(\epsilon) + E_z^e + E_z^h + E_r^e + E_r^h + J_{eh} - qh_{QD}F, \tag{1.12}$$

where $E_g(\epsilon)$ is the strain dependent bandgap of the QD material, and $E_{z(r)}^{e(h)}$ is the confinement energy of the electron (e) or the hole (h) along the growth axis $\vec{c}$ (z) or along the plane (r), q is the electric charge and h_{QD} the height of the QD. Two results can already be shown from equation 1.12: the emission energy of the QD will decrease with dot height (h_{QD}) for a fixed aspect ratio and an electric dipole moment is present within the dot (qh_{QD}).

1.2.2 Density of states

A quantity which is crucial for the properties of systems is their density of states. It enters in Fermi's golden rule which allows one to calculate transition probabilities. The density of electronic states (eDOS) of a system describes the number of available states in a given energy interval. The general definition of the density of states is:

$$D(E) = \frac{1}{V} \sum_{n,\vec{k},s} \delta(E - E_{n\vec{k}s}), \tag{1.13}$$

where V is the volume of the crystal, n is the band index, $\vec{k}$ is the wave vector and s is

the spin quantum number. The dispersion relation of the energy $E_{n\vec{k}s}$ will completely determine the functional form of the eDOS. Then, integrating the eDOS over energy up to a given E results in the total number of states per volume below E ($\mathcal{N}(E)$):

$$\int_{-\infty}^{E} D(E')dE' = \mathcal{N}(E). \tag{1.14}$$

As a consequence,

$$D(E) = \frac{d\mathcal{N}(E)}{dE}. \tag{1.15}$$

The previous relationship can be used for calculating the density of states for a given $E_{n\vec{k}s}$. For a bulk crystal with isotropic parabolic dispersion ($E = E_g + \frac{\hbar^2 k^2}{2m^*}$, with m^* being the effective mass) the total number of states can be obtained by integration:

$$\mathcal{N}_{3D}(E) = \frac{2}{(2\pi)^3}\int_0^{k(E)} d^3k = \frac{8\pi}{(2\pi)^3}\int_0^{k(E)} d(k^2)\cdot\frac{k}{2} \tag{1.16}$$

and the magnitude of the wavevector $\vec{k}$ can be written as a function of energy as $k^2 = 2m^*(E - E_g)/\hbar^2$. This will lead to:

$$\mathcal{N}_{3D}(E) = \frac{2}{(2\pi)^3}\left(\frac{2m^*}{\hbar^2}\right)^{3/2}\int_0^{E-E_g}\sqrt{E}dE \tag{1.17}$$

Then the eDOS follows as:

$$D_{3D}(E) = \frac{d\mathcal{N}_{3D}(E)}{dE} = \frac{2}{(2\pi)^2}\left(\frac{2m^*}{\hbar^2}\right)\sqrt{E - E_g}. \tag{1.18}$$

As can be readily seen in equation 1.18, the eDOS is proportional to $\sqrt{E}$ in three dimensions. Reducing the dimensionality of the problem leads to drastic differences in the eDOS, as illustrated in figure 1.3. For instance, for a two-dimensional spin-degenerate parabolic dispersion with in-plane effective mass m^*, the energy dispersion will be given

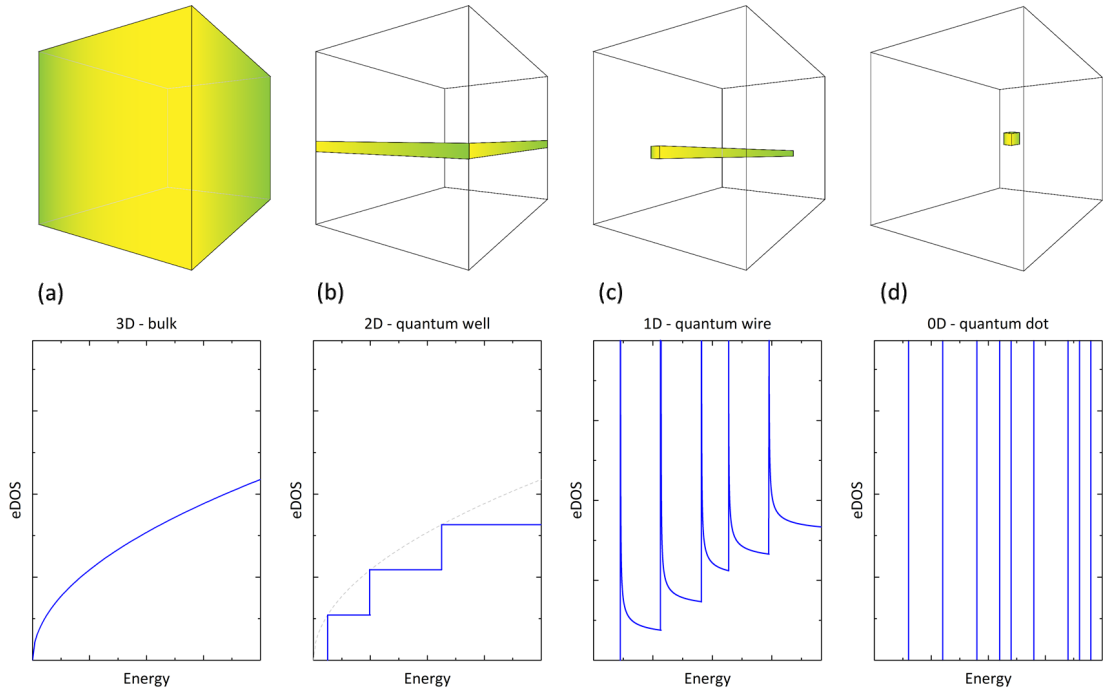

Figure 1.3 – Illustration of confinement from bulk to zero-dimensions and electronic density of states as a function of the confinement potential; (a) bulk semiconductor, (b) quantum well, (c) quantum wire and (d) quantum dot.

by:

$$E_n(k_\parallel) = E_n + \frac{\hbar^2 k_\parallel^2}{2m^*} \tag{1.19}$$

And the corresponding $\mathcal{N}(E)$ by:

$$\mathcal{N}_{2D}(E) = \frac{m^*}{\pi\hbar^2}\int_0^E dE' = \frac{m^*}{\pi\hbar^2}E. \tag{1.20}$$

The resulting eDOS for a two dimensional system with parabolic dispersion is then:

$$D_{2D}(E) = \frac{dN_{2D}(E)}{dE} = \frac{m^*}{\pi\hbar^2} \tag{1.21}$$

For a two dimensional system the eDOS is independent of energy. The result can be

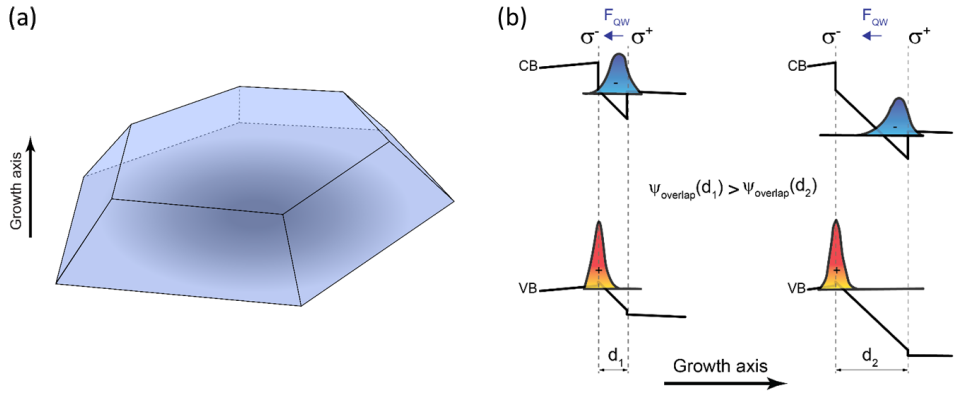

Figure 1.4 – (a) Schematic of a GaN QD, illustrating the truncated hexagonal pyramid shape. (b) Simulation of the conduction and valence band in a III-nitride heterostructure, along with the spatial localization of the electron and hole wavefunctions, courtesy of C. Haller.

expanded for each n so that the eDOS illustrated in figure 1.3 (b) appears. In the zero dimensional case the eDOS will be of the form $D(E) = \frac{1}{V}\delta(E - E_{0D})$ where E_{0D} is discrete.

1.2.3 GaN quantum dots

Due to the atom like eDOS of QDs, extensive research has been directed towards the fabrication and characterization of GaN QDs [24, 25, 26]. Their fabrication often relies on the growth of GaN on AlN and a strain induced morphological transition due to the lattice mismatch [1, 27, 28]. The islanding or transition into a Stranski-Krastanov (SK) growth mode occurs when the strain energy released by the island edges overcomes the surface free energy [29]. In contrast to the InAs/GaAs QDs, GaN/AlN QD layers tend to have a rather high dot density $\sim 10^{11}$ cm^{-2}, which could be useful for optoelectronic devices [30]. Another interesting avenue for GaN QDs is their use as single photon sources [26], for which very low QD densities are required to easily isolate single dots.

GaN QDs adopt the shape of truncated hexagonal pyramids, their diameter is typically in the range of 10-30 nm and their height ranges from a few monolayers (ML) up to 5 nm [31]. A schematic of the shape of a GaN QD is displayed in figure 1.4 (a).

Due to the internal electric field of c-plane oriented III-nitride QDs, the electron and hole wave functions are localized at the top and at the bottom of the QD, respectively [24]. Furthermore, the electric field in the QD will also lead to a huge quantum confined Stark effect (QCSE) which, depending on the QD height, can redshift the emission energy even to 2 eV [1]. The electric field for a GaN/AlN heterostructure can be difficult to quantify, due to carriers and residual doping, and values from 3.8 to 11 MV/cm have

been estimated [32, 33]. In practice, this has the advantage that the emission energy can be easily tuned by changing the height of the QDs and can span the whole visible range [1]. The presence of opposite charges at the interfaces of the heterostructure leads to a band bending with a triangular-shape, as schematized in figure 1.4(b).

Another consequence of the electric field is the reduced spatial overlap of the electron and hole wavefunctions. The oscillator strength (f) is the probability of absorption or emission of a photon in transition energies of an atom, molecule or semiconductor [34]. The oscillator strength of a transition between an excited electron state $|e\rangle$ in the conduction band and a hole in the valence band $|h\rangle$ can be defined by:

$$f \propto |\langle e|h\rangle|^2. \tag{1.22}$$

Then, with an increasing electrical field and hence a decrease in the spatial overlap of the electron and hole wavefunctions, f will also decrease, leading to a smaller probability for photon emission. As illustrated in figure 1.4(b), with an increased QW or QD thickness the overlap will be reduced. Therefore, smaller GaN QD (or thinner QW) are brighter due to an increase in f.

The QCSE will also have an important impact on the linewidths of GaN QDs [35, 36]. Typically, GaN QDs are embedded in an AlN matrix material, which will often contain defects. The defects in turn can stochastically trap and release charges thus providing a wavering electric field [35]. The fluctuating electric field will then shift the emission energy of the QD proportionally to the excitonic electric dipole qh. As a consequence, smaller QDs emitting at higher energies statistically have smaller linewidths than bigger QDs [36]. If the trapping and release time of the charges is shorter than the integration time, GaN QDs linewidths will thus be inhomogeneously broadened. Typical GaN QDs linewidths range from hundreds of μeV, in the best cases, up to several meV [36].

Applications of GaN QDs

GaN QDs have two main avenues of application: as the optically active medium in LEDs and lasers and as single photon emitters (SPE). An important figure of merit in a laser diode is its threshold current; the electrical current necessary for lasing to start. The threshold current depends on temperature and increases exponentially: e^{T/T_0}, where T_0 is the characteristic temperature of the laser. The three dimensional confinement of QDs was proposed to be an advantage for lasers as it drives T_0 to infinity in the ideal case, thus rendering the laser impervious to temperature [37].

An area of research that has grown tremendously in the past decade is the quest for

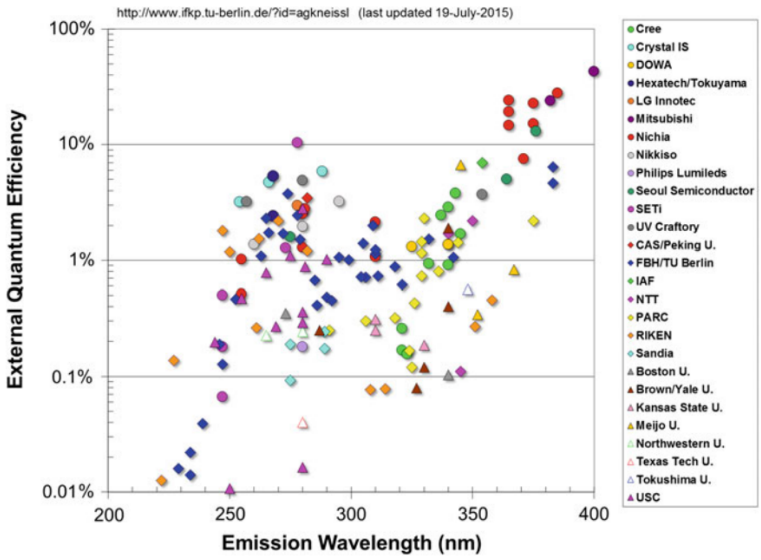

Figure 1.5 – External quantum efficiency of UV LEDs as a function of emission wavelength. Reproduced from [38] with permission from Springer Nature.

efficient ultraviolet LEDs. The number of published journal articles per year containing the keywords "ultraviolet" and "LED" has increased from less than one hundred in 1997 to almost one thousand in 2014 [38]. An interesting trend in UV LEDs is an overall decrease in the external quantum efficiency with decreasing wavelength, see figure 1.5. The data in figure 1.5 corresponds to AlGaN, InAlGaN and InGaN QWs. As was discussed earlier, depending on the size of the GaN QD it is possible to choose the emission energy. In particular, they can be tuned to emit deep in the UV with a high internal quantum efficiency (IQE) as high as 60 % (see chapter 4). Nevertheless, their use in UV LEDs has been limited, in part due to the extreme difficulty for doping AlN [38] and independently controlling the size and density of the QDs [31]. To ease the doping and allow electrical injection, some researchers have sought to grow (Al)GaN QDs on AlGaN instead of AlN [39]. However, due to the smaller lattice mismatch, the critical thickness for the 2D-3D transition from a QW into QDs is much larger [40].

Another promising application of GaN QDs, and objective of the current thesis, is for SPE [26]. Devices emitting single photons are one of the main building blocks for the creation of integrated quantum optics, which could be used for secure quantum communication systems and optical quantum computers [41]. The field of quantum information is centered around the idea of the quantum bit or qubit. In contrast to the classical bit, that can take either a value of 0 or 1, a qubit implements Schrödinger's superposition of states; $|0\rangle$ and $|1\rangle$. Single photons can be used as qubits and full quantum information processing is in principle possible with linear optics [42]. The complete polarization state of a single photon is one instance of such a qubit. Two orthogonal polarization directions can be defined, e.g. horizontal and vertical, as "0" and "1". Then, a diagonally polarized

photon is the analog to Schrödinger's cat: such a photon can be treated as a coherent superposition of "0" and "1" polarization. When measured with a vertical analyzer, the measurement outcome will be with certainty either "0" or "1". As long as the photon is not measured, however, it will linger on in its superposition [43].

An ideal single photon source should provide individual, indistinguishable, photons on demand [44]. Epitaxial QDs based on conventional III-V semiconductors have proven as efficient quantum light emitters due to their scalability and integrability. However, their operation is often limited to cryogenic temperatures [45]. In contrast, GaN QDs have demonstrated SPE up to 350 K [46] and two-photon emission at 50 K based on the biexciton-exciton cascade [47].

1.3 Experimental apparatus

In this section the three main experimental techniques utilized in this work will be reviewed: molecular beam epitaxy (MBE), atomic force microscopy (AFM) and photoluminescence (PL) or micro-photoluminescence (μ-PL). MBE has been used to prepare the samples and AFM and (μ-)PL to characterize them.

1.3.1 Molecular Beam Epitaxy

MBE together with metal organic vapor phase epitaxy (MOVPE) are the two crystal growth techniques that are mostly used for the growth of III-nitride heterostructures. MOVPE enjoys the advantage of being wide spread in the mass production of blue LEDs containing InGaN QWs. However, it lacks several *in situ* real time monitoring techniques found in MBE. In particular, reflection high energy electron diffraction (RHEED) allows real time monitoring of the sample's surface morphology, lattice parameter and growth rate. Actually, several techniques compatible with ultra high vacuum (UHV) have been implemented in MBE, for example: real time scanning tunneling microscopy (STM), tunneling electron microscopy (TEM) and quadrupole mass spectroscopy among others. Because of this reason, MBE is particularly well suited for the study of growth dynamics and phase transitions.

MBE has been used for the growth of advanced epitaxial structures; abrupt or continuous modulations in the composition and doping profiles are possible with a thickness control below the equivalent coverage of one ML. The technique has been extended to several materials families which include: III-nitrides, III-arsenides, III-phosphides, III-antimonides, oxides, magnetic materials and metals [48].

Epitaxy imposes the crystallographic structure, or a similar symmetry, of the substrate onto the growing layer, whereas deposition is referred to the growth of layers with no specific crystallographic relationship to the substrate.

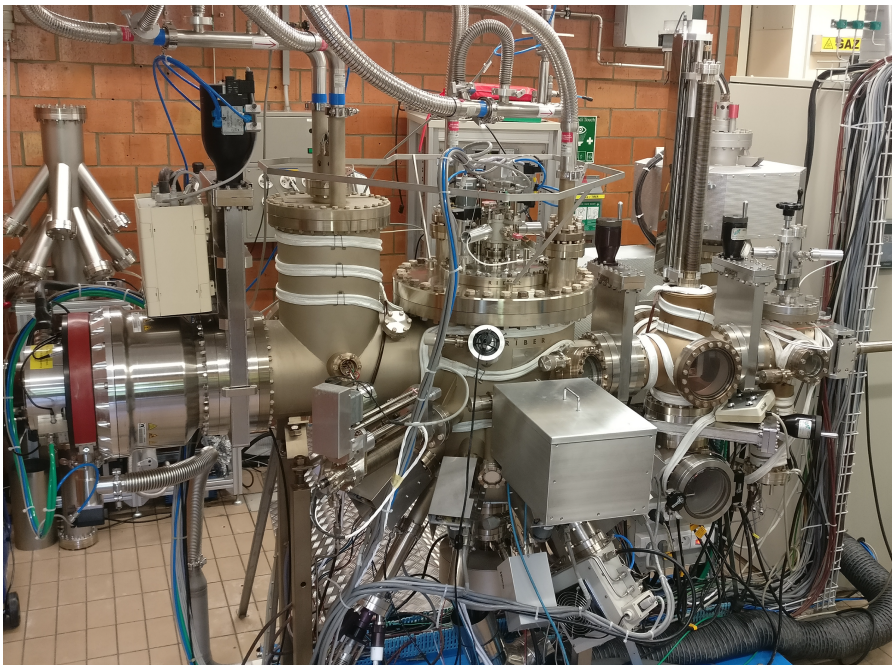

Figure 1.6 – Photography of the MBE system used in this work.

Fundamentals of MBE

The fundamental elements of an MBE system are an UHV chamber ($P \leq 10^{-9}$ Torr), a temperature controlled substrate and non-interacting atomic or molecular beams. The beams are usually achieved by the thermal evaporation or sublimation from ultra pure materials situated in crucibles. The beams are then directed onto the substrate, where the atoms are adsorbed and migrate on the surface until finding suitable vacant lattice sites to incorporate in solid phase. The beams can also be achieved by directly injecting gaseous species in the growth chamber. For the growth of III-nitrides the metallic species can be supplied by effusion cells, whereas N can be provided either by a plasma cell with a N_2 flux or by directly injecting NH_3. In the later case, N is provided by the decomposition of NH_3 at the surface.

A photography of the Riber compact 21 system employed in this work is displayed in figure 1.6. A schematic cross section of the MBE is displayed in figure 1.7 along with some of the elements present in the system.

The UHV of the chamber ensures a long enough mean free path for the atomic species to reach the substrate without any interaction and a minimization of impurities incorporation. Under this regime, atoms and molecules basically do not interact during their paths from the source to the substrate, and mechanical beam shutters can be used to switch on and off the beams. In this manner, the composition of the supplied species can be abruptly changed in times determined by the mechanical shutter operation rate (in the order of

0.1 s).

A quick calculation allows us to confirm that the beams are indeed in the molecular regime. According to the kinetic theory of gases, the mean free path (λ) between collisions of atoms or molecules at a given pressure (p) is:

$$\lambda = \frac{k_B T}{\sqrt{2}\pi p D^2} \tag{1.23}$$

where D is the diameter of atoms or molecules in the beam, T is the temperature of the cell and k_B is Boltzmann's constant. Then, for cell operating at around 1000 K, a molecule size of 2 Å, a beam operating at a pressure of 10^{-4} Torr, $\lambda = 0.5$ m. In comparison, the distance from the sources to the substrate in typical MBE chambers is in the order of 0.2-0.5 m. In fact, it is the pressure in the chamber and hence the mean free path, that sets the upper limit to the amount of gas that can be injected in the chamber when working with gas-source MBE.

Beam sources

The most widely used elements in MBE are metals from group III, namely: aluminum, gallium and indium. For these elements, solid source effusion cells are commonly utilized. The crucibles are often made of high-purity pyrolitic boron nitride or graphite. The crucibles are radiatively heated by Ta filaments, and the temperature is measured by a thermocouple. In order to achieve stable cell temperatures the electrical current in the filament is handled by a proportional integral derivative (PID) controller in closed loop with the thermocouple. Following Knudsen and Langmuir's theory of evaporation [49, 50], the flux (Φ) from an effusion cell in UHV can be calculated as:

$$\Phi = A_e p(T) \sqrt{\frac{N_A}{2\pi M k_B T}}, \tag{1.24}$$

where N_A is Avogadro's number, M is the molecular weight, and $p(T)$ is the equilibrium pressure of the evaporant. In practice, the fluxes are given in terms of beam equivalent pressure (BEP). BEPs are readily measurable in an MBE system by positioning a pressure gauge (a hot filament ionization gauge is used in our system) at the substrate position and directly measuring the pressure due to the beam. The procedure allows for accurate calibration of the cell's fluxes and thereby growth rates. A schematic illustration of an effusion cell is displayed in figure 1.8.

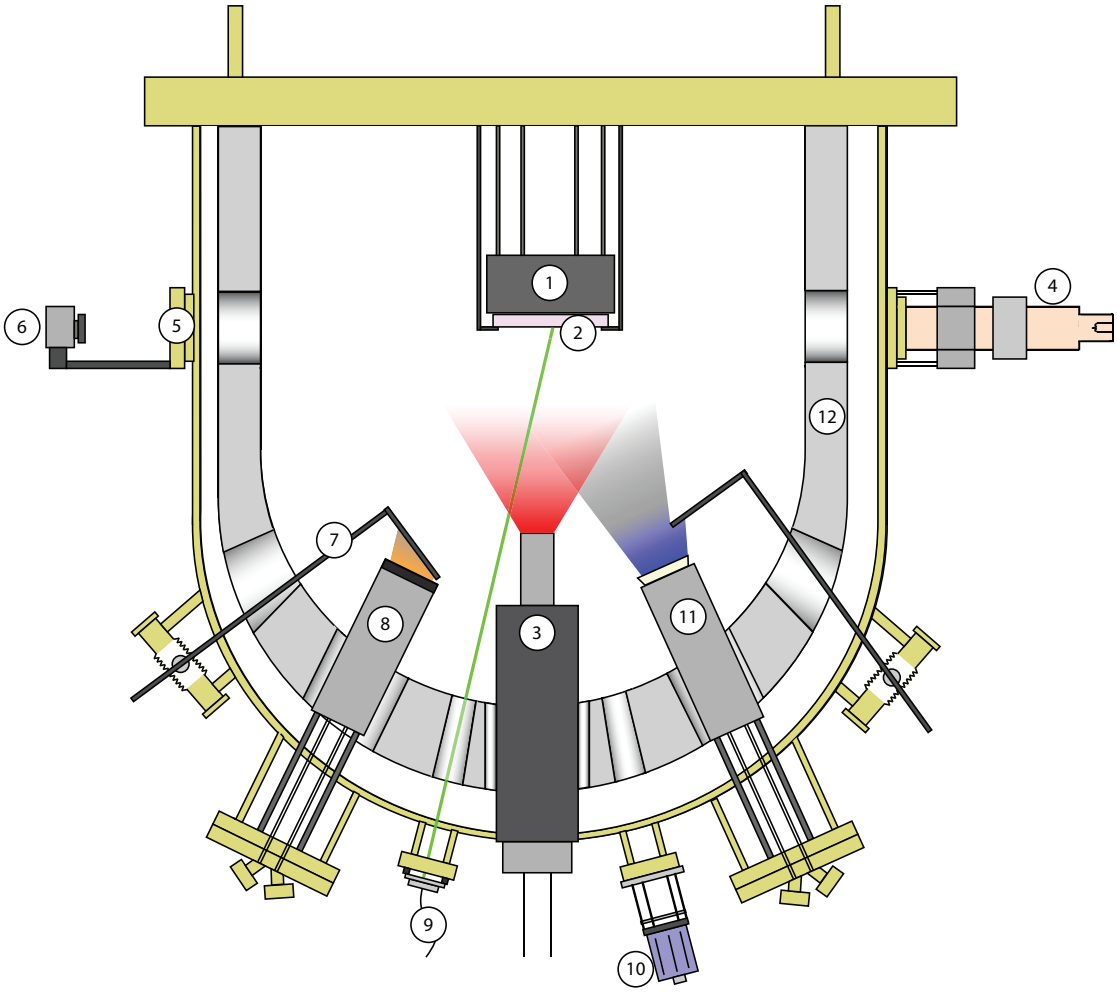

Figure 1.7 – Schematic cross section of the MBE system used in this work. The elements depicted are: 1. Substrate heater and thermocouple. 2. Molybdenum sample holder. 3. NH_3 injector. 4. RHEED electron gun. 5. RHEED phosphor screen. 6. High sensitivity camera. 7. Cell shutter. 8. Double filament Ga cell. 9. Laser reflectivity. 10. Pyrometer. 11. Cold lip Al cell. 12. Liquid N_2 cryopanels.

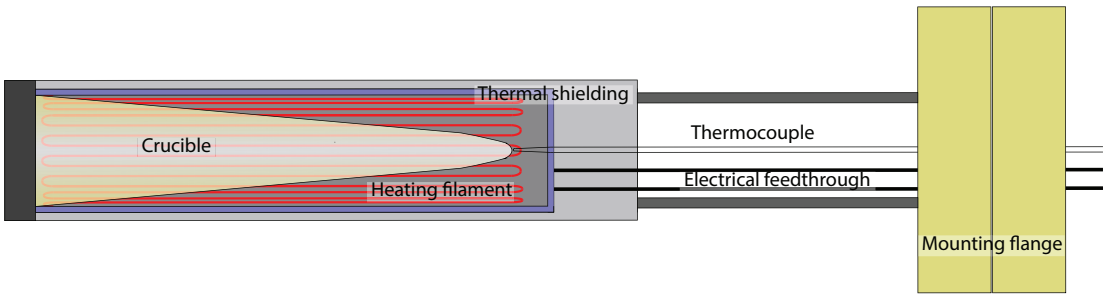

Figure 1.8 – Schematic cross section of a conventional solid source effusion cell.

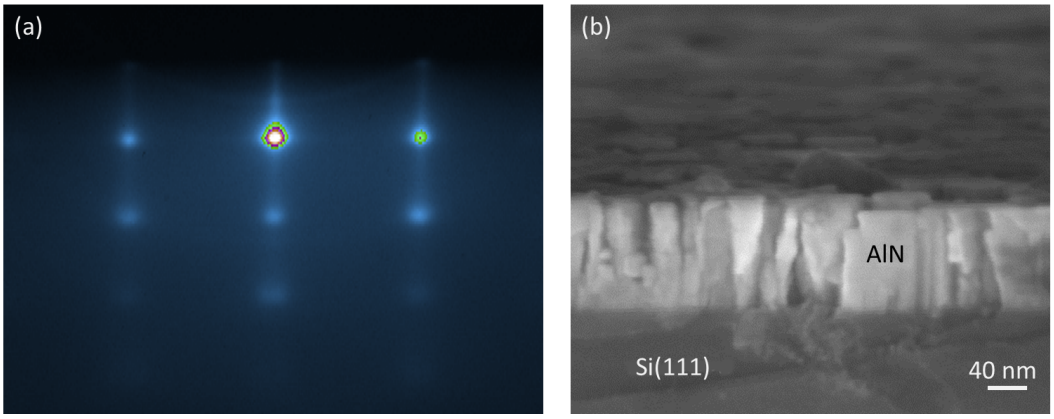

Figure 1.9 – (a) RHEED pattern of 100 nm of AlN on Si(111), (b) cross section SEM image demonstrating the columnar growth (5° tilted), courtesy of I. Rousseau.

Reflection high-energy electron diffraction

RHEED is perhaps the most distinguished and widespread *in situ* diagnostic technique employed in MBE. The technique operates a collimated beam of electrons with energies in the range of 10-50 keV and a fluorescent screen with which the diffracted electrons are detected. The MBE system utilized in this work relied on an electron gun operated with an accelaration voltage of 15 keV. The diffraction patterns are then visualy inspected or analyzed by an image processing software. As the name implies, the beam is operated in a reflection geometry with a grazing angle of 0.5 to 2.0 °. Due to the low angle of incidence and the high accelaration voltage, the electron beam's depth of probe is only a few MLs.

Constructive interference will be given by the intersection of the reciprocal lattice and the Ewald sphere. Then the diffraction pattern will consist of almost circular spots for a perfect surface. It should be noted that in the case of electron diffraction (as opposed to X-ray diffraction) the radius of the Ewald sphere is much larger than the distance between reciprocal lattice sites and the Ewald sphere has a finite thickness due to the energy spread of the electrons [48]. For a rough surface with a reciprocal lattice consisting of dots, the intersection with the Ewald sphere happens at several locations, hence, the RHEED patter will consist of spots, as illustrated in figure 1.9. When the surface is rough, the electrons will be diffracted by the bulk material and the reciprocal lattice is then composed of dots.

For smooth surface, strain inhomogeneities and disorder at the surface will lead to either thick rods (highly inhomogeneous) or thin lines (highly homogeneous) in the reciprocal lattice. As a result, the intersection with the Ewald sphere will be more or less localized. As an example, the RHEED pattern of AlN on Si(111) (highly inhomogenous) AlN on *c*-plane sapphire template and AlN single crystal (highly homogeneous) are presented in figure 1.10. Notice that as the surface ordering is increased, the vertical spread of the

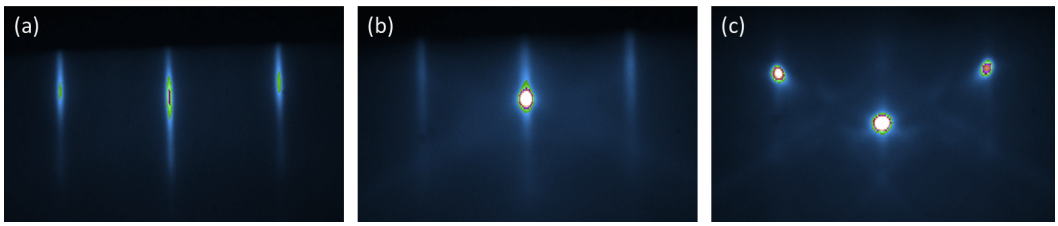

Figure 1.10 – RHEED pattern of (a) 200 nm of AlN on Si(111), (b) 1 μm of AlN on sapphire and (c) AlN single crystal substrate.

diffracted beam on the screen gets narrower.

Another useful application of RHEED in an MBE environment is its ability to evaluate the growth rate and the growth mode. Given a set of growth parameters that lead to a layer by layer growth mode, the intensity of the RHEED specular beam will oscillate proportionally to the surface coverage of the growing species. It has been shown that the period of oscillations corresponds to the period required to grow a 1 ML thick layer; 0.249 nm for AlN and 0.259 nm for GaN [51]. The condition for RHEED oscillations is the formation of ML thick islands that roughen the surface and scatter the incident electrons. However, if the growth conditions are set for a step flow growth mode, which can be usually achieved by raising the substrate temperature, no oscillations will be visible as there is no island formation and hence no roughening of the surface. Thanks to *in situ* measurement of growth rates, provided sticking coefficients ~ 1, alloy compositions can be directly accessed by comparing the relative growth rates of the species.

RHEED also provides access to the lattice parameter in real time, since the diffraction conditions given by the reciprocal lattice (k) are proportional to the lattice parameter: $k \propto 1/a$. Monitoring of the lattice parameter during growth is particularly useful when growing lattice mismatched materials, the relaxation rate and critical thickness can be directly measured [52, 53]. The monitoring of the lattice parameter, together with the surface roughening makes RHEED an excellent tool to monitor *in situ*, in real time the transition of the growth mode from layer by layer into 3D islands and hence is ideally suited for the study of the growth of QDs.

Growth modes

Three growth modes can be differentiated during epitaxy. These are: the Volmer-Weber mode (VW), the Frank van der Merwe mode (FM) and the SK mode. The growth mode of the epitaxial film will depend on the lattice mismatch between the substrate and the film, the supersaturation of the crystallizing phase, the growth temperature and the adhesion energy [54].

In the VW mode, or pure island growth all the nucleation happens in small clusters

of directly nucleated material that form islands in the condensed phase. The atoms or molecules of the deposit are strongly bound to each other, than to the substrate. This mode is often found in metals growing on insulators. In the FM mode, the adatoms condense to form complete MLs on the surface and no island thicker than a ML is observed. This growth mode is also called layer-by-layer. In the case of a lattice mismatch between the substrate and the epitaxial material, strain release will take place in the form of extended defects: dislocations. The SK mode is characterized by an intermediate regime between FM and VW growth modes and is commonly observed in lattice mismatched systems. After proceeding in FM mode up to a certain critical thickness, the strain is released by the formation of 3D islands on top of the 2D layer, which is called the wetting layer (WL) [54].

The FM mode can be divided into layer by layer or step flow mode. The step flow mode is often seen in high quality homoepitaxial growth when the substrate is slightly miscut from the index plane. If the diffusion length of the adatoms on the surface is at least half of the average atomic step width, the growth will proceed in a step flow mode. In this case all the nucleation proceeds at the edge of the atomic steps, and the growth occurs by the motion of steps along the terraces. The step flow growth mode is particularly interesting when aiming at epitaxial films with extremely low surface roughness.

1.3.2 Atomic Force Microscopy

AFM is perhaps the best suited technique to study the topography of a surface, in the best case with atomic resolution. Before the AFM was invented and implemented in 1986 [55], it was preceeded by the scanning tunneling microscope (STM) in the early 1980's, for which the Nobel Prize for Physics was awarded.

An AFM consists of a cantilever (used as mechanical resonator) with a sharp tip at its end, which is approached to the surface of the sample and the surface is rastered. The AFM used in this work was operated in the so-called tapping mode, where the tip oscillates in the z-direction (perpendicular to the sample surface). The oscillations are driven by a piezoactuator to which the cantilever is attached and the cantilever is driven at its resonant frequency or close to it. As the tip approaches the surface, the attractive force between the tip and the sample due to a Van der Waals force will shift the resonance frequency of the cantilever and hence the amplitude of the oscillations. A laser is directed on the top of the cantilever, from where it is reflected on to a photodiode. The photodiode then detects the amplitude and the frequency of the oscillation. Finally, the sample is held in place on top of a XYZ piezostage. The piezostage will move the sample in order to raster the surface and the movement of the piezostage is used to reconstruct the topography of the surface.

The quality of an AFM image will be mostly determined by the performance of the tip.

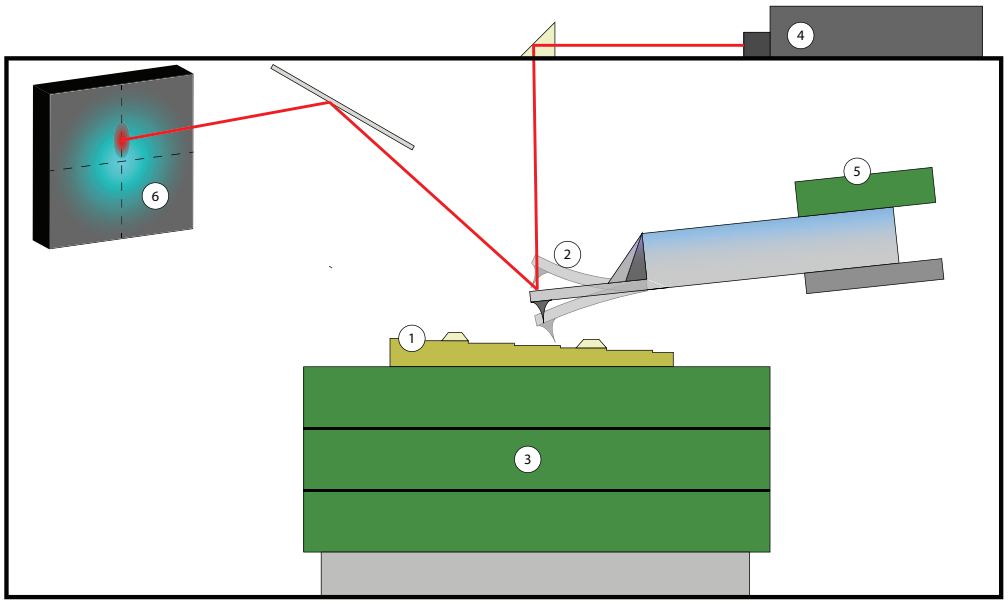

Figure 1.11 – Schematic of the AFM used in this work. The elements depicted are: 1. Sample. 2. Cantilever and tip. 3. XYZ piezoelectric stage. 4. Laser. 5. Tip piezoactuator. 6. Photodiode.

In this work two types of AFM tips were employed: the OTESPA-R3 from Bruker or the SuperSharpSilicon from Nanosensors. Both consist of Si cantilevers and an Al coating on the backside to enhance laser reflection. The cantilevers have typical resonant frequencies of 200 to 500 kHz and force constants in the order of 10-100 N/m. The notable difference between the AFM probes is the sharpness of the tip. The suppliers claim typical tip radius of 7 nm and 2 nm for the Bruker and Nanosensors tips, respectively. Atomic terraces can be imaged with both types of AFM tips. However, when lateral resolution is also important as for instance when measuring QDs, the Nanosensors tips are superior.

1.3.3 Photoluminescence and micro-Photoluminescence

PL is based on the absorption of high energy photons, followed by the reemission of photons at lower energies. During this process, electrons in the valence band are excited to the conduction band by the incoming photons and then decay to their ground state. The energy of the outgoing photons will be determined by the band structure or by the energy of localized states like impurities or QDs. Two setups have been used through this work to investigate the optical signature of GaN QDs: either a PL setup, with a spot size in the order of a hundred μm where an ensemble of QDs is probed or a micro-photoluminescence setup (μ-PL) where the spot size can be reduced to about 500 nm and for which single QDs can be investigated. Although the physical principle is exactly the same, μ-PL imposes a more severe technical complexity.

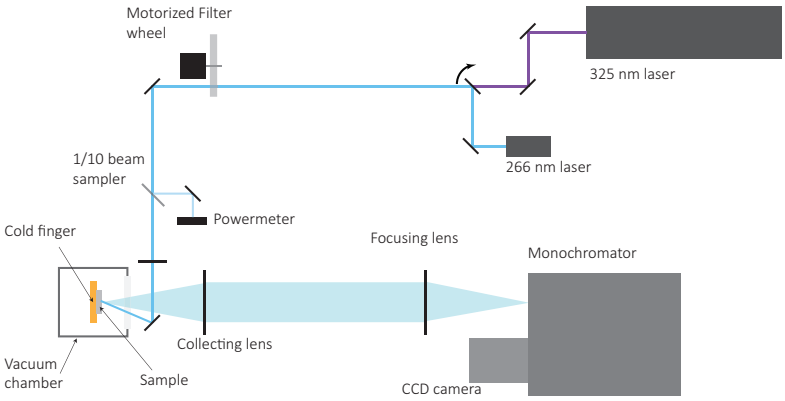

Figure 1.12 – Schematic of the PL setup used in this work. Courtesy of C. Haller

The PL setup consists of several lasers, most of them in the UV. The selected laser is focused on to the sample by a 30 cm focal length lens and the output signal collected by a set of lenses and focused onto the slit of a 32 cm monochromator and a Peltier cooled CCD. The sample is mounted in a closed cycle cryostat capable of reaching 10 K. The setup offers the possibility of temperature, power and polarization dependent measurements for a variety of excitation sources. Depending on the QD size, their emission energy can be located deep in the UV, for this reason, the PL experiments presented in this work were done with a pulsed 266 nm laser. A schematic of the setup and its elements is depicted in figure 1.12.

The μ-PL setup consists of deep UV lasers focused onto the sample by a 80X plan UV microscope objective (NA = 0.55). Two, different deep UV continous wave lasers have been used in this work: a 100 mW frequency quadrupled Nd:YAG laser operating at 266 nm and a 70 mW frequency doubled solid state laser at 244 nm. The sample is cooled by a closed cycle cryostat capable of reaching 4 K, the sample can be positioned by means of a three axis piezostage with a high mechanical stability. The sample chamber can be operated in vacuum or in controlled atmospheres of O_2 or N_2. For mapping and fine laser positioning the sample is held immobile with the sample piezostage in closed loop and the microscope objective is precisely positioned using an additional piezostage.

In order to maximize the PL signal, a 90:10 transmission to reflection beam sampler was used. The signal can be routed onto two different detection arms. The first consists of a 64 cm single monochromator and a liquid N_2 cooled CCD. The other detection arm consists of a 27 cm monochromator with an output onto a Hanbury Brown and Twiss (HBT) interferometer. A schematic and a photography of the μ-PL setup are depicted in figure 1.13 and 1.14, respectively.

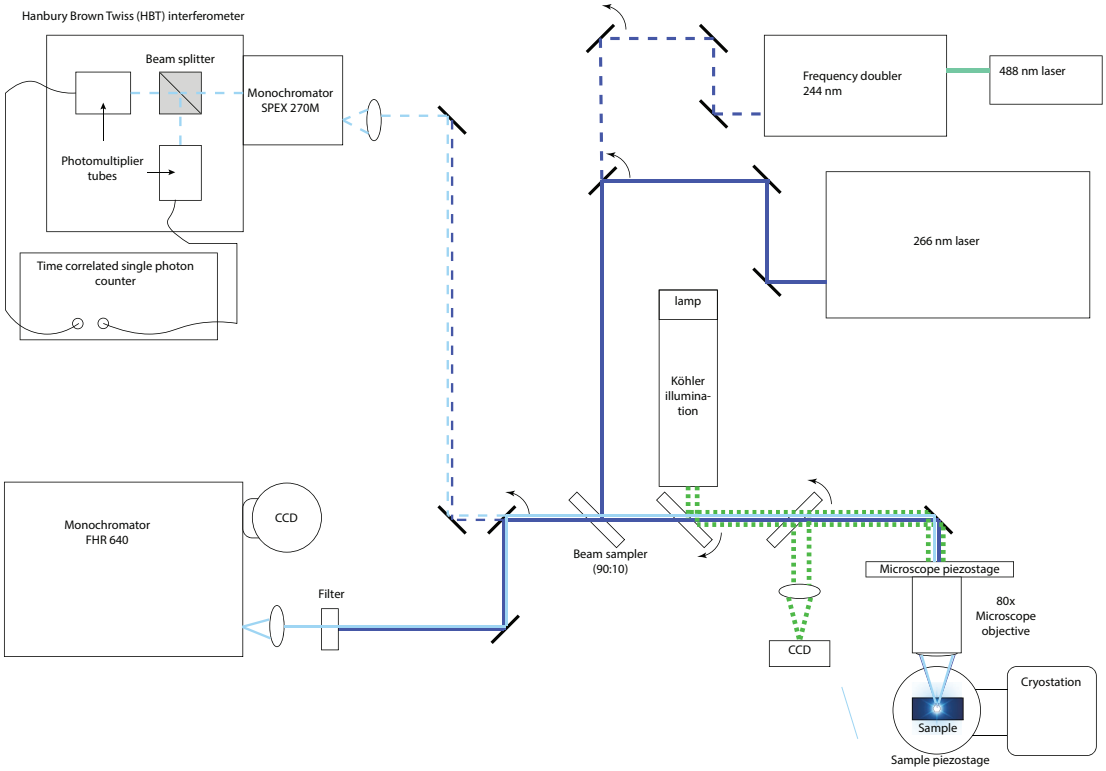

Figure 1.13 – Schematic of the μ-PL setup used in this work. Curved arrows denote temporarily removable elements in the setup and dashed lines represent alternative signal paths.

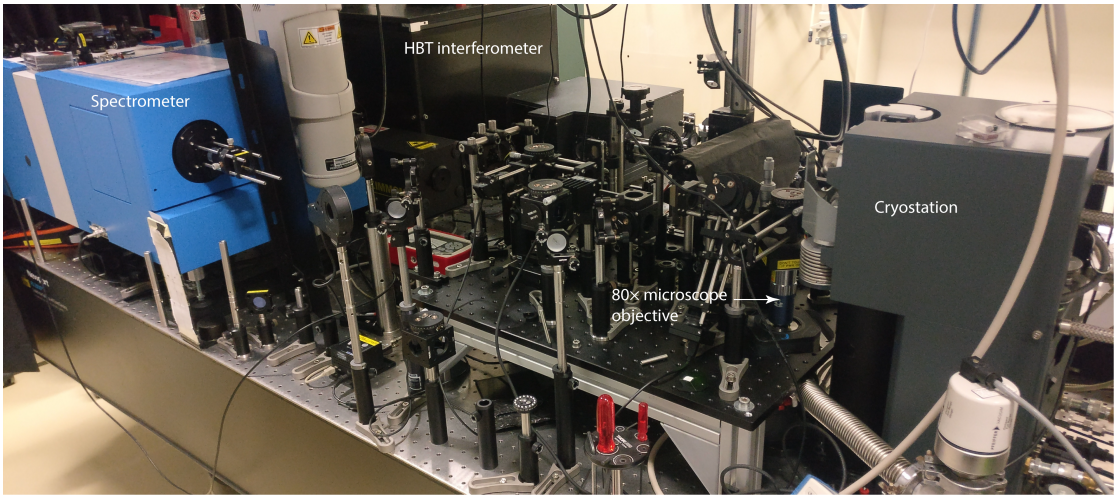

Figure 1.14 – Photography of the μ-PL setup used in this work.

Second order autocorrelation function - photon statistics

The HBT interferometer consists of a monochromator used to spectrally select the investigated QD. The light is then sent into a fused silica 50:50 beam splitter. At each of the arms of the beam splitter, photomultiplier tubes (PMT) are used as detectors. The detection events are time correlated by a Picoharp 300 which records the photon's arrival times. A first arrival at any of the detectors starts an internal watch in the time correlator and is stopped with the arrival of a photon at the other PMT. A histogram of the delay time between detections is built, which is known as the second order autocorrelation function or $g^{(2)}(\tau)$, where τ is the time delay. Mathematically, $g^{(2)}(\tau)$ can be expressed as [26]:

$$g^{(2)}(\tau) = \frac{\langle I(t) \cdot I(t+\tau) \rangle}{\langle I(t) \rangle^2}, \tag{1.25}$$

where, $I(t+\tau)$ is the intensity operator at a time t and a delay τ. For $\tau = 0$, a $g^{(2)}(0) < 0.5$ implies a single photon source. However, an ideal single photon source would give $g^{(2)}(0) = 0$. SPE and photon statistics are disscussed in detail in chapter 4, section 4.6.1. One of the main challenge in the practical implementation of an ideal single photon source is the background emission from other light sources in the sample. Background emission is a significant problem in III-nitride quantum structures [26]. For this reason, some reports achieve reasonable $g^{(2)}(0)$ when subtracting the background during post experiment analysis. Nevertheless, practical single photon sources require "uncontaminated" emission and thus uncorrected $g^{(2)}(0)$ value is the relevant figure of merit [26].

2 AlN on Si(111)

The crystal growth of III-nitrides constitutes one of the primary challenges for the development of III-nitride devices. Due to their high melting point and equilibrium pressure, the Czochralski process is not possible. The Czochralski process, invented in 1913 by the Polish researcher Jan Czochralski, is today the most widespread technique for the growth of defect free, large scale, single crystals of silicon, germanium, gallium arsenide and more recently gallium oxide [56]. There has been considerable progress in the field of III-nitride substrate fabrication; for instance, so called "free-standing" GaN substrates with TDD in the order of 10^6 cm^{-2} are commercially available. These rely initially on GaN on sapphire layers, then the surface is masked except for some apertures where further growth is allowed to take place. Finally a regrowth is performed on the apertures and the layer eventually coalesces by epitaxial lateral overgrowth. The laterally overgrown material does not have structural defects such as dislocations [57]. Recently, high quality AlN substrates have become available. The technique relies on a small seed of AlN crystal which is then transformed into macroscopic wafer size crystals by physical vapor transport [58]. Such AlN substrates exhibit TDDs as low as 10^3 cm^{-2}. Nevertheless, the vast majority of III-nitride scientific studies and industrial applications rely on heteroepitaxially grown material. The most commonly used substrates are sapphire, Si(111) and SiC. Silicon is particularly interesting due to its low cost, high thermal conductivity and high etching selectivity. Low substrate price and high thermal conductivity have made silicon substrates interesting for the growth of high power, high frequency electronics [59, 60]. Additionally, the high etching selectivity between nitrides and silicon has allowed the fabrication of PhC membranes and nanobeams [61, 62, 63, 64], that allow for the engineering of the propagation of light and the enhancement of the spontaneous emission via the Purcell effect.

In this chapter, we will discuss the growth of AlN on Si(111) by NH_3-MBE, with the objective of achieving PhCs and possibly inserting of GaN QDs in the optical cavities. The wavelength at which the PhC operates implies a thickness constraint to the monomode. Therefore, strategies that use thick overgrowth and strain engineering layers to improve

the crystal quality and prevent cracks cannot be implemented. Although, the present study is centered around the study of thin AlN on Si(111) layers, in the order of a hundred nanometers, the first layer of AlN on Si(111) is fundamental on the crystal quality of any subsequent heterostructure and hence on device performance [65, 60, 66].

The growth of III-nitrides on Si(111) is particularly challenging. The lattice mismatch, that amounts to 19% between AlN and Si(111), implies that a misfit dislocation is created every 5 lattice spacings [67], and thus layers with high dislocation densities are obtained. In addition, the thermal expansion coefficient (TEC) of Si is twice that of AlN, which can lead to extreme stress in the layer during cooldown from growth temperature to room temperature and eventually to cracks [68]. Furthermore, the clean surface of Si is extremely delicate, as it is reactive with NH_3 and unstable against Ga [69]. Nevertheless, it is possible to grow III-nitrides on Si by using an AlN buffer layer and thus shielding the Si surface from Ga. Also, the strain in GaN due to the difference in TEC can be compensated by AlN interlayers [69]. Hence the GaN is in compressive strain and compensates for the tensile strain which builds up during cool down.

The objective for the growth of AlN on Si(111) was to minimize the surface roughness and to maximize the structural quality of the layers, while keeping a total thickness in the order of 100 nm. The highlights and main results of the chapter were published in the Journal of Crystal Growth [70].

2.1 State of the art

The first demonstration of AlN on Si(111) dates back to over four decades [71]. Then, together with the general trend of III-nitrides, very limited research was carried out until the beginning of the 1990's. It was towards the end of the decade, that full LEDs [72] and AlGaN/GaN heterostructures [59] grown on Si were reported. Two major challenges were identified: the high chemical reactivity of the Si substrate to most species and the huge difference in TEC that leads to cracking of thick films [73, 68]. The former issue has been solved by growing an intermediate layer between the GaN and the Si substrate. Even if AlN has been the most succesful, several other approaches have been explored: GaAs [74], AlAs [75] and SiC [76]. The issue of cracking due to the difference of TEC, has been also succesfully solved by growing GaN under compressive stress; AlN has a smaller in-plane lattice paramater than GaN, namely, 0.311 and 0.318 nm, respectively. When growing GaN on AlN, GaN will tend to adopt the lattice parameter of AlN and therefore the layer will be under compressive strain [73]. However, dislocations decrease the compressive strain [77], thus reducing the dislocation density of the AlN film is of utmost importance to achieve crack-free thick GaN layers on Si.

Specifically for MBE, the first reports discussing the growth of AlN on Si(111) for both plasma-assisted MBE as well as gas source MBE appeared at the end of the 1990's

[78, 79, 80]. Among the key steps towards high quality III-nitrides on Si is the nucleation layer [81, 82, 83, 84, 85, 86]. In this work we have used the approach suggested by F. Semond *et al.* [60] and further studied by A. LeLouarn *et al.* [86].

2.2 Steps in the growth of AlN on Si

All Si surfaces exposed to the ambient atmosphere oxidate. The resulting native oxide is amorphous and hence prevents any epitaxial growth. The first step in the growth is therefore the removal of the native oxide. This can be obtained either *ex situ* by chemical etching in HF or *in situ* by annealing the substrate under vacuum at high temperature.

Following the removal of the native oxide a nucleation layer is created. The nucleation layer has been widely studied and plays a fundamental role in the quality of the resulting layer. Two approaches can be found in the literature to treat the nucleation layer. Some researchers suggest exposing the clean Si surface to Al first is essential for a sharp interface [68], whereas others found that a dose of NH_3 leads to an improved layer quality [86].

Once the nucleation layer is optimized, the growth of AlN can be started by supplying NH_3 and Al and ramping the substrate temperature to the desired value. As will be shown later, the V/III ratio and the substrate temperature during the growth of AlN on Si by NH_3-MBE is critical for achieving flat surfaces and high crystal qualities.

2.3 Preliminary results

At the beginning of this work, a recipe for the growth of AlN on Si(111) was implemented following the results described by Semond *et al.* [60]. It consisted in degassing the substrate at 600 °C for 10 hours. At this stage, the RHEED pattern is blurry due to the presence of the native oxide on the surface (Fig. 2.1(a)). Then, the native oxide is removed by annealing the Si substrates in the growth chamber. At a substrate temperature of around 900 °C,[1] the RHEED pattern increases drastically in intensity due to the removal of the native oxide (Fig. 2.1(b)). Then, when cooling the substrate below 830 °C the (7×7) surface reconstruction of Si(111) could be observed. The appearance of the (7×7) surface reconstruction by RHEED is often used as an indication of a clean Si(111) surface, although, as will be seen later, this does not prove that the surface is clean.

Since the nucleation layer is a crucial step in the growth of AlN on Si, a series of growths were performed with different nucleation layers. The nucleation layer consisted in the nitridation of the silicon surface by exposing the latter to either NH_3 or N-plasma for a

[1] At the beginning of this thesis, the substrate heater in the MBE was capable of a maximum substrate temperature of 950 °C. It was later replaced by a high temperature heater that can reach temperatures in excess of 1200 °C.

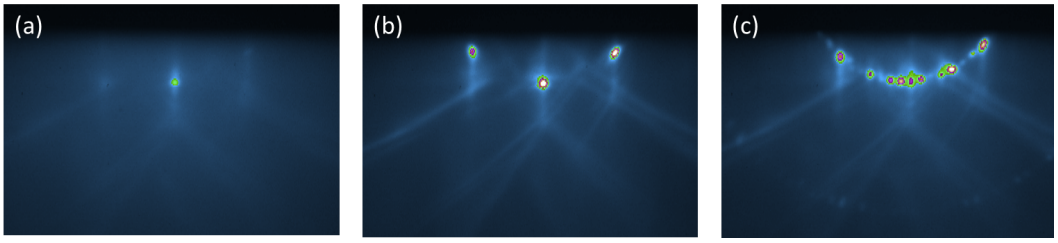

Figure 2.1 – RHEED patterns of the Si(111) substrates. (a) After degassing at 600 °C, (b) during the high temperature annealing at 900 °C and (c) after the oxide removal at a substrate temperature of 790 °C.

short duration of time. Then, with the N-species shuttered, 1.5 ML of Al were deposited at the same substrate temperature. Finally, a 100 nm thick AlN layer was grown by simultaneously supplying 20 sccm of NH_3 and aluminum (V_{AlN} = 350 nm/hr) and ramping up the substrate temperature to 900 °C. The quality of the resulting 100 nm thick AlN layer was used to monitor the effect of the substrate temperature and nitrogen species during the formation of the nucleation layer.

Two key parameters were explored: the temperature of the substrate (T_s) and the N-species. The nitridation step can be precisely controlled with the plasma source because molecular nitrogen will not contribute to the nitridation, and thus switching off the RF source immediately stops the supply of N-active species. In the case of ammonia, the opening and closing of the valves can be used to adjust the ammonia flux. However, once the valve is closed some ammonia still persists in the system and continues the nitridation until it is pumped out or trapped in the cryopanels. The cryopanels of the MBE are capable of storing large amounts of ammonia. In turn, this ammonia may outgas producing a parasitic nitridation, that is, SiN is formed in an uncontrolled manner without deliberately providing ammonia to the substrate.

The results of the sample series are summarized in terms of root mean squared surface roughness (r_{RMS}) and full width at half maximum (FWHM) of the x-ray diffraction (XRD) ω rocking curve along (002) in figure 2.2. As a general trend, the quality of the AlN is enhanced when using an NH_3 nitridation, both in the crystal quality and the r_{RMS}. Also, it can be observed that the best quality is obtained when performing the nucleation layer at a constant temperature of 800 °C. The reproducibility of the procedure was tested by growing two nominally identical samples with a nucleation layer formed at 600 °C, see figure 2.2 black square frames. The difference in quality is striking. Moreover, all the samples in the series exhibit r_{RMS} in excess of 2 nm and lack of crystal quality. A fundamental step in the growth procedure has been overlooked, the preparation of the Si(111) surface.

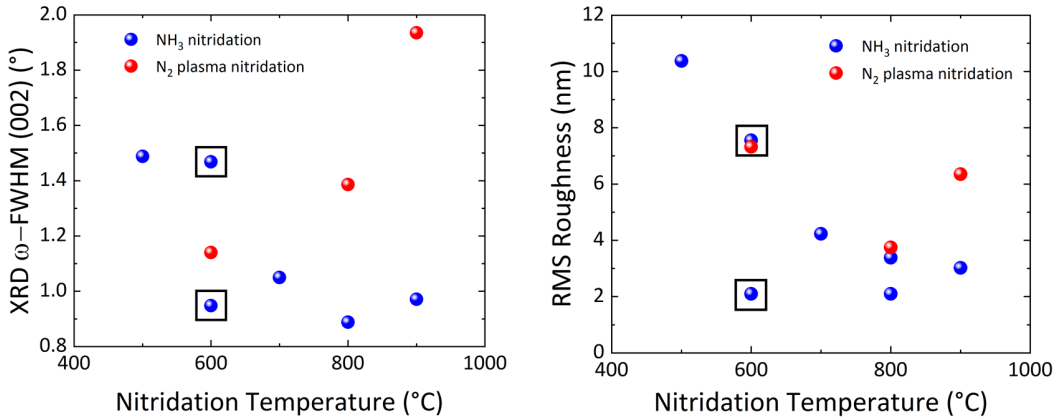

Figure 2.2 – (a) FWHM of the rocking curve ω scan of the AlN (002) crystallographic direction. (b) Root mean square (RMS) roughness of the AlN films, measured by AFM over 10×10 μm^2. The data points marked by black square frames highlight the lack of reproducibility.

2.4 Si(111) surface preparation

As a consequence of the widespread use of silicon substrates in the electronics industry, various silicon substrate cleaning procedures have been proposed to get chemically clean and atomically flat surfaces. Some of the most commonplace procedures are the RCA [87] and the Shiraki processes [88]. These techniques have the advantage of being performed at room temperature. The principle of the procedures consists in chemically etching the native oxide with acid solutions, then forming an oxide which captures most the impurities and contaminants, then the newly formed oxide is once again etched away. Alternatively, high temperature annealing in ultra high vacuum (UHV) can also lead to a clean and atomically flat Si surface. The sample temperature must be raised above 900 °C to expose the silicon surface. The sample is usually heated by means of direct current. In this way, temperatures in excess of 1000 °C can be achieved. The resulting surface consists of atomically flat terraces which are free of defects [89]. Oxide removal by high temperature annealing for the growth of AlN by MBE is a more practical approach over the RCA and Shiraki processes, as the delicate and cumbersome *ex situ* chemical process is no longer required, and the preparation of the Si substrate can be done immediately before the epitaxy.

The substrate heater of the MBE system was upgraded to a nitride resistant high temperature model, capable of temperature ramps of 200 °C/minute and a maximum substrate temperature above 1200 °C. A series of samples were prepared in the MBE growth chamber. The samples were annealed by means of radiative heating. The Si substrate is first outgassed in the preparation chamber during 4 h at 600 °C. Then we performed several high temperature cycles, with a maximum temperature of either 950 or 1100 °C for different durations (between 90 to 900 s). The experiments are summarized

Table 2.1 – Annealing parameters of the *in situ* thermally cleaned Si substrates.

Sample	A	B	C	D
Number of annealing cycles	1	6	4	4
Temperature (°C)	950	950	1100	1100
Duration (s)	900	120	90	120

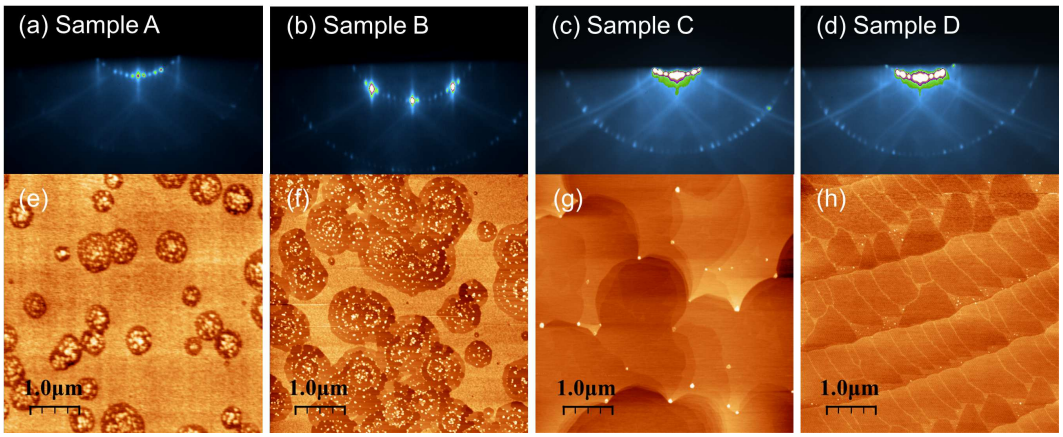

Figure 2.3 – RHEED pattern and corresponding 5×5 μm^2 AFM images of Si(111) substrates after thermal cleaning in the growth chamber as detailed in Table 2.1. Sample A presents a blurry 7×7 surface reconstruction (a). The AFM picture shows that the surface is still mainly covered by native oxide, the voids corresponding to oxide desorption (e). Sample B exhibits a better defined 7×7 RHEED pattern (b). The AFM image displays larger voids in comparison to sample A (f). In sample C, the native oxide has been completely removed. Although RHEED (c) shows a well defined 7×7 surface reconstruction (c), the corresponding AFM image indicates the presence of small hillocks that pin the steps (g). These tiny defects are identified as SiC crystallites. Sample D corresponds to an optimized thermal cleaning procedure. It yields atomic steps and large terraces of 2 μm with a substructure associated to the 7×7 and 1×1 surface reconstructions (h). Adapted from reference [70]

in table 2.1.

In figure 2.3, the results of the sample series described in table 2.1 are presented in terms of the Si(111) (7×7) surface reconstruction, as measured by the RHEED pattern, and the surface, as measured by AFM. For sample A, we observe that the RHEED pattern is blurry, vertical lines can be observed, indicating a disordered surface (figure 2.3 (a)). In fact, the RHEED pattern is comparable to the one obtained during the preliminary results (figure 2.1). Correspondingly, the AFM image displays a somewhat flat surface with sporadic voids, which are in turn decorated by islands (figure 2.3 (e)). The topmost surface is identified as the amorphous native oxide, hence the lack of defined atomic terraces. The actual Si surface is exposed in the voids. For sample B, six annealing cycles were used. The RHEED specular beam and (1×1) diffraction spots are much

more defined, however, the (7×7) pattern is faint 2.3(b). Analysis of the surface by AFM demonstrates that a large portion of the surface is still covered by the native oxide. The desorption of the native oxide follows the proposed model by Kobayashi *et al.* [90]. The oxide desorption starts at single points, forming voids in the native oxide, which then expand radially to the rest of the native oxide. Raising the annealing temperature to 1100 °C for sample C yields a very clear (7×7) surface reconstruction by RHEED. The AFM of sample C displays a very smooth oxide-free surface with some bunching of atomic steps. However, some small islands are visible. These have been identified as SiC nanocrystallites [91]. Finally, increasing the duration of the annealing cycles yields an extremely smooth surface as shown in figure 2.3(h). Large, about 2 μm wide, parallel terraces, delimited by 1 ML high ($\sim$ 0.3 nm) atomic steps are present. Within the terraces a substructure is visible. The large areas correspond to highly ordered (7×7) surface reconstruction and the triangular domains connected by lines to unreconstructed (1×1) domains [92]. Interestingly, the RHEED pattern of sample C and D are extremely similar; the small surface coverage by β-SiC nanocrystallites does not impact the RHEED pattern. Consequently the appearance of the (7×7) surface reconstruction by RHEED is not a sufficient proof of a highly ordered, clean and flat Si surface.

The procedure of sample D was confirmed to be highly reproducible over tens of samples. It was found that the recipe consistently yields high quality Si(111) surfaces with parallel atomic steps. All further samples described in this thesis involving Si substrates were prepared in this way.

The (7×7) surface reconstruction of Si(111)

The (7×7) surface reconstruction of Si(111), first observed in 1959 by Schlier *et al.* [93], is probably the most complex and widely studied surface. It took over 30 years to achieve a consensus on the geometry of the reconstruction. The accepted model, known as a dimer-adatom-stacking-fault (DAS), was proposed by Takayanagi *et al.* [94] This model consists of three atomic layers of restructured atoms as depicted in figure 2.4. The unit cell with a (7×7) reconstruction forms of an angle cavity and two triangular subcells separated by dimer chains.

As previously noted, the reconstruction appears when cooling down a clean Si(111) surface below 830 °C. It abruptly disappears if the temperature is raised above 830 °C. In fact, the surface reconstruction is a convenient way to calibrate the emissivity of the sample for the pyrometyric measurement of the substrate temperature.

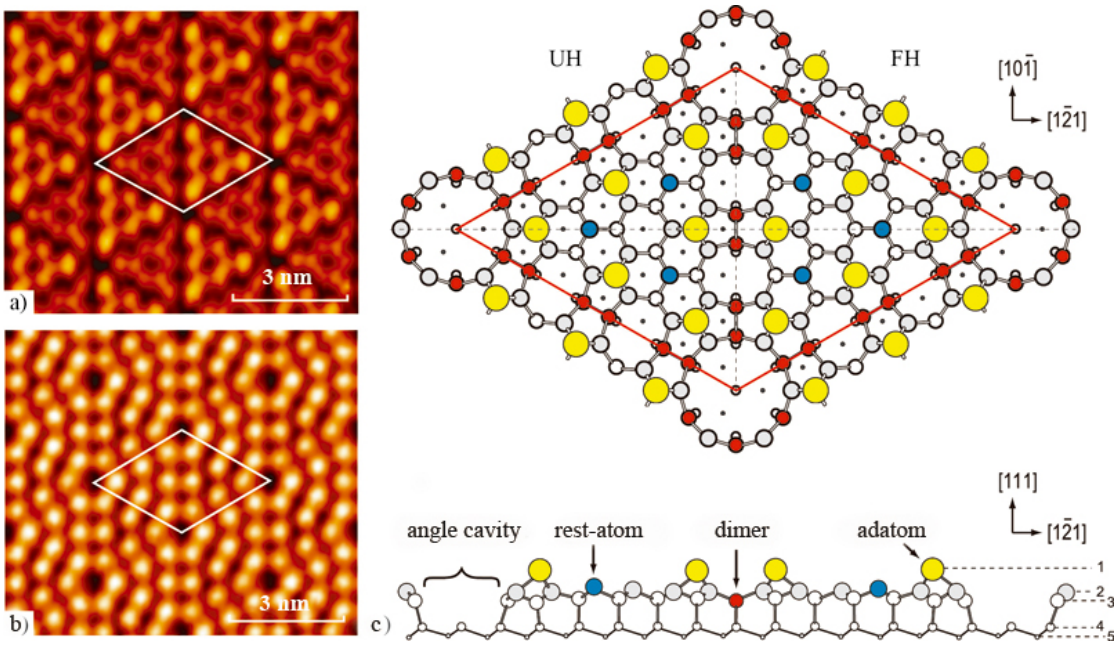

Figure 2.4 – (a) STM image of the filled and (b) unfilled states of the (7×7) surface reconstruction of Si(111). (c) Top and cross section schematic of the dimer-adatom-stacking fault geometry. Adapted from reference [95] under a Creative Commons license.

2.5 AlN growth at high temperature

The substrate temperature during MBE growth is often limited by the decomposition of the growing material. In the case of GaN, the surface starts to sublimate in vacuum at a non-negligable rate at a temperature of 750 °C, a process which can be prevented by supplying ammonia [96]. Similarly, the growth of InN is limited to about 480 °C [97]. Nevertheless, an enhanced crystalline quality [98] and surface morphology [99] is obtained when growing at high temperatures ($\geq$ 800 °C).

The MBE environment is excellent for studying crystal growth, thanks to the possibility of real time *in situ* monitoring techniques, such as laser reflectivity, RHEED, and mass spectroscopy. For instance, the evaporation rate of the sample surface can be measured by laser reflectivity [96]. The growth rate is available from the interference pattern within the Fabry-Pérot cavity formed by the interfaces between vacuum, sample surface and substrate. The intensity of the reflected laser beam depends on the sample thickness by the phase relationship (δ) between the reflection from each of the interfaces:

$$\delta = \frac{2\pi}{\lambda} 2nl \cos\theta, \tag{2.1}$$

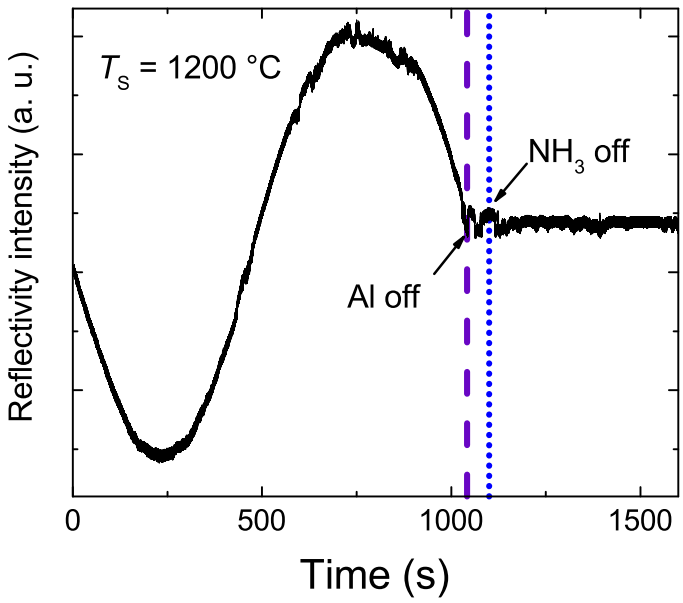

Figure 2.5 – *In situ* laser reflectivity during the growth of AlN including a growth interruption at half the intensity oscillation amplitude. We observe a constant intensity after closing the NH_3 flow indicating negligible evaporation. Adapted from reference [70]

where λ is the wavelength of the laser, n is the refractive index of the layer, l the thickness of the sample, and θ the incidence angle. Hence there is a direct relation between the intensity of the reflected signal and the thickness of the sample since all the other variables remain constant.

Laser reflectivity was used to monitor the decomposition rate of AlN as a function of temperature. The growth of AlN was stopped at half an oscillation amplitude. At this instance, the technique is very sensitive to small changes in thickness, any growth or evaporation of material will be accompanied by a non-zero slope. It was found that even at a substrate temperature of 1200 °C the reflectivity signal stays constant when the ammonia flux is closed. Therefore, AlN does not evaporate under ultra high vacuum at temperatures as high as 1200 °C. This is quite different from GaN.

In general, it is desirable for the crystal growth to proceed in a step-flow regime as this allows for extremely low surface roughnesses. The growth mode will undergo a transition from layer-by-layer to step-flow if all the impinging adatoms have sufficient diffusion length to reach the edge of a step and incorporate. Therefore, the transition will depend on the average terrace width (or miscut angle) and the diffusion length, which is fixed by the substrate temperature and the growth rate. RHEED intensity oscillations are observed due to a roughening of the surface by the nucleation of single ML high islands, whereas, if the growth mode follows a step-flow regime, the surface never roughens as all

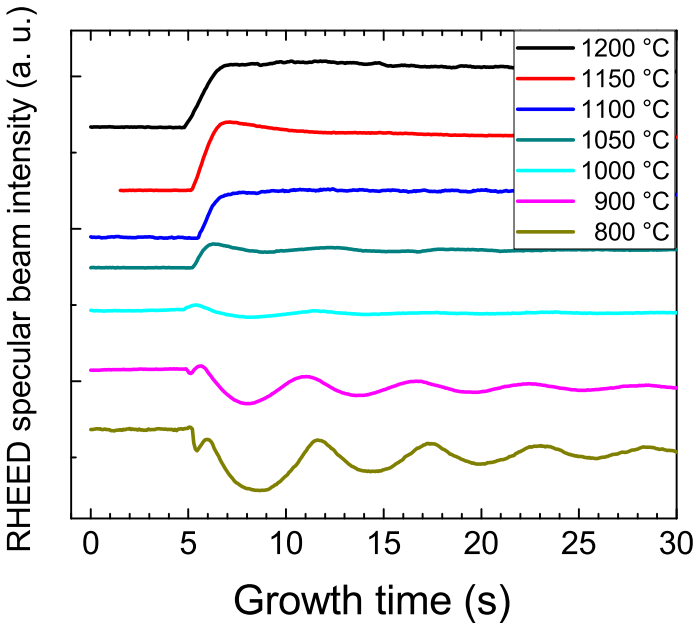

Figure 2.6 – RHEED intensity oscillations for different substrate temperatures during AlN growth. Well defined oscillations are observed at 800 °C. As the temperature increases the oscillations start dampening and at 1100 °C they have completely disappeared. Adapted from reference [70]

the incorporation of new atoms happens at the edge of the existing atomic steps. In this case, RHEED intensity oscillations are no longer observed [51].

A series of experiments were carried out on MOVPE grown AlN on sapphire templates with a dislocation density of around 10^9 cm^{-2} and a surface misorientation below 0.5° off. RHEED intensity oscillations during the growth of AlN were monitored as a function of the substrate temperature while keeping a constant Al and NH_3 flux. The results are depicted in figure 2.6. Clear oscillations are measured at 800 °C, while the period increases with increasing temperature and eventually they vanish above 1050 °C. The growth mode transitions from a 2D, layer-by-layer, growth mode into a 1D step-flow regime at a temperature of 1100 °C. Additionally, the frequency of the oscillations decreases with increasing temperature. As the growth mode turns to step-flow regime, an ever larger portion of the adatoms incorporate at the step edges, and thus do not contribute to RHEED intensity oscillations, which are a direct consequence of 2D nucleation [51].

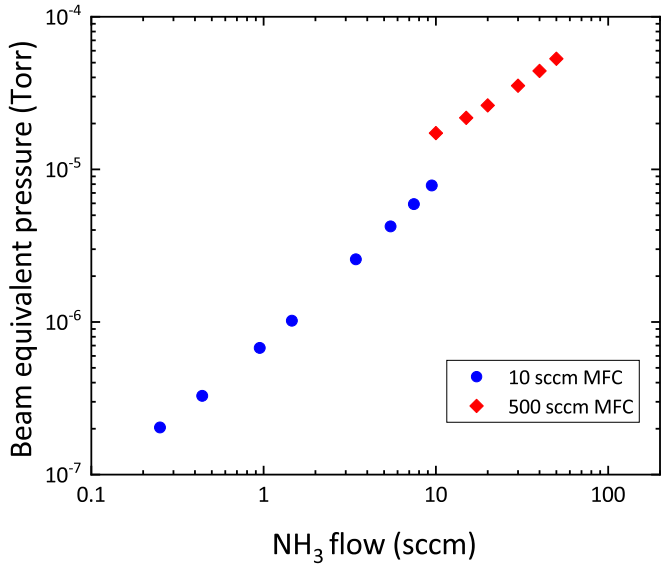

Figure 2.7 – Beam equivalent pressure as a function of the NH_3 flow for the two mass flow controllers (MFC).

2.5.1 Determination of stoichiometric growth conditions as a function of the substrate temperature

During NH_3-MBE, the impinging flux of NH_3 is only partially used for the actual growth due to the low efficiency, whereas the sticking coefficient of Ga and Al is 1 for typical growth temperatures ($\leq$ 850 °C for GaN and $\leq$ 1200 °C for AlN). By determining the stoichiometric point it is possible to assess the effective V/III ratio. The stoichiometric point can be measured by monitoring the growth rate of AlN as a function of the NH_3 flow. Under Al-rich conditions, the growth rate will be limited by the availability of N species and will lead to the formation of droplets and to a lower AlN growth rate. As the NH_3 is increased, the growth rate also increases until reaching a maximum at the stoichiometric point [100, 101]. By analogy, the stoichiometric point can also be found by varying the Al cell temperature and keeping a fixed NH_3 flow.

The stoichiometric point for the growth of AlN corresponds to very small NH_3 flows even for high Al growth rates. A secondary mass flow controller was installed to allow for NH_3 flows between 0.25 and 10 sccm, whereas the primary mass flow controller operates between 10 and 500 sccm. The BEP of NH_3 was measured as a function of NH_3 flow and the results are plotted in figure 2.7. An offset between the two mass flow controllers occurs at 10 sccm, therefore, further results of this section and the next chapter will be reported in terms of NH_3 BEP.

The growth rate of AlN was measured as a function of NH_3 BEP on AlN on sapphire templates. For growth conditions corresponding to the N-rich regime, clear RHEED intensity oscillations were observed and the growth rate was estimated with a precision

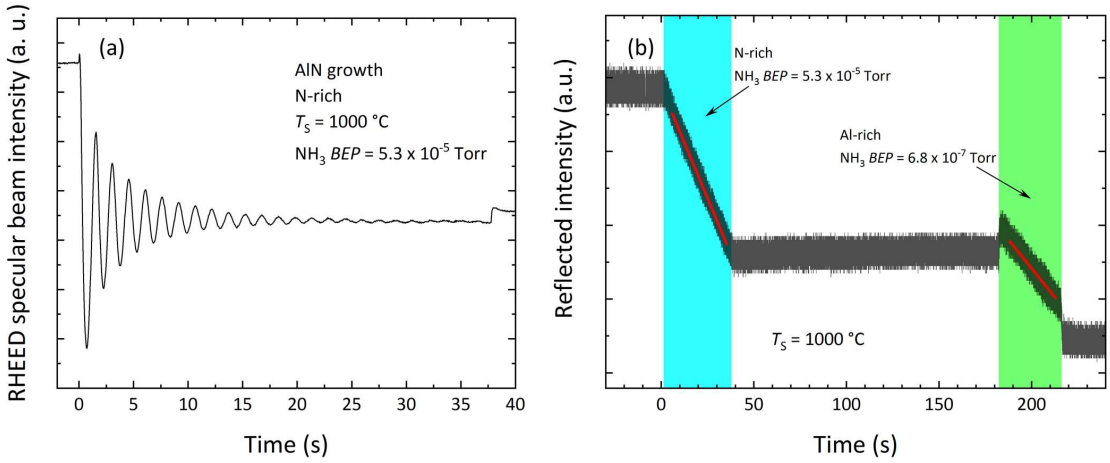

Figure 2.8 – (a) RHEED specular beam intensity oscillations during homoepitaxial growth of AlN under N-rich conditions used to measure the growth rate and determine the stochiometric point. (b) Laser reflectivity for the measurement of the growth rate under Al-rich conditions. The slope is calibrated under N-rich conditions together with RHEED oscillations.

better than 0.01 ML/s, see figure 2.8 (a). For the Al-rich regime, RHEED oscillations were not observable, instead the growth rate was measured by laser reflectivity. The thickness of the film was set so that the reflected intensity was in the middle of the oscillation amplitude, where the growth rate is proportional to the slope of the reflectivity as a function of time. As illustrated in figure 2.8(b), the slope was calibrated under N-rich conditions to obtain a relation between the growth rate and the slope. Finally, the growth rate under Al-rich conditions was measured by comparing the slopes.

In figure 2.9, we plot the AlN growth rate as a function of NH_3 BEP. Under Al-rich conditions, the growth rate is limited by the availability of N species, Al accumulates on the surface but is not incorporated as AlN. Under N-rich conditions, the growth rate is determined by the flux of Al. We can also observe a small decrease in the growth rate for high NH_3 BEPs, as the NH_3 pressure is increased the mean free path of the Al species reduces [102].

The experiments were reproduced for two more substrate temperatures; 800 and 900 °C, while keeping the same Al cell temperature. The NH_3-BEP needed to achieve stoichiometric growth conditions is plotted in figure 2.10 as a function of temperature. The ammonia flux is almost twice at 800 °C compared to 1000 °C. Therefore, the effective V/III ratio increases with increasing growth temperature even when the NH_3 flow is fixed.

Notice that the determination of the stoichiometric point and hence the actual V/III ratio was performed posterior to the optimization of the AlN growth presented in this chapter. Further on, the article on which this chapter is based is discussed in terms of

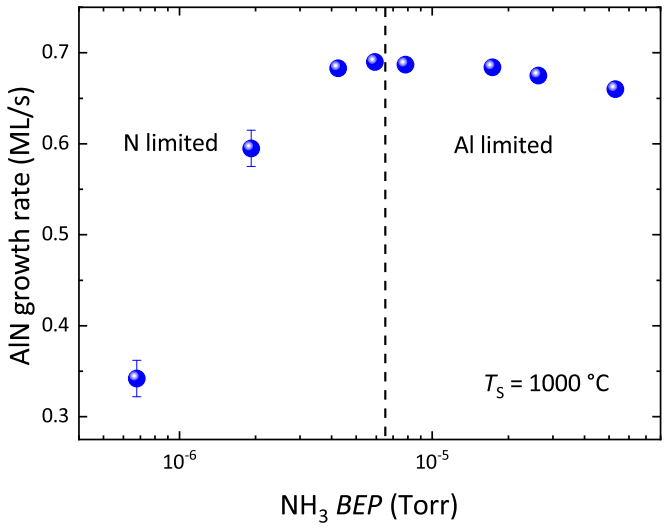

Figure 2.9 – AlN growth rate as a function of NH_3-BEP, under low(high) NH_3 flows the growth proceeds in an Al(N)-rich regime and the growth rate is limited by the availability of N(Al) species. The stoichiometric point is marked as a dashed line. A decline in the growth rate can be observed with increasing NH_3 flow due to gas scattering.

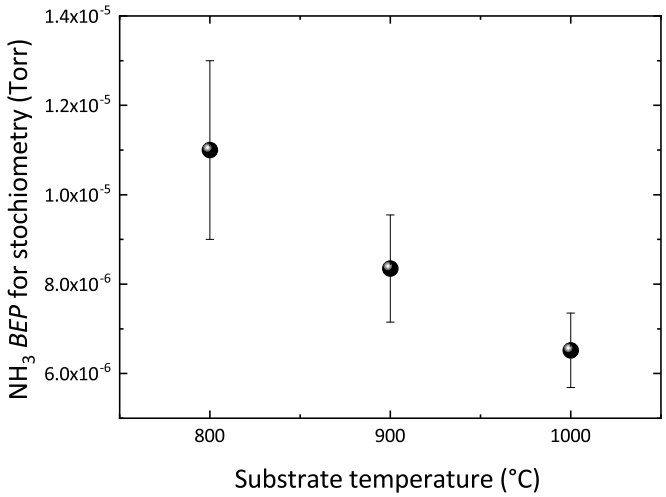

Figure 2.10 – NH_3-BEP necessary for stoichiometric growth, for an AlN growth rate of 0.7 ML/s, as a function of the substrate temperature. Lower NH_3 flows are necessary with increasing substrate temperature due to the enhanced thermal cracking of NH_3.

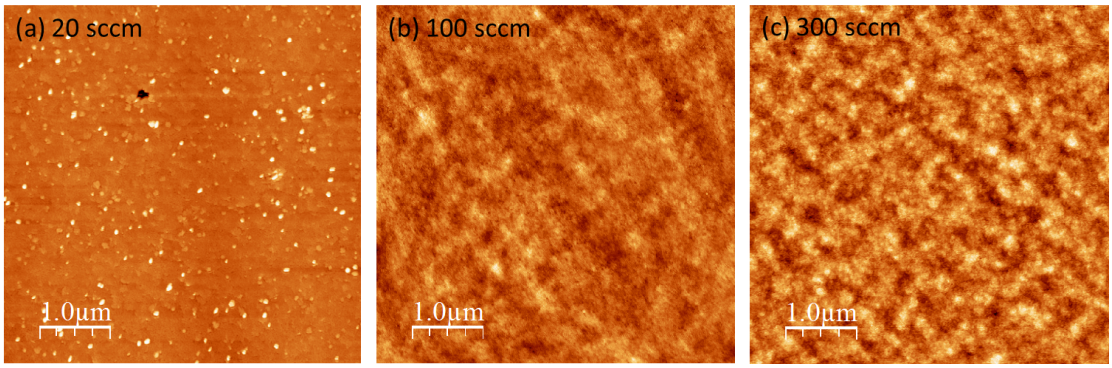

Figure 2.11 – 5×5 μm^2 AFM images of 100 nm of AlN on Si(111) grown with an NH_3 flow of (a) 20, (b) 100 and (c) 300 sccm. The z ranges are 40 nm for (a) and 3.5 nm for (b) and (c). The growths of AlN under low NH_3 fluxes exhibited hillocks and an overall lower quality.

NH_3 fluxes. For these reasons, the results of this chapter will be given in NH_3 fluxes.

2.6 Optimization of the AlN growth conditions

As previously seen in the preceeding sections, the preparation of the Si substrate as well as that of the nucleation layer are critical for the reproducibility and quality during the growth of AlN on Si(111). We have also demonstrated that AlN does not decompose in UHV at temperatures as high as 1200 °C. Finally, it has been shown that the growth mode of AlN by NH_3-MBE undergoes a transition from a layer-by-layer regime into step-flow mode for a substrate temperature of 1100 °C. Now we turn our attention towards the impact of the growth temperature and ammonia flow on the growth of AlN.

In 2006, A. LeLouarn reported in his thesis on the nucleation of AlN on Si(111) [92]. He explored in depth the different surface reconstructions at each stage of the nucleation of AlN on Si(111) for a variety of nucleation strategies [92]. The recipe we used in the present work is the following: starting from a high quality Si(111) surface, the nucleation layer was prepared by setting the T_S to 800 °C and exposing the surface to 10 sccm of NH_3 during 5 s. Then while keeping the same T_S and UHV the surface was exposed to the equivalent Al thickness of 1.5 ML. Next the AlN growth was initiated by simultaneously opening the Al cell and opening the NH_3 valves and setting the NH_3 flow to 20 sccm. Finally, T_S and the NH_3 flow were ramped up to their setting points.

Keeping the growth temperature at 1100 °C, we investigated the impact of the NH_3 flow on the properties of 100 nm thick films of AlN on Si(111). The surface was studied by AFM and the structural quality measured by XRD. In figure 2.11, we display the AFM images of three typical samples, grown with 20 sccm, 100 sccm and 300 sccm. The samples with low NH_3 flow revealed a 3D RHEED pattern and a high density of

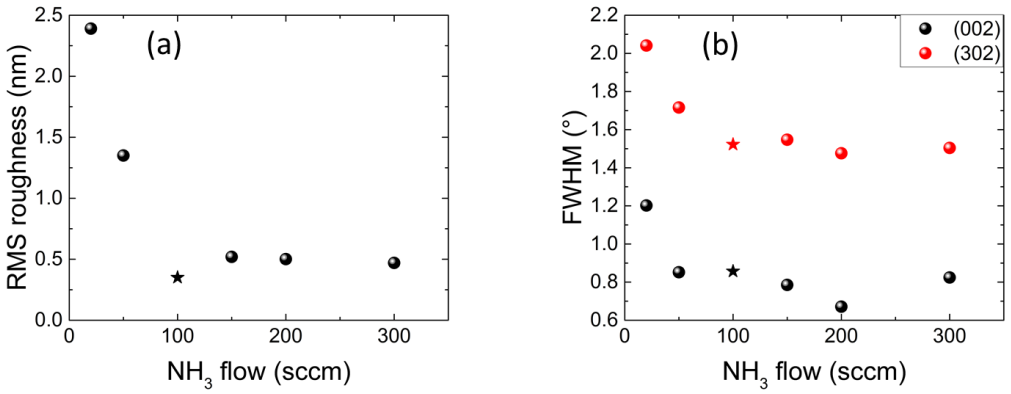

Figure 2.12 – (a) r_{RMS} as measured by AFM on 5×5 μm^2 areas of 100 nm thick AlN films grown with different NH_3 flows. (b) Dependence of the FWHM of the (002) and (302) XRD ω rocking curves on the NH_3 flow. All films are grown at 1100 °C and are 100 nm thick except the one denoted by ★ which is 75 nm thick. Adapted from reference [70].

hillocks at the surface, which accounts for the significant r_{RMS} of 2.4 nm. On the other hand, the samples grown at higher NH_3 flows, i.e. above 100 sccm, exhibit very flat surfaces and no hills or pits. In fact, a very clear trend can be observed when plotting r_{RMS} as a function of the NH_3 flow. Very low roughnesses can be achieved under high NH_3 flows, while a clear degradation of the surface is obtained when lowering the NH_3 flux. Furthermore, XRD ω rocking curve measurements were performed around the (002) and (302) crystal orientations. The broadening of the XRD reflection around the (302) orientation provides a more complete indication of the crystal quality, as it is sensitive to edge, screw and mixed dislocations [103]. In figure 2.12(b) we plot the FWHM of both reflections. The value of both remains almost constant for flows in excess of 100 sccm. The density of dislocations is determined by the AlN/Si interface and the low mobility of Al adatoms hinders the formation of large 3D islands, limiting thereby dislocation bending and possible dislocation annihilation. However, for small NH_3 flows the crystal quality deteriorates in parallel with a roughening of the surface.

The surface of the layers grown with low NH_3 flows ($\leq$ 50 sccm) displays hillocks, which could be ascribed to Al droplets due to the lack of NH_3. The samples were then etched in HCl, but the surface morphology remained unchanged, indicating that the mounds observed by AFM for the two samples grown with a low V/III ratio (20 and 50 sccm) are not metallic droplets. We further performed KOH etching and found that the surface exhibited large etch pits, from tens to several hundreds of nanometers in diameter. In figure 2.13, the AFM of a sample grown with 20 sccm at 900 °C is displayed before (Fig. 2.13(a)) and after KOH etching (Fig. 2.13(b)). These etch pits could be related to inversion domains since N-polar AlN is readily etched by KOH while Al-polar AlN remains unaffected [104].

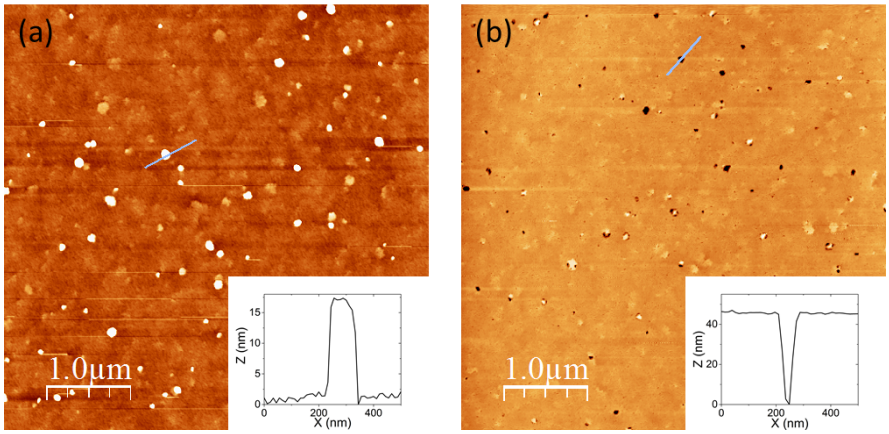

Figure 2.13 – (a) 5×5 μm^2 AFM of 100 nm of AlN on Si(111) grown with an NH_3 flow of 20 sccm and at a substrate temperature of 900 °C. The sample is plagued with hills with a diameter between 50 and 100 nm and several tens of nm in height. (b) AFM image of the same sample after KOH etching. All the hills have been etched away. Pits are now present in the surface, moreover, the pit diameter and density are similar to that of the hills before KOH etching. Inset: Line profile over a typical hill/void.

Impact of the growth temperature on the properties of AlN on Si(111)

The substrate temperature is often the most important parameter during MBE growth. Further optimization, and understanding of the growth of AlN on Si(111) by NH_3 was achieved by measuring the resulting surface morphology and structural properties, as a function of the growth temperature. The samples were grown with a substrate temperature between 900 and 1200 °C and a NH_3 flow of 100 sccm. As seen in the previous section, under this ammonia flow and a growth temperature of 1100 °C, the surface energy is high enough to prevent the formation of hills and/or inversion domains.

In figure 2.14, we plot the ω rocking curve FWHM for the (002) and (302) reflections. The (302) linewidth is almost unaffected by the temperature at which the growth is performed, with the exception of the highest temperature. The RHEED pattern displays streaks throughout the growth of the 100 nm thick layer. Such a 2D morphology does not allow the mechanisms for dislocation annihilation found during the early, three-dimensional, stage of the growth of GaN on sapphire [105, 106]. Instead, the total dislocation density is fixed during the early stages of the growth, which is common for all the samples. Further on, there is a slight improvement at the highest temperature. One may suppose that at high temperature dislocations can move, interact and eventually annihilate. For the (002) reflection, a trend of decreasing linewidth is observed with increasing substrate temperature, with the exception of 900 °C. However, the (002) reflection is only sensitive to screw and mixed dislocations, conversily the (302) is sensitive to edge, screw and mixed. Hence, the total dislocation density remains somewhat constant throughout the sample series, and only the ratio of edge to screw and mixed dislocations is changed for

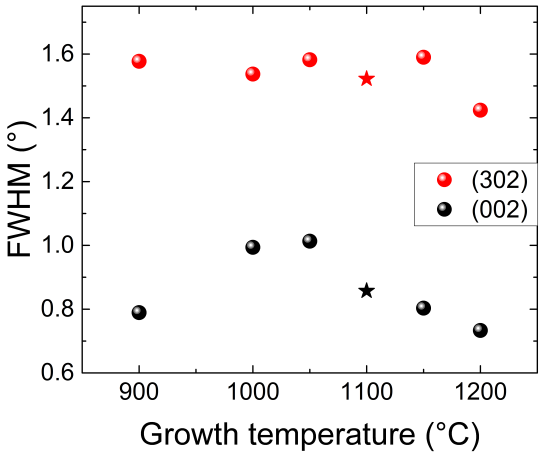

Figure 2.14 – FWHM of the ω rocking curve of AlN on Si(111) as a function of the growth temperature. All films are grown at 1100 °C and are 100 nm thick except the one denoted by ★ which is 75 nm thick.

the different samples. In conclusion, the total dislocation density is hardly affected by the growth temperature, and hence is rather fixed at the AlN/Si interface. However, the XRD linewidth is highly dependent on the film's total thickness, a FWHM of the (002) and (302) reflections as low as 0.36° and 0.78° were achieved by increasing the total thickness to 400 nm while employing a NH_3 flow of 200 sccm and setting T_S to 1100 °C. A similar trend was reported by Semond [68], where the (002) FWHM decreased from 1.3° to 0.7° and 0.36° for thickness of 40, 100 and 350 nm, respectively.

Further insight into the impact of the growth temperature was obtained by probing the strain state of the AlN epilayer. Due to the difference in TECs between Si and AlN, we expect the AlN films to be under tensile strain. Confocal micro-Raman spectroscopy was performed with a 405 nm laser. The frequency shift ($\Delta\omega$) for each phonon mode in the case of biaxial strain will be given by [107]:

$$\Delta\omega = 2a\epsilon_{xx} + b\epsilon_{zz} = 2\tilde{a}\sigma_{xx} + \tilde{b}\sigma_{zz}, \tag{2.2}$$

where the phonon deformation potentials a and b relate the change in $\Delta\omega$ to the strain ϵ or the phonon pressure coefficients $\tilde{a}$ and $\tilde{b}$ to the stress σ. Here, we have used the values reported by Callsen *et al.* [107] to extract the strain from the shift in the E_2^H phonon line. In figure 2.15, we plot the Raman shift of the E_2^H phonon line as a function of growth temperature, and the corresponding tensile strain. As expected, all data points are red shifted from the unstrained value (653.8 cm^{-1}), here plotted as a dashed line. We assumed a fully relaxed AlN layer during growth and calculated the strain due solely

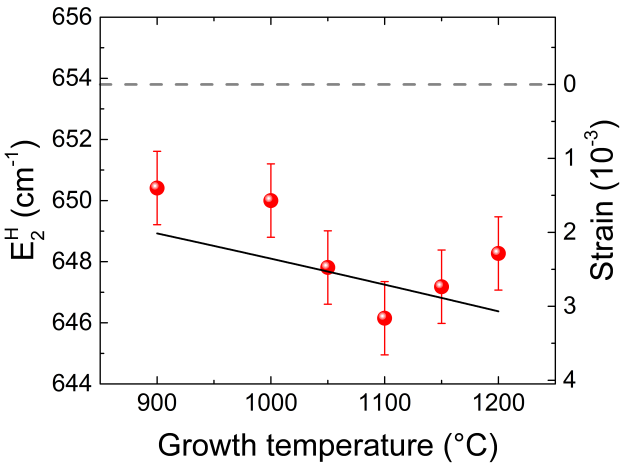

Figure 2.15 – Raman shift of the E_2^H phonon line and corresponding strain of the AlN on Si films as a function of growth temperature. The unstrained value is plotted as a dashed line and the expected strain due to the difference in TEC as a solid black line.

to the difference in TEC. The calculated strain is plotted in figure 2.15 (solid black line). The calculation used temperature dependent TEC from references [108] and [109]. The data roughly follows the theoretical prediction, with the strain increasing with growth temperature. However, an additional source of strain is necessary to explain the sample grown at 1100 °C. Heteroepitaxial films have been demonstrated to have an additional tensile strain due to grain coalescence [110]. However, the samples grown at low and high temperatures display a lower strain; structural defects and surface roughening are a source of strain relaxation. Actually, the surface roughness (see Fig. 2.16) clearly follows the same trend as the deviation from the calculated thermal strain. A minimum surface roughness is observed at 1100 °C, where the strain is maximum. Interestingly a sharp increase in surface roughness towards higher temperatures is accompanied by a decrease in tensile strain. Therefore, layers with a high grain coalescence and reduced roughness exhibit strain beyond that of the thermally induced one. This has the drawback of a tendency for crack formation in high quality III-nitride layers grown on silicon.

Detailed analysis of the surface morphology by AFM reveals clear differences depending on the growth temperature. The layer grown at the lowest temperature (900 °C) exhibits hills of around 10 nm in height and between 50 and 100 nm in diameter with a density of 1.2 x 10^8 cm^{-2} (Fig. 2.17(a)). The sample was etched in KOH and the hills disappeared in favor of voids with similar diameters and density. Therefore, these could be related to inversion domains. Structural defects such as inversion domains are thus providing strain relaxation, but do not contribute significantly to the broadening of the XRD linewidths. These hills are no longer visible for the growth performed at 1000 °C and above. In fact, the roughness of the sample decreases with increasing substrate temperature, as the growth turns into the step-flow regime (see Fig. 2.6). In contrast, the sample roughens

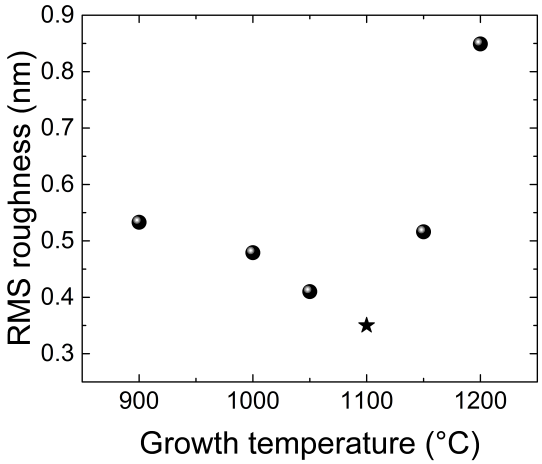

Figure 2.16 – r_{RMS} from 5×5 μm^2 AFMs of AlN on Si films as a function of growth temperature. r_{RMS} follows a similar trend to the strain state. All films are grown with 100 sccm of NH_3 and are 100 nm thick except the one denoted by ★ which is 75 nm thick.

when grown at 1200 °C, due to spiral growth around screw dislocations (Fig. 2.17(c)).

At the optimum growth temperature of 1100 °C the surface is extremely smooth, further AFM measurements over a 30×30 μm^2, see figure 2.17(d), revealed an extremely flat and featureless surface. A r_{RMS} as low as 0.33 nm was obtained even over such a large area. A line profile from the large scale AFM exhibits height variations of around 1 nm over a a distance of 30 μm. Such a smooth surface is ideal for the nucleation and study of QDs, which are typically 2-4 nm in height and will be therefore easily measurable by AFM. The quality of the optimized layers is further showcased by SEM. In figure 2.18, SEM images of an unoptimized, 100 nm thick AlN on Si layer grown during the early stages of this thesis and an optimized sample are presented. The unoptimized layer (Fig. 2.18(a)) displays pits and defects throughout the surface, whereas the optimized sample (Fig. 2.18 (b)) has no visible features.

Let us recall the presence of hills, attributed to inversion domains, that appeared for the sample grown at low temperature (900 °C). The cracking efficiency of NH_3 into active N species that contribute to the growth was proven to be highly temperature dependent in the case of GaN growth by NH_3-MBE [101]. As was shown in section 2.5.1, the effective V/III ratio depends on the substrate temperature as the cracking efficiency of NH_3 increases with increasing substrate temperature. Therefore, similarly to the case where the NH_3 flux was decreased and hillocks appeared on the surface, the decrease in substrate temperature led to a decrease in the effective V/III ratio and therefore to the appearance of hillocks.

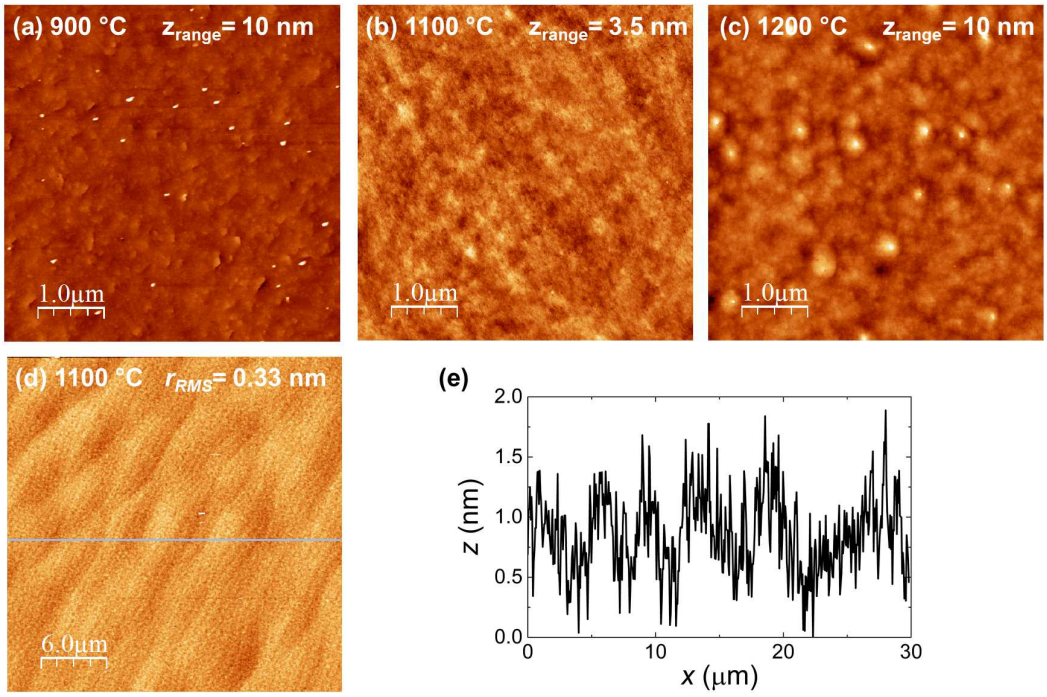

Figure 2.17 – 5×5 μm^2 AFM images ((a), (b) and (c)) of AlN on Si(111) grown at 900, 1100 and 1200 °C respectively. (d) 30×30 μm^2 AFM image of the sample grown at 1100 °C and corresponding line profile (e). Adapted from reference [70]

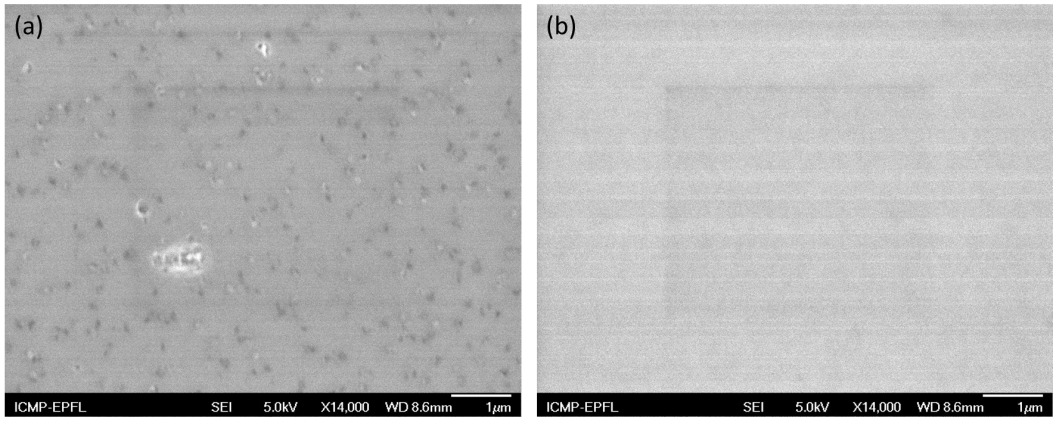

Figure 2.18 – Plan view SEM images of the surface of an unoptimized AlN on Si sample grown at the beginning of this thesis (a) and an optimized sample grown at high temperature (b).

3 Stranski Krastanov Growth of GaN Quantum Dots

In 1932, the red or yellow color found in some glasses was produced by the presence of microscopic crystals of CdSe and CdS. In 1985, the emission energy of these glasses was attributed to the quantum confinament of excitons in 0D systems [111]. During the early 1980s, the dimensionality of the active region in optoelectronic devices was linked to its current threshold, thus theoritizing that zero-dimensional systems would make an ideal gain medium for low threshold lasers [37]. Ever since, research focused on semiconductor QDs has been abundant for their applications in optoelectronic devices [112], optical quantum communciation protocols [113, 114], cavity quantum electrodynamics, and quantum metrology [115].

Three fabrication techniques for QDs have been the most prolific: synthesis of colloidal QDs in a chemical solution [116], droplet epitaxy [117] and SK growth [118]. Colloidal QDs have been succesfully made out of different materials such as: CdSe, CdTe for the visible range and PbS and Ag_2S for near-infrared. On the other hand, they are useful as fluorophores for biomedical imaging [119] and as color convertors for color displays [120]. One of the main drawbacks of such colloidal QDs is their toxicity and their implementation in a convenient and scalable solid-state host system. In contrast, both droplet epitaxy and SK have the advantage of being inherently solid-state based. In addition, the emission energy and density of such QDs can be finely tuned. Extensive research in the growth of conventional III-V semiconductors has led to QD based lasers [121] and integrated photonic circuits utilizing QDs as tunable single photon sources [122].

Two distinct epitaxial growth modes can produce QDs from 3D islanding. The VW growth mode entails only the formation of islands while the SK growth incorporates a flat layer plus islands. The transition from a 2D surface to 3D islands is strain driven from the lattice mismatch of the substrate and the epitaxial layer. As the thickness of the growing layer increases, the strain energy builds up. Eventually, the strain is released either by the creation of dislocations or 3D islanding. In the prototypical InAs/GaAs system, the

transition into self-assembled islands occurs spontaneously during growth after a certain amount of InAs has been deposited (1.7 MLs). The minimum amount of InAs required for the transition is called the critical thickness for the 2D-3D transition (h_{2D-3D}). The driving force behind the spontaneous transition is the large lattice mismatch between InAs and GaAs, which amounts to 7.2%. The transition depends not only on the lattice mismatch, but also on the interface and surface energies. If the energetic cost to create islands ($\Delta\gamma$) exceeds that of dislocation creation, the layer will relax plastically and remain 2D.

The lattice mismatch between GaN and AlN only amounts to 2.5%, making the transition into a SK growth mode highly dependent on $\Delta\gamma$. Therefore, the transition is not ubiquitous and both FM and SK growth modes can be achieved using the same growth technique [53, 31]. Whether the growth proceeds in a FM or SK growth mode will governed by thermodynamics. The variables will be the thickness of the film (h), the lattice mismatch, the film's biaxial modulus and the surface energy [123]. Of these, the most important one is perhaps the surface energy which can be controlled by the surface chemistry. For instance, a 2D or 3D morphology can be achieved by changing the V/III ratio during growth of GaN on AlN [124] or by desorption of excess Te when growing CdTe on ZnTe [125]. The transition on the growth mode depends only on the energetic balance and not on the kinetics as the transition was shown to be insensitive to the growth rate in the InAs/GaAs system [126]. Further evidence of the thermodynamical regime is presented in the reversibility of the transition depending on the surface energy [1].

The highlights and main results presented in this chapter can be found in the paper published in Applied Physics Letters [31].

3.1 State of the Art

3.1.1 SK GaN QDs by PA-MBE

GaN QD have been realized using plasma assisted MBE (PA-MBE) [25, 27, 30, 127], NH_3-MBE [1, 32, 128, 129, 130] and MOVPE [28, 131, 132]. Let us address first the growth by PA-MBE. In this technique two growth regimes have been identified: Ga-rich and N-rich. In the case of a Ga-rich growth regime, an auto-surfactant effect is observed, where a two ML thick Ga film prevents islanding [25, 133]. Under this regime, smooth surfaces are obtained as the growth proceeds in step flow. Close to stochiometric growth conditions the growth proceeds in a 2D layer by layer nucleation. It is under N-rich conditions that $\Delta\gamma$ is low enough for the formation of 3D islands [25, 133]. Even then, the growth has to be combined with proper kinetics to obtain self-organized GaN QDs. Interestingly, using this growth technique, h_{2D-3D} has a value of 2.5 ML in contrast to 3 ML for NH_3-MBE. In fact, the calculated value for the critical thickness based on energy

minimization within the framework of Frank and Van der Merwe yields 3 ML [53].

3.1.2 Modified SK growth by NH_3-MBE

The growth of GaN by NH_3-MBE is typically done under N-rich conditions, in fact the best optical and structural quality is achieved when growing at a substrate temperature of 830 °C and a very high NH_3 flow, reported as 50 sccm[1] and a chamber pressure of 10^{-6} Torr [134]. Further on, at such high temperatures GaN decomposes under vacuum, a process which can be prevented by supplying NH_3 [96]. Using such growth conditions, the growth of GaN on AlN proceeds in the FM regime leading to plastic relaxation [1]. In fact, this behavior is found throughout the temperature range from 750 to 900 °C, and is independent of the initial density of dislocations [53].

A procedure, which will be referred to as the m-SK growth, was developed in 1999 to achieve GaN QDs on AlN by NH_3-MBE [1]. It consists of depositing a few MLs of GaN under typical growth conditions, where the layer is still 2D. Then the growth is interrupted by shuttering both the Ga and NH_3 fluxes, then the layer transitions to 3D islands. The minimum thickness of the 2D-GaN film to achieve the 2D-3D transition using m-SK is 3 MLs. As expected due to the reduction of the lattice-mismatch, h_{2D-3D} increases if the procedure is performed on $Al_xGa_{1-x}N$ instead, with 4.5 MLs for $Al_{0.25}Ga_{0.75}N$ and 6 MLs for $Al_{0.5}Ga_{0.5}N$ [40]. The height of the QDs can be easily manipulated by changing the thickness of the 2D GaN layer. In turn, the emission energy will depend on the height of the QDs. In fact, the emission energy can be tuned from 4.5 eV down to 2 eV. This emission energy much below that of bulk GaN is due to the huge internal electric field and related QCSE [1].

3.2 Stranski Krastanov growth of GaN on AlN

3.2.1 Growth conditions for SK islands

A comparable control over the properties of GaN QD, similar to the seminal InAs/GaAs QD system, should be feasible if the growth proceeds in an SK growth mode; the 2D-3D transition should occur spontaneously once the critical thickness has been reached. Therefore, we aimed at obtaining a phase transition from a 2D surface to 3D islands without requiring a growth interruption without NH_3 flow.

The energetics governing the film's morphology provide a roadmap towards achieving a true SK growth by NH_3-MBE. The film's free energy can be expressed according to

[1] NH_3 flows cannot be compared directly as the effective number of NH_3 molecules reaching the surface will depend on the reactor geometry

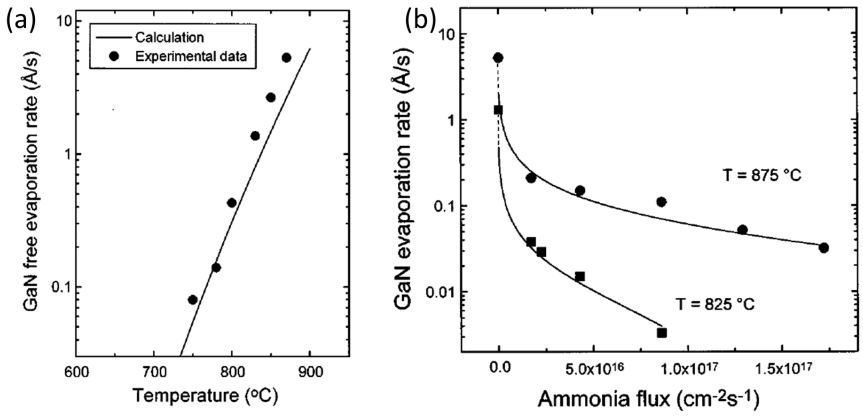

Figure 3.1 – (a) Evaporation rate of GaN under vacuum (b) GaN evaporation rate at a temperature of 875 °C and 825 °C as a function of the incident NH_3 flux. Adapted from reference [96].

Mariette [135] as:

$$E_{2D}(h) = M\epsilon^2_{\mathrm{GaN}}h + \gamma \tag{3.1}$$

and

$$E_{3D}(h) = (1-\alpha)M\epsilon^2_{\mathrm{GaN}}h + \gamma + \Delta\gamma, \tag{3.2}$$

where $E_{2D}(h)$ is the energy of the pseudomorphic 2D surface, M is the film's biaxial modulus, ϵ_{GaN} is the strain, $M\epsilon^2_{GaN}h$ is the elastic energy for a given GaN equivalent thickness (h) and γ is the surface energy for the (0001) surface. $E_{3D}(h)$ is the energy of the layer when a fraction α of the surface is covered by 3D islands and $\Delta\gamma$ is the surface energy cost to form the 3D islands.

By energy minimization, the film will transition into 3D islands if $E_{3D} < E_{2D}$. The strain energy will depend on h, as $M\epsilon^2_{\mathrm{GaN}}$ is set by the material system. In fact, the minimal thickness, where the inequality $E_{3D} < E_{2D}$ holds, will be the critical thickness for the 2D-3D transition (h_{2D-3D}). Islanding implies a sufficient adatom diffusion length, which depends mostly on T_S and the GaN growth rate (V_{GaN}). Therefore, the transition is kinetically limited and higher T_S leads to faster islanding, as demonstrated by Damilano *et al.* [128]. As previously mentioned, the growth of GaN on AlN can lead to both a FM and a SK growth, and will be determined by $\Delta\gamma$. Under typical growth conditions

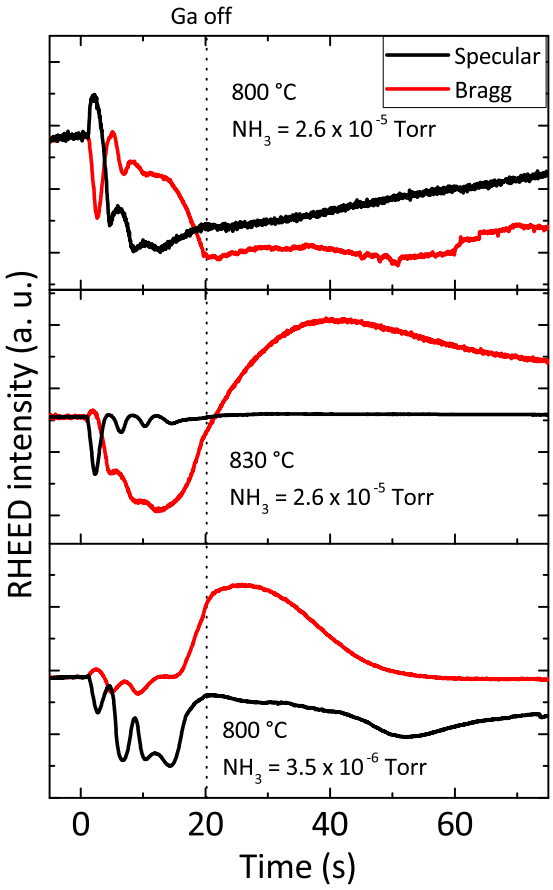

Figure 3.2 – RHEED intensity at the specular and Bragg spot positions during the growth of GaN on AlN. Under a high NH_3 flow the layer remains 2D (top), the transition into 3D islands can be promoted by either raising the temperature (middle) or reducing the NH_3 flow (bottom).

for GaN by NH_3-MBE, the layer follows a FM growth. This behavior is found for a wide range of temperatures [53]. In the framework of m-SK, the transition into 3D islands was found to be only possible when shuttering the NH_3 flow. Which leads to the conclusion that $\Delta\gamma$ is reduced under vacuum. Actually, it could be thought as $\Delta\gamma$ being proportional to the NH_3 pressure. It should be noted that the decomposition rate of GaN under vacuum is non-negligible for $T_S > 750°C$, a process which can be partially prevented by supplying NH_3. The rate of GaN decomposition as a function of temperature and NH_3 flux is given in figure 3.1.

A set of experiments are presented to experimentally evidence the energetic balance. One possibility to overcome the energetical barrier of the surface energy is by raising T_S. As illustrated in figure 3.2, with $T_S = 800°C$ and a NH_3-BEP of 2.6×10^{-5} Torr, the growth starts by a layer by layer growth mode, since RHEED intensity oscillations are

visible, and after 3 MLs these oscillations stop. However, the layer stays 2D as evidenced by the constant intensity of the Bragg spot. Raising the temperature to 830 °C provides the necessary diffusion length to promote the 2D-3D transition. Once again, RHEED intensity oscillations are observed for the first 3 MLs, then the oscillations stop and the Bragg spot intensity increases. The intensity of the Bragg spot continues to increase even after the GaN growth has been stopped, the transition is still kinetically limited. Alternatively, keeping the initial T_S of 800 °C, but decreasing the NH_3-BEP to 3.4 × 10^{-6} Torr, also promotes the 2D-3D transition. Shortly after the growth is stopped, the Bragg spot intensity decreases; the GaN QDs evaporate because the NH_3 flow is not high enough to prevent it.

The previous considerations and experimental data can be summed up into the following guidelines to identify the growth conditions to achieve a SK growth mode:

I. T_S should be increased to maximize the diffusion length. However, above 750 °C evaporation of GaN will also take place leading to an effective growth rate:

$$V_{effective} = V_{growth} - V_{evaporation}(T_S) \tag{3.3}$$

II. The NH_3 flow should be minimized, as $\Delta\gamma$ depends on the NH_3 pressure. High NH_3 flows can completely hinder the 2D-3D transition.

III. V_{GaN} should be low enough to allow the necessary formation time for a given $\Delta\gamma$ and T_S. This also ensures N-rich conditions, even when decreasing the NH_3 pressure.

3.2.2 Phase diagram for SK growth

Further experiments were performed to establish the growth window and phase diagram for the spontaneous transition into SK islands. The growth was monitored by RHEED and V_{GaN} set to 0.025 ML/s. In figure 3.3, the resulting surface morphology is plotted as red dots when an SK growth mode was observed and as black crosses for a streaky RHEED pattern signaling a 2D morphology. Three regimes can be discerned:

1. Under high NH_3 pressures and low T_S, the growth proceeds in a FM regime (Shaded blue).
2. With increasing T_S and a low NH_3 pressure $V_{evaporation}$ prevents the layer from reaching h_{2D-3D}. The boundary of this regime will depend on V_{GaN} (Shaded green).
3. A narrow growth window is left where SK growth is observed (White).

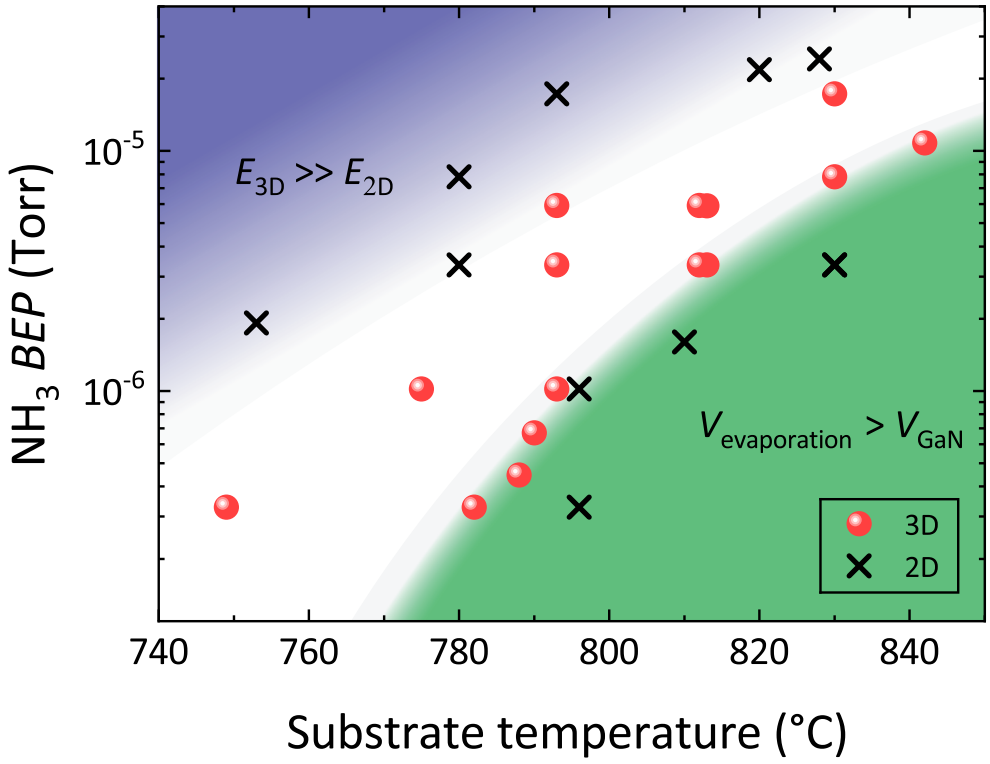

Figure 3.3 – Phase diagram of the surface morphology during the growth of GaN on AlN in terms of T_S and NH_3-BEP for a growth rate of 0.025 ML/s. Adapted from reference [31].

The size and density of the resulting QDs will be determined by the diffusion length, which in turn depends on V_{GaN} and T_S, and h. With the aim of reducing the QD density, a higher diffusion length will be required as it increases the probability for an adatom to attach at an existing QD site instead of nucleating a new island. However, the evaporation of GaN sets an upper boundary to T_S. Therefore, in order to have a higher reproducibility and allow for the increase in the diffusion length by means of reducing V_{GaN}, T_S was set to 750 °C and the NH_3-BEP to 3.3×10^{-7} Torr for all the following experiments. These growth conditions will be referred to as standard QD growth conditions for GaN SK-QDs.

In figure 3.4, the characteristic RHEED intensity curves and diffraction patterns during the growth of GaN on AlN under standard growth are displayed. The growth begins by a layer by layer growth, as evidenced by the RHEED intensity oscillations. The Bragg spots also display oscillations, albeit with a phase of π relative to the specular beam. The RHEED diffraction pattern remains streaky throughout the first 3 ML. After 3 ML, the oscillations stop and the Bragg spot starts to increase in intensity. Further deposition of GaN leads to a clear spotty pattern, signature of 3D islands. Note that the transition occurs spontaneously without any growth or NH_3 interruption. Hence, a conventional

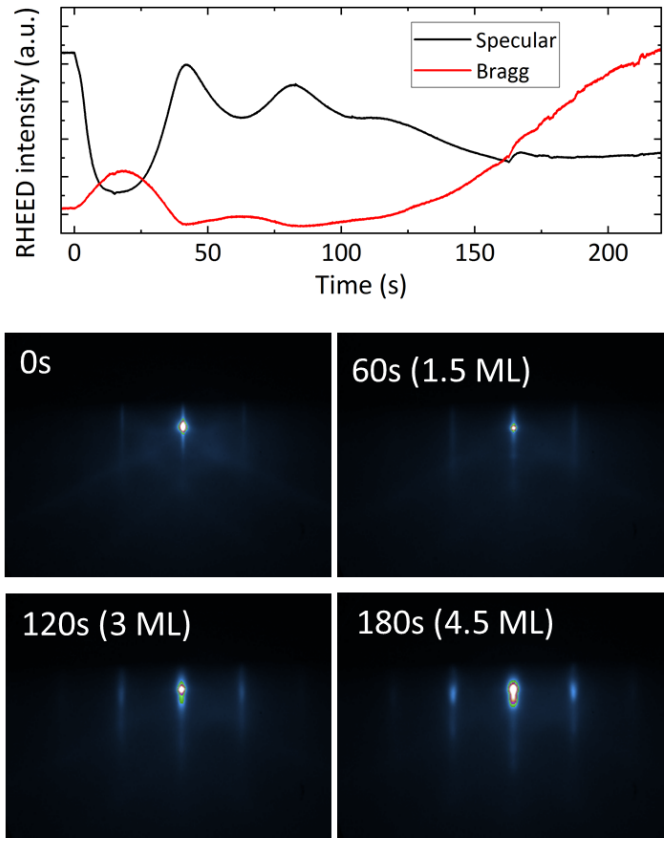

Figure 3.4 – RHEED intensity curves and RHEED diffraction pattern at the different stages of the the growth of GaN on AlN using standard QD growth conditions.

SK growth can be achieved by NH_3-MBE.

3.3 Dependence on the equivalent GaN thickness

Theoretical predictions by energy minimization, as well as, the RHEED intensity curves suggest a h_{2D-3D} of 3 MLs. However, in PA-MBE, h_{2D-3D} is reported to have a value of 2.5 MLs [25]. We have used AFM to study the initial stages of the formation of GaN SK-QDs, as well as the morphological features as a function of the deposited thickness. The experiments consisted in depositing GaN on AlN/sapphire templates under standard growth conditions and stopping the growth at a given thickness, followed by a rapid quenching of T_S. As seen in figure 3.5, at a thickness of 2.9 MLs (Fig. 3.5 (a)) the layer remains smooth and 2D, clear atomic terraces can be seen. Thus, as RHEED suggested, up to this thickness the growth proceeds in a layer by layer growth mode. Furthermore, some areas are a few ML thicker and are about to transition into 3D islands. Just beyond h_{2D-3D}, small islands are visible (Fig. 3.5 (b)). The density was estimated to be $3{\times}10^9$ cm^{-2}. The heights range from 0.75 up to 1.5 nm and the diameters from 10-20 nm.

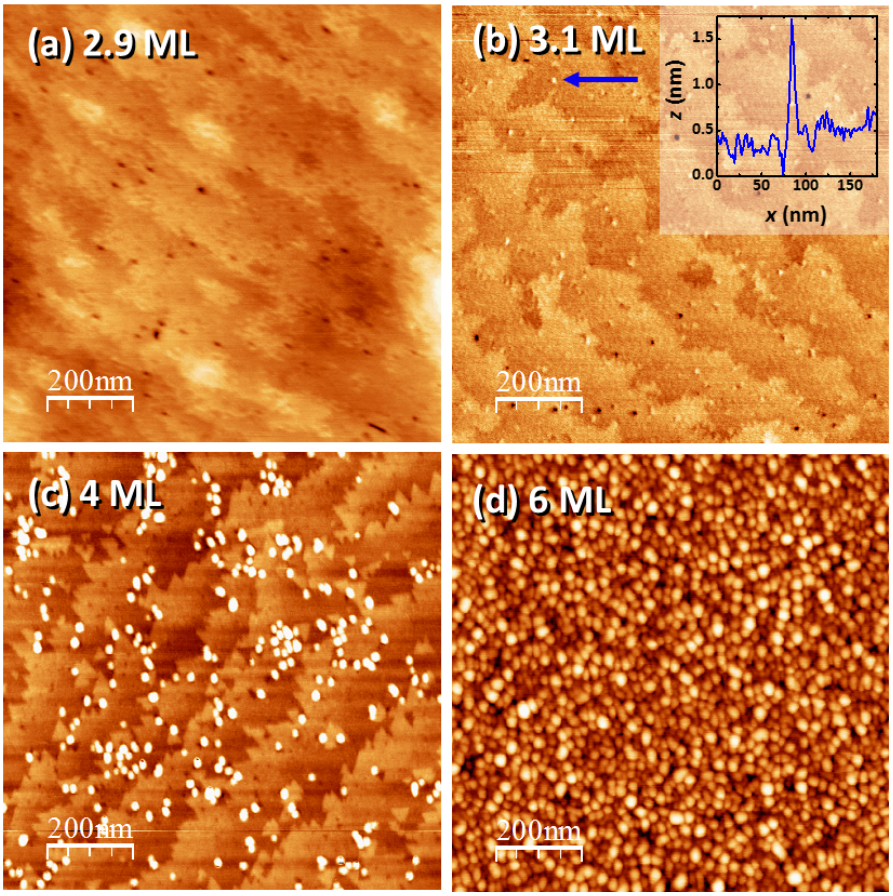

Figure 3.5 – 1×1 μm^2 AFM images of GaN on AlN with the equivalent GaN thickness given in ML. No island is observed in (a) whereas small islands are seen in (b), confirming $h_{2D-3D} = 3$ ML. At a thickness of 4 ML (c), clear and distinct islands can be observed. If h is further increased the surface becomes fully covered by islands (d). Inset: Profile over an exemplary island marked by the blue arrow.

Upon further increasing h, the islands grow both in size and density. At $h = 4$ MLs, see figure 3.5 (c), well defined islands can be observed. The islands density is about 2×10^{10} cm^{-2}, and the average height and diameter are 2.5 and 25 nm, respectively. Notice that the islands tend to either nucleate at terrace edges or to cluster at certain locations. Additional increase of h yields a very high dot density and a complete coverage of the surface by QDs (see Fig. 3.5(d)), with a density up to $\sim 10^{11}$ cm^{-2}. Additionally, the size of the islands remains somewhat homogeneous for each coverage, even for $h = 6$ ML. In contrast, the InAs/GaAs system only shows mostly uniform QD sizes at the initial stages, i.e. small coverages. Notice that strain relaxation in a lattice mismatched system can occur by means of dislocated islands. Once formed, these incoherent islands grow in size without restriction, and are observed by AFM as much larger islands [137, 138]. Interestingly, the surface does not show extremely large islands at any of the growth coverages, which could be associated to plastically relaxed islands.

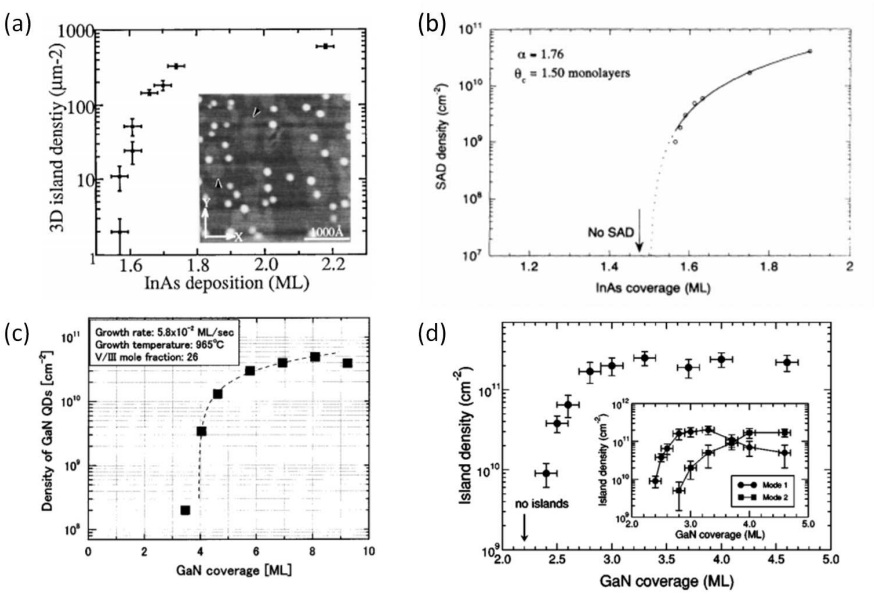

Figure 3.6 – Quantum dot density as a function of coverage for InAs/GaAs (a) and (b) and for GaN/AlN (c) and (d). The GaN/AlN growths were achieved by MOVPE (c) and PA-MBE (d). Adapted from references: (a) [136], (b) [137], (c) [28] and (d) [30].

The equivalent thickness (h or coverage) is often used to change the density and size of the QDs. The common trend, is a decrease of the QD density and size for reduced coverages. However, the slope of the density becomes very steep near h_{2D-3D}, a feature that is observed with different material systems and growth techniques [28, 30, 136, 137]. As illustrated in figure 3.6, densities in the order of 10^8 cm^{-2} are challenging to achieve through this method as small deviations in h will either lead to no islands or a much higher density. A different approach towards controlling the QD density relies on changing the diffusion length. In this way, in conjunction with choosing the appropriate h, one should be able to independently change the size and the density of the QDs [139].

3.4 QD growth on AlN single crystal

With the proper SK growth regime established, controllable and reproducible experiments are feasible, allowing us to explore the possible paths towards achieving low density QDs for single dot spectroscopy and single photon emission. As we have mentioned, reducing the amount of deposited GaN can reduce the density of QDs, but the trends in QD density as a function of coverage reveal a very sharp transition from nearly no QDs to a high density. Therefore, we have explored an alternative strategy, consisting of increasing the diffusion length. Increased diffusion lengths promote the incorporation of adatoms into existing islands instead of nucleating new ones.

A series of GaN QD samples were prepared using standard growth conditions, but with

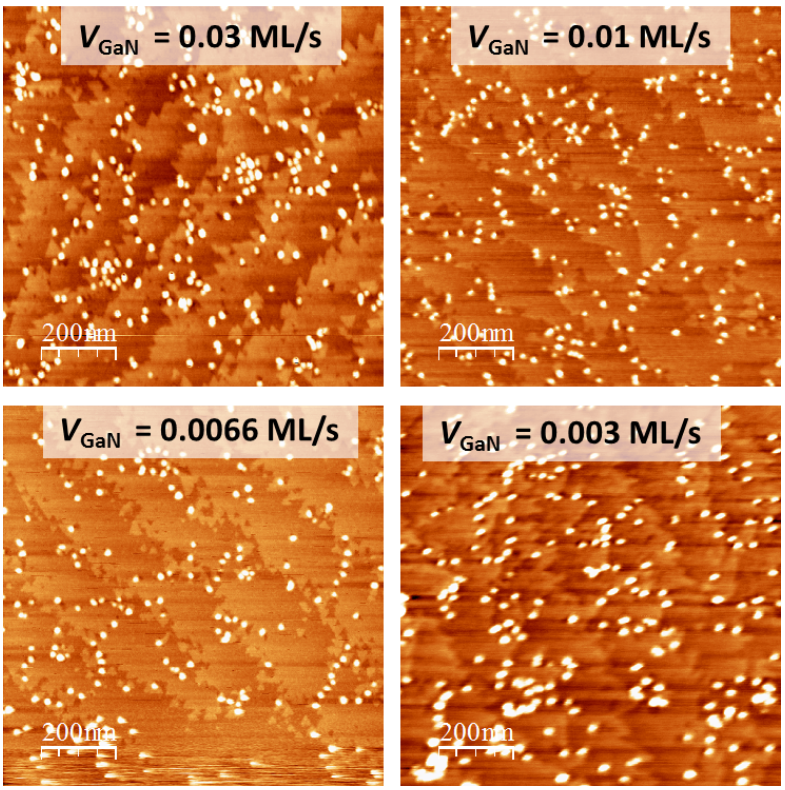

Figure 3.7 – 1×1 μm^2 AFM images of GaN QDs on AlN/sapphire templates grown under standard conditions and variable V_{GaN}.

a variable V_{GaN}. V_{GaN} was varied from 0.001 ML/s to 0.03 ML/s. The growth rate was measured for each sample from the RHEED curves from the oscillations during the first 3 MLs. For extremely low V_{GaN}, oscillations are almost completely absent since the growth proceeds in a step flow growth mode. In this case V_{GaN} was estimated from the 2D-3D transition and the corresponding increase in the Bragg spot intensity. The accuracy with which V_{GaN} could be estimated is conveyed in the error bars of figure 3.12. The initial series of samples were grown on AlN/sapphire templates and h was set to 4 MLs. The resulting morphologies are depicted in figure 3.7. Although V_{GaN} has been changed by one order of magnitude, the size and density of the QDs remain somewhat constant, contrary to the expected reduction of QD density and increase in QD size. Upon further inspection of the AFM images, pits next to the QDs are observed[2]. They are identified as edge dislocations, see figure 3.8 (c). Edge dislocations were identified as preferential nucleation sites for GaN QDs in 1997 by Rouvière *et al.* [140]. These dislocations form a strain dipole [141] and thus provide a local strain minimum for the QD nucleation. In our case, the diffusion length gained by decreasing V_{GaN} is counteracted by the strain induced nucleation provided by the dislocation, hence the QD density becomes fixed by

[2]Imaging the pits located next to the dislocations requires extremely sharp AFM tips, and thus the effect is not visible in all AFM images.

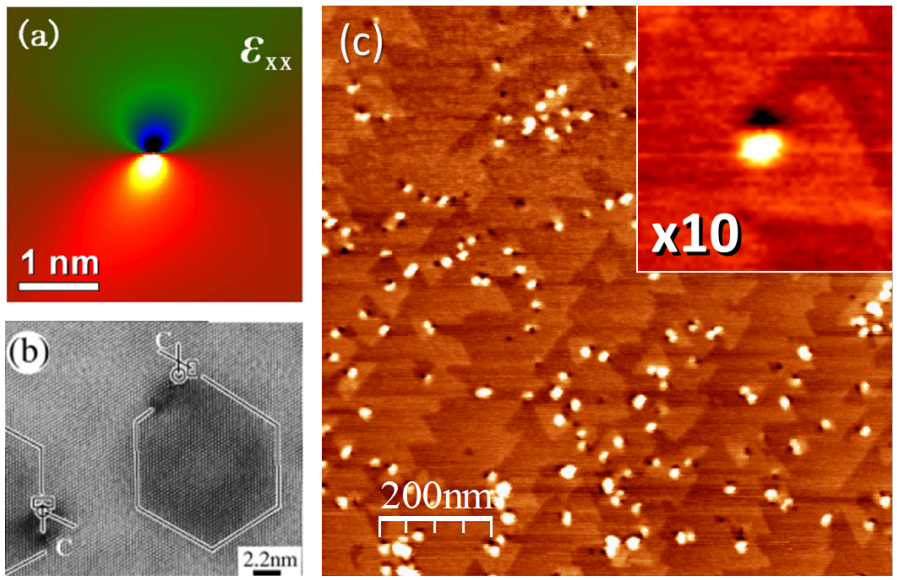

Figure 3.8 – (a) Strain field, extracted from HRTEM measurements, due to an edge dislocation. Adapted from Ref. [141]. (b) TEM image showing a GaN QD nucleating at the edge of an edge dislocation. Adapted from Ref. [140]. (c) 1×1 μm^2 AFM image of GaN QDs on AlN/sapphire templates grown with V_{GaN} = 0.001 ML/s. Inset: ×10 magnification from the AFM image, showcasing a dislocation and a dot.

to the dislocation density. Therefore, getting rid of the dislocations should provide an homogeneous strain potential landscape allowing a low QD density.

Recent progress in bulk nitride growth has led to commercially available native III-nitride substrates (AlN) and pseudosubstrates (GaN). The use of AlN single crystal substrates with a TDD of $\sim 10^3$ cm^{-2} enabled the study of the nucleation of QDs in the absence of structural defects.

3.4.1 Temperature calibration

Due to the high cost of AlN single crystal substrates, they were cut into 5 × 5 mm^2 square pieces. A series of technical challenges had to be overcome in order to use these small pieces of AlN single crystals as substrates, which are discussed in the Appendix B. A notable one is the determination of T_S. Reliable and fast measurement of T_S during MBE can be achieved by means of pyrometric measurements, which rely on the Stefan-Boltzmann law:

$$j* = \varepsilon\sigma T^4, \tag{3.4}$$

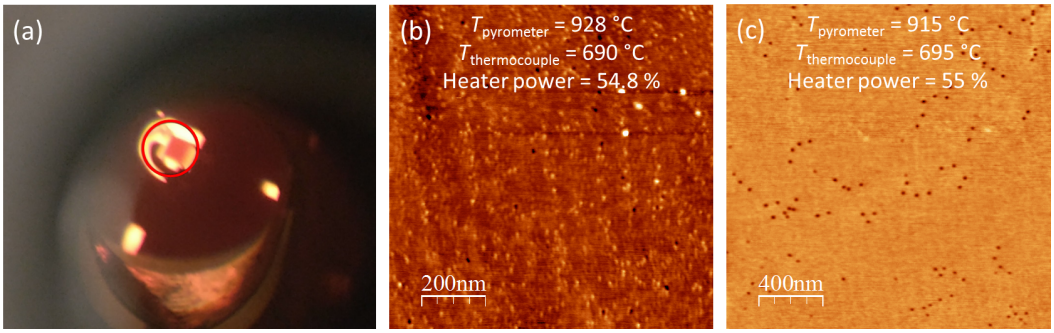

Figure 3.9 – (a) Photography of the sample mounted on the spring holder through the pyrometer's window. (b) and (c) 1×1 μm^2 AFM images of attempts at growing GaN QDs on AlN single crystal. In (b), high density small QDs can be observed, meaning that T_S is below its optimum value. In (c) no QDs were found, which means that T_S was too high and hence led to the evaporation of GaN.

where $j*$ is the radiant emittance, ε is the emissivity, σ is the Stefan-Boltzmann constant and T is the temperature. A different ε is used depending on the material being measured; for example, for Si substrates ε = 0.69 - 0.71 and for Mo back-coated sapphire substrates ε = 0.36 - 0.39. In each of these cases, the measured area is much smaller than the substrate size and is thus homogeneous and at a constant temperature. This is not the case for the 5 × 5 mm^2 AlN single crystal samples. In figure 3.9 (a), a photography of the sample through the pyrometers window is shown. The red circle printed in the pyrometer's window delimits the probed area. The sample is clamped by a spring (see Appendix B). The color within the circle is not homogeneous, as different elements of the holder are at different temperatures. Thus, the pyrometer cannot be properly used. The situation is improved with the uniblock sample holder (see Appendix B), as in this case the emissivity can be adjusted to display the correct temperature. Nevertheless, the emissivity value will change for each sample, as the placement of the sample is not always exactly the same. A thermocouple is installed in the substrate heater, but the distance to the sample is too long for accurate measurements.

Figure 3.9 shows two attempts at growing QDs on AlN under standard conditions and the corresponding temperature measurements and output power of the substrate heater.[3] The AFM from figure 3.9(b) exhibits a high density of very small islands, T_S was high enough to promote the 2D-3D transition, but too low to enhance the diffusion length. The sample from figure 3.9(c) has no islands, T_S was too high. GaN decomposes leaving a smooth surface. Notice that the pyrometer and thermocouple readings are not consistent, and the furnace's output power was only increased by 0.2%. Hence, T_S of AlN single crystal has to be calibrated for each sample. Furthermore, for most MBE growth purposes an accuracy in T_S of ± 10-20 °C is acceptable. However, for GaN QD growth, reproducible

[3]Pits can be observed on the samples surface, which are likely due to the extensive number of *ex situ* and *in situ* experiments realized on this particular piece which have degraded its quality.

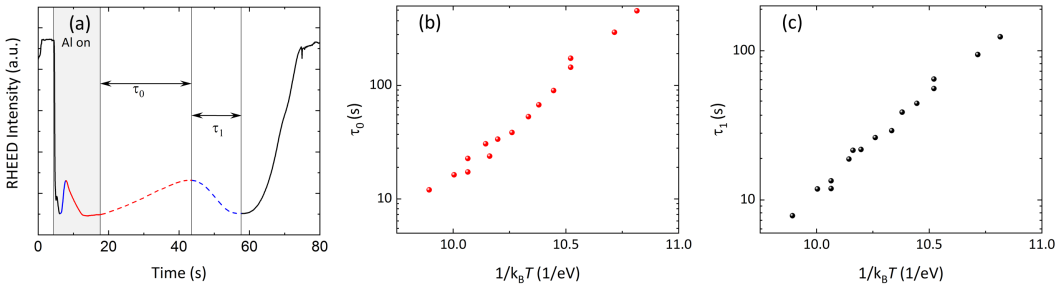

Figure 3.10 – (a) RHEED intensity curve of the specular beam during the deposition of Al on AlN under vacuum. (b) and (c) Evaporation rate of Al, in terms of τ_0 and τ_1 as defined in (a), measured on AlN/sapphire templates.

growths can only be achieved if T_S is determined within a precision of a few °C, especially when aiming at low V_{GaN}.

Temperature measurement by Al evaporation

Since, the thermometer in the MBE system is not well suited for the measurement of T_S when growing on the small AlN single crystal substrates, alternative techniques had to be devised for the calibration of T_S. An approach consists in the congruent evaporation of Al from the AlN surface.

The experiments are the following: in exposing the AlN surface is first exposed to an Al beam under vacuum. During the deposition of Al, the AlN surface exhibits several surface reconstructions depending on the amount of Al[142]. Here we did not focus on identifying the surface reconstructions, but rather on the fact that the RHEED specular intensity curves are reproducible within the range of interest of T_S. The typical RHEED intensity curve during the deposition and subsequent evaporation of Al under vacuum is displayed in figure 3.10(a). During the first stage of the experiment, when the Al cell is opened, an abrupt decrease of the RHEED intensity is observed, followed by an asymmetric oscillation and finally a low intensity plateau. If the Al cell is kept open, no further changes in the intensity occur. Once the Al cell is closed, the same curve is observed in reverse, the speed at which this evaporation is observed can be modeled by an Arrhenius equation:

$$V_{evaporation} = Ae^{-E_a/k_BT} \tag{3.5}$$

The time from the closing of the Al cell and the maximum RHEED intensity was labeled as τ_0 (dashed red line in figure 3.10 (a)), and the time from the maximum to the valley as τ_1 (dashed blue line in figure 3.10 (a)). The experiment was performed on AlN/sapphire

templates for which T_S is readily available and repeated with different T_S. The resulting τ_0 and τ_1 as a function of $1/k_BT$ are plotted in figure 3.10(b) and (c), respectively. Then, by repeating the experiment on AlN single crystal pieces, T_S can be estimated by comparing τ_0 and τ_1.

3.4.2 QD density control

A series of samples was grown on AlN single crystal with varying V_{GaN}. As opposed to AlN/sapphire templates, the lack of dislocations in AlN single crystals allowed us to control the QD density from 10^8 up to 10^{11} cm^{-2} while keeping $h = 4$ MLs. The AFM images in figure 3.11 showcase the density control. The scanned area is 1×1 μm^2 for (a) and (b), whereas for (c) a 2×2 μm^2 area is displayed. Even though the nucleation is no longer mediated by dislocations, the QDs still nucleate at sites providing a strain minimum; in this case, at the atomic step edges.

The results of the sample series on AlN/sapphire templates and on AlN single crystal are summarized in figure 3.12. Thanks to the close to featureless strain potential landscape, a strong dependence of the QD density is achieved when growing on AlN single crystal.

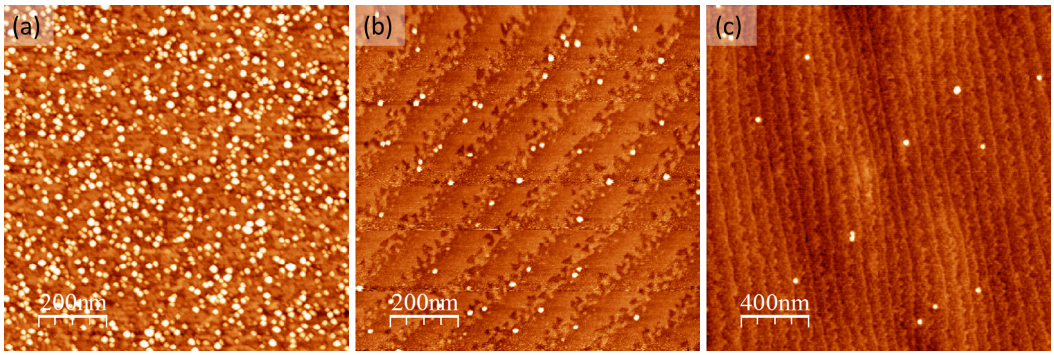

Figure 3.11 – AFM images of GaN QDs grown on AlN single crystal with varying V_{GaN}. The density and growth rates are respectively: (a) 7.9×10^{10} cm^{-2} and 0.09 ML/s, (b) 5.6×10^9 cm^{-2} and 0.006 ML/s and (c) 4×10^8 cm^{-2} and 0.003 ML/s.

3.5 Low QD density by ripening and evaporation

Even though a solution has been demonstrated to obtain low density GaN QDs by means of reducing V_{GaN} in the absences of dislocations, it is desirable to also achieve low density QD samples on substrates other than AlN single crystal. The motivation for switching from AlN single crystal is threefold: the high cost of AlN single crystals renders them impractical for mass use. Secondly, all AlN films display sub-bandgap emission primarily due to point defects, an effect that is particularly important with the AlN substrates as the intensity of the emission is proportional to the density of point defects and the excited

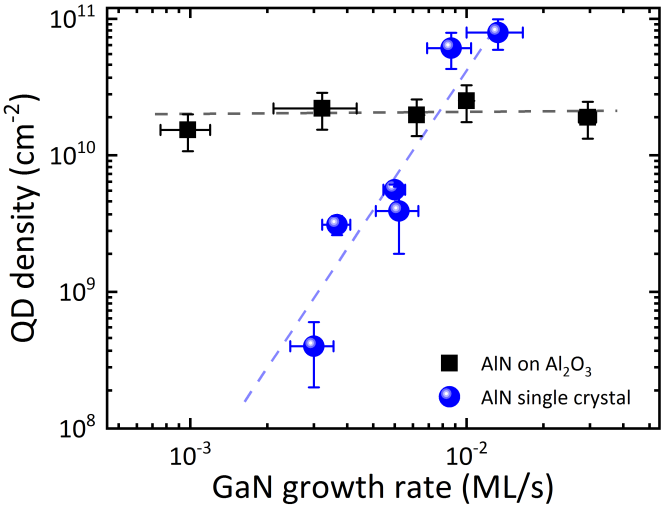

Figure 3.12 – QD density as a function of V_{GaN} for AlN/sapphire templates and AlN single crystals. The dashed lines are guides to the eye. Adapted from ref. [31]

.

volume. Finally, the use of AlN substrates does not provide any etching selectivity for the fabrication of membrane PhC. Therefore, we have considered alternative paths towards low density GaN QDs compatible with high TDD AlN underlayers.

Theoretical calculations for the self organization of nanostructures predict that for a given strain energy, island formation energy and a fixed h, there is an optimum island volume. Thus, as the system tends towards equilibrium, the islands will exchange material in an attempt to homogenize their size [118].

Our approach consists in growing a layer of GaN QDs at a slightly higher temperature, such that very slow GaN evaporation can occur. Once $h = 4$ MLs, the Ga flux is shuttered and the sample is kept under the same NH_3 atmosphere. Due to the slow evaporation of GaN, the island size start decreasing. However, in order to minimize the system's energy, islands will exchange atoms, feed from the WL or merge to maintain sizes close to the optimum. As a result, QDs of similar heights and diameters are expected, but because the total amount of GaN on the surface is lowered, the QD density decreases. The ripening time t_r during which the islands were allowed to evolve and GaN to evaporate was varied while T_S was set to 756 °C. In figure 3.13(a) we plot the QD density as a function of t_r. We can observe that the QD density is decreasing as the film is left to evolve under these conditions. Most importantly, QD densities below the TDD can be achieved in this way. Figure 3.13(b) showcases the low density of QDs estimated at 3×10^9 cm^{-2}, while a TDD of 1.8×10^{10} cm^{-2} is estimated from the pit density in AFM images. Therefore it is possible to obtain low QD densities even on highly dislocated AlN layers. It should be noted, that the QDs still reside fixed next to the dislocations.

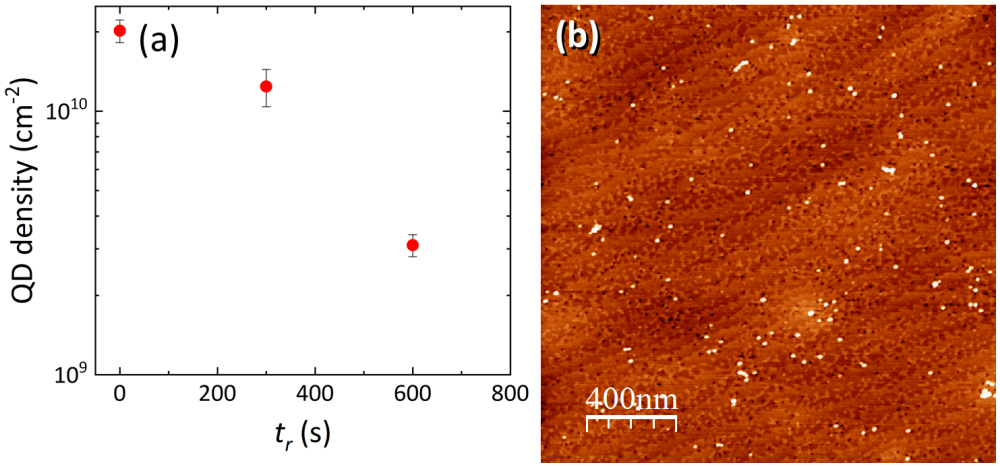

Figure 3.13 – (a) QD density as function of ripening time grown on AlN/sapphire templates. A density of 10^9 cm^{-2} can be achieved with this strategy, which is lower than the TDD density (10^{10} cm^{-2}). (b) 2 × 2 μm^2 AFM image of the sample with a ripening time of 600 s.

Additionally, the morphology of the WL appears to evolve under ripening. In figure 3.14, 1 × 1 μm^2 AFM images of ripened QD layers grown on (a) AlN/sapphire template and (b) AlN single crystal, are displayed. We can observe that the areas lacking QDs show incomplete atomic terraces and a dendritic shape as opposed to all previous AFM scans displayed in this chapter. It could be therefore conceivable that the thickness of the WL is being reduced as it either evaporates or feeds the QDs. As will be seen in the upcoming chapter, a thin WL is desirable as it pushes the emission energy of the WL to higher energies. Then, a larger background-free energy window for single QD spectroscopy can be achieved.

3.6 QD size distribution

It is often advantageous to have a small distribution of QD sizes and hence a narrow inhomogeneous broadening of the QD ensemble luminescence. The distribution of QD sizes is compared between two samples grown either on AlN/sapphire or on AlN single crystal. For an accurate quantification of the QD sizes, low noise AFM images and extremely flat AlN surfaces are required. The selected AFM images are displayed in: figure 3.5(c) and figure 3.11(b). The maximum height and perimeter of each individual QDs was extracted from the AFM images and the QD diameter calculated from the perimeter assuming a circular base.

We can observe that when growing on AlN single crystal, the size of the QDs is much more uniform, both in terms of height and diameter, than when growing on AlN/sapphire. This is most likely due to the difference in strain homogeneity between the AlN layers,

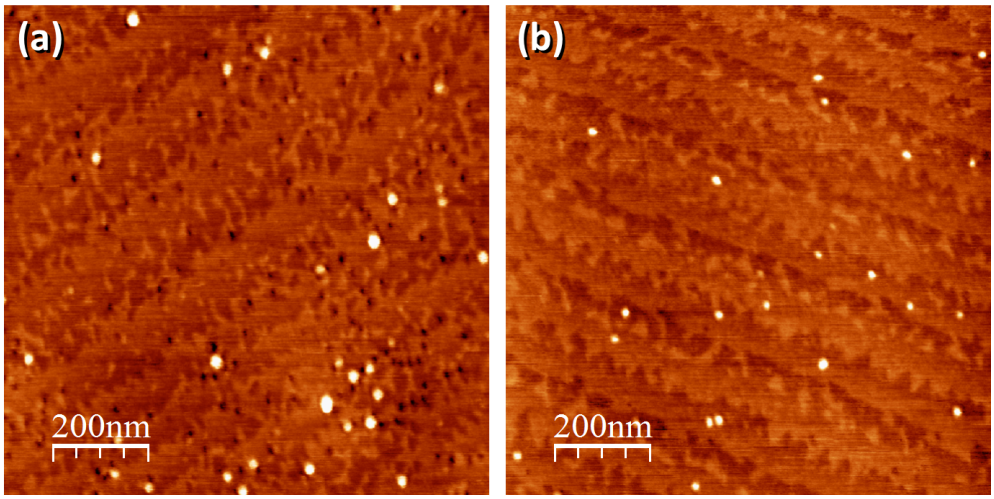

Figure 3.14 – 1 × 1 μm^2 AFM images of QD samples with reduced density by ripening on (a) AlN/sapphire and (b) AlN single crystal, displaying the dendritic nature of the WL.

the strain minima when growing on single crystal are the step edges, whereas when growing on AlN/sapphire these are the dislocations. The strain field of a dislocation extends to several microns[143], hence, for a particular dot, the exact spatial distribution of dislocations will determine the effective strain field and thus the optimum QD size.

Another parameter that could explain the difference in size distributions is the growth rate. The QD size distribution can be further modified by changing the growth rate, as shown in the InAs/GaAs system, see figure 3.16 [144]. When the growth rate is reduced, the PL in figure 3.16 is red-shifted, as expected from a reduction of the QD density at the expense of an increase in the QD size. Simultaneously, there is a narrowing of the PL linewidth from 44 to 27 meV implying a more uniform QD size distribution. A possible explanation for this behavior is the following: for a given lattice mismatch and coverage, there is an optimum island size [118]. To arrive at the optimum island size the system has to achieve thermodynamical equilibrium, but MBE growth is an out of equilibrium process. Nevertheless, by reducing the growth rate, the system is allowed more time to approach equilibrium and hence for the islands to approach their optimum size. A dependence of the QD size on the growth rate suggests a kinetically governed process.

Another growth parameter capable of influencing the QD size distribution is the growth temperature. According to the equilibrium theory developed by Shchukin *et al.*, entropy can play a role in the number of atoms per island, i.e., the island size [145], see figure 3.17 (a). The Helmholtz free energy of the system will be influenced by entropy contributions, which favor the formation of smaller islands at higher temperatures. At low temperatures the system will start from a narrow distribution of nanometric islands (see curve 1 in figure 3.17(a) and the top panels of figure 3.17(b)) and then spread into a bimodal

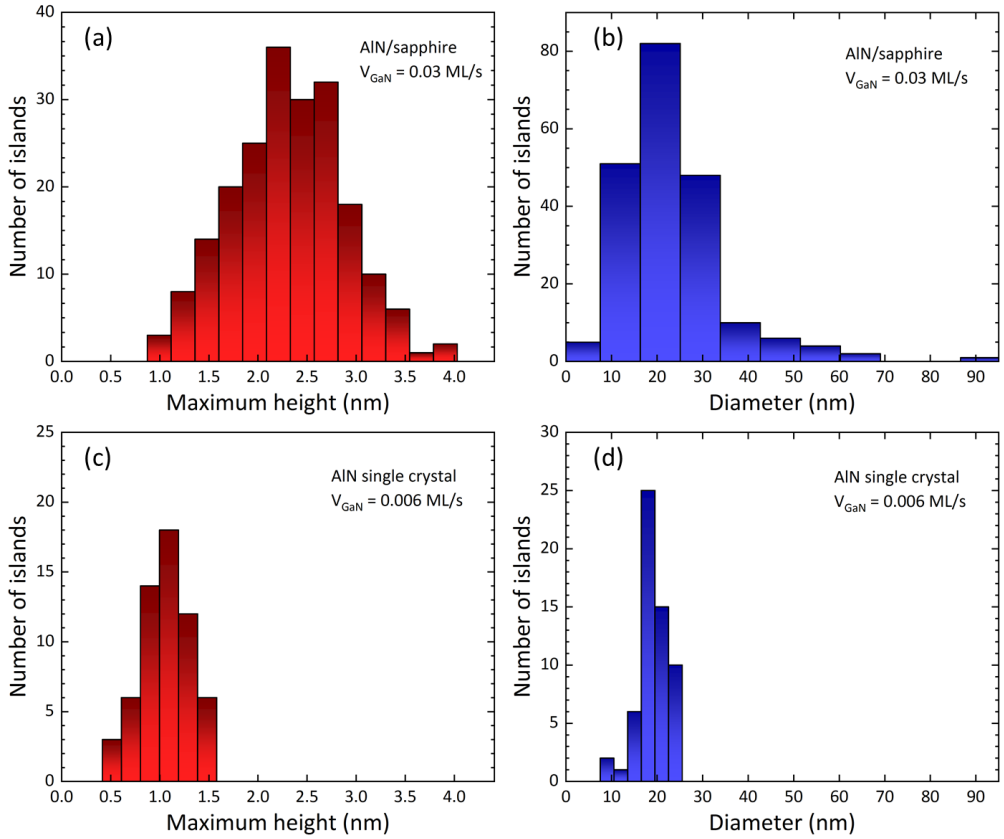

Figure 3.15 – Histogram of the number of islands as a function of the maximum QD height and diameter for the growth on AlN/sapphire templates (a) and (b) and on AlN single crystal substrate (c) and (d).

distribution when the temperature is raised, as was confirmed experimentally for GaN QDs by Adelmann *et al.* [30]. According to the calculation, if the temperature is further raised, the islands will tend to a single atom size (curve 6). It should be noted that the calculation was performed without considering strain.

In conclusion, three distinct parameters have an impact on the distribution of the QD sizes: strain, growth rate and entropy via the substrate temperature. Interestingly, in other segregation models [146], growth rate and substrate temperature are tightly intertwined; raising the substrate temperature has the same effect as lowering the growth rate. In contrast, here we have seen that lowering the substrate temperature and lowering the growth rate will both lead to more uniform QD sizes. Actually, it can be seen that even if the main PL peak in figure 3.16 becomes narrower, an additional peak appears at higher energies hinting towards a bimodal distribution, as predicted by the equilibrium model. Therefore, the system can only be accurately described by considering both the kinetic regime and equilibrium theory.

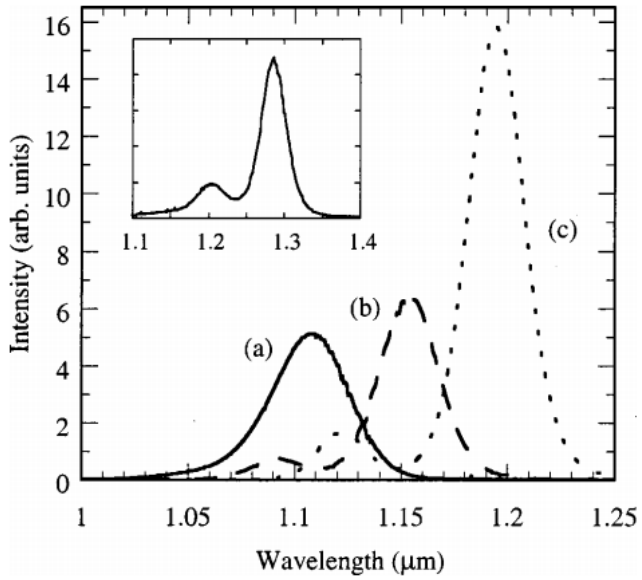

Figure 3.16 – Low temperature PL spectra of InAs/GaAs QDs with growth rates of (a) 0.55, (b) 0.016, and (c) 0.0065 ML/s. The equivalent thickness and growth temperature are constant. Reproduced with permission from [144].

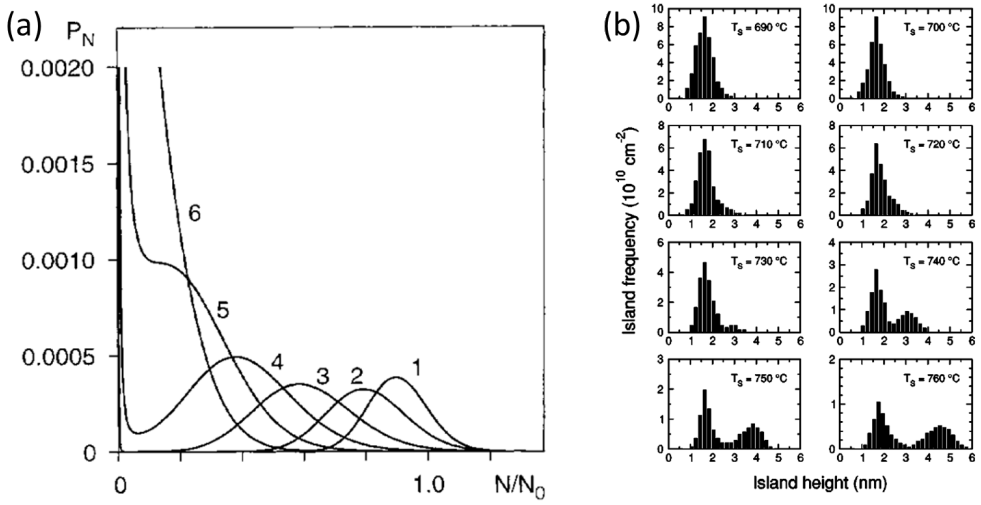

Figure 3.17 – (a) Normalized areal concentration of islands, the different curves and their corresponding numbers are for calculations with different temperatures in terms of $k_BT/\Theta = 0.005$ (curve 1), 0.01 (curve 2), 0.02 (curve 3),0.03 (curve 4), 0.04 (curve 5), and 0.05 (curve 6), where Θ is the energy of the optimum islands. (b) Distribution of GaN QD heights as a function of the growth temperature. Reproduced with permission from [145] and [30].

4 Spectroscopy of GaN Quantum Dots

This chapter focuses on the optical properties of GaN QDs and the impact of the different growth conditions on the implementation of GaN QDs for SPE. First we analyze ensembles of QDs. Then the focus is shifted towards single QD spectroscopy. Linewidth statistics of individual QDs, power-dependent measurements, polarization and temperature series of individual QDs are presented. The chapter is concluded with the successful measurement of SPE at room temperature. Finally, we estimated the absolute number of photons emitted by the QD.

4.1 State of the art

Once the first growths of GaN/AlN QDs were achieved in the late 1990's [1, 27], a wide range of emission energies were demonstrated, even below GaN's bandgap. The strongly redshifted optical emission in large QDs was soon described to originate from the QCSE. This was further proven by time resolved photoluminescence [147, 148]. The first reports of single QD spectroscopy was in 2004 when single GaN QDs were isolated by etching microscopic mesa structures [149]. In this way, exciton (X) and biexciton (XX) luminescence were possible to discern. The biexciton is the simultaneous occupation of two electrons and two holes within the QD. Further studies of multi excitonic complexes were reported by Kako *et al.* and the XX transition was identified by power dependent measurements and second order cross correlation photon statistics [150]. The binding energy of biexcitons as a function of QD size and aspect ratio was studied by Simeonov *et al.* [32]. The binding energy of the biexciton represents the energy difference between two independent excitons and the XX complex. As such, it sums up the interaction between the two excitons. The general trend of the biexciton binding energy is a decrease in the binding energy with increasing QD size (figure 4.1). Due to the QCSE, the electrons and holes will be spatially separated along the c axis. For large QDs, the repulsive Coulomb interaction between electron and hole pairs increases with the spatial separation between opposite charges, leading to a decreased binding energy. In contrast, for decreasing QD

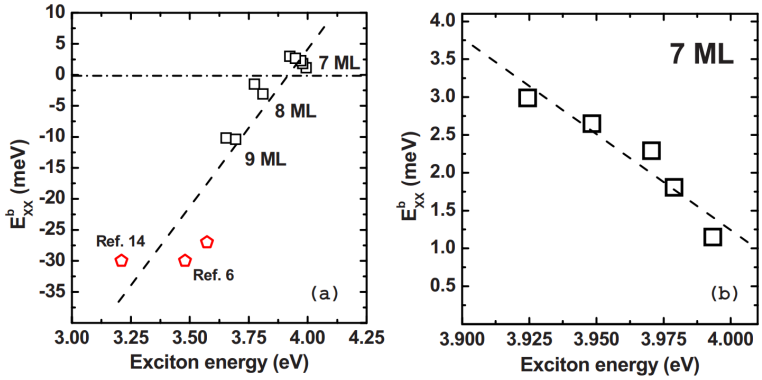

Figure 4.1 – Biexciton binding energy in GaN QDs as a function of QD emission energy. Adapted with permission from reference [32].

sizes the biexciton binding energy increases and can even become positive. Furthermore, for a fixed QD height, an increase in the lateral confinement will lead to a decrease in the binding energy as the repulsive Coulomb interaction increases. Further understanding of the XX was derived by Hönig *et al.* [151] in terms of a hybrid XX which is discussed in detail later in this chapter. Along with the XX, other properties have been studied, such as: linewidths [36], fine structure splitting [152], spectral diffusion [153, 36, 154], phonon interactions [155, 156] and temperature dependence of the emission [157, 158, 159].

One of the main interests for III-nitride QDs is their application for SPE. In order to demonstrate SPE, an HBT interferometer is required. To the author's knowledge only four HBT setups in the short wavelength range exist worldwide: Tokyo[160], Berlin [151], Grenoble [158] and Lausanne. Hence, data on SPE in GaN QDs is scarce and most of the available data comes from Arakawa's group [26]. The field experienced an increase of interest following the demonstration of SPE at 200 K in 2006 [150]. As of today, SPE from GaN QDs has been demonstrated up to a temperature of 350 K [46]. Further on, the cleanest SPE for III-nitrides has been obtained from interface fluctuations in GaN QWs. The raw data yields $g^{(2)}(0) = 0.085$ at a temperature of 10 K [161]. Another interesting use of QDs is to produce entagled photon pairs, which can be obtained by the biexciton cascade [47].

4.2 Luminescence of an ensemble of QDs

Let us first address the luminescence of an ensemble of QDs. The PL of two samples consisting of 10 planes of GaN/AlN QDs is displayed in figure 4.2. The QDs were formed by the spontaneous SK transition discussed in chapter 3. The samples were grown on commercially available 1 μm thick AlN on sapphire templates grown by MOVPE. The spectra are dominated by a single broad peak, at either 4.45 or 3.6 eV, respectively. The spectra are further modulated in energy due to the Fabry-Perot cavity created by the

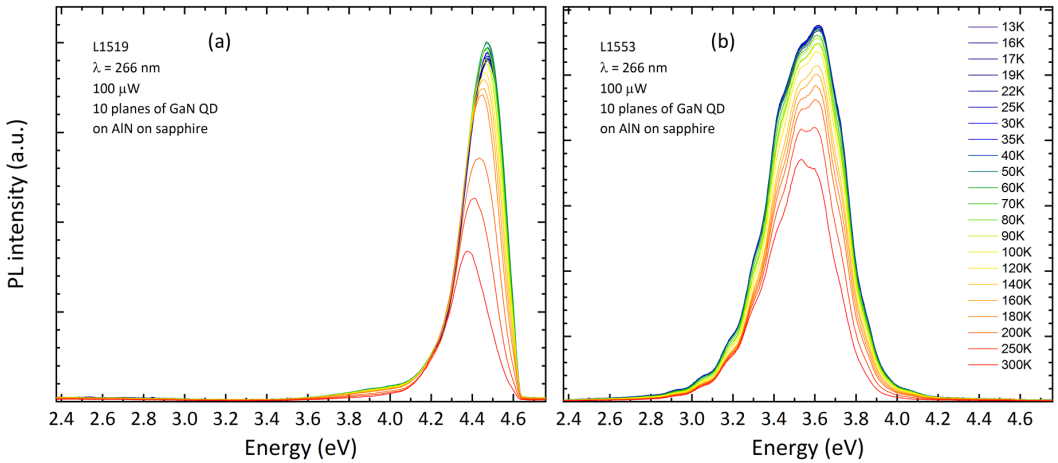

Figure 4.2 – Ensemble PL of 10 planes of QDs grown on AlN on sapphire templates as a function of the sample temperature. (a) Depending on the growth conditions the PL emission can be blue shifted up to 4.45 eV or red shifted with increasing dot size (b)

interface of the AlN with the sapphire and the interface between the AlN and vacuum. The emission energy is determined by the size of the QDs, which can be mostly controlled during growth by changing the equivalent GaN coverage h. However, as discussed in chapter 3, increasing the diffusion length will lead to a lower QD density at the expense of a dot height increase. Therefore, to obtain high density QDs emitting at high energy, such as the ones depicted in figure 4.2 (a), the diffusion length has to be decreased as well as h. A salient feature of all QD samples, and signature of the three-dimensional carrier confinement, is the thermal stability of the PL. The internal quantum efficiency (IQE) at 300 K, which can be roughly defined as the ratio of the PL intensity at that temperature over the PL intensity at low temperature, can be as high as 60 % at 300 K, see figure 4.2. Notice that the homogenous broadening due to phonon interactions expected to be on the order of 40 meV at 300 K, is much smaller than the inhomogenous broadening determined by the size distribution of the QDs, and as such is not detectable.

Further insight can be obtained by performing PL on a single plane of QDs. In this case the number of excited QDs is not as large and additional features are visible: the blue AlN defect band and the WL, which corresponds to a 3 ML thick GaN/AlN QW. As a first approximation, the overall signal intensity of the QDs can be considered as proportional to the number of excited QDs, or for a single plane of QDs proportional to the QD density. For samples grown under conditions leading to a high density of QDs, two features are commonly observed: a decrease in the intensity of the WL and an increase in the absolute QD signal intensity. Correspondingly, in samples with very low QD densities, the WL dominates the PL signal and very faint QD signal can be extracted.

An important feature of the temperature series presented in figure 4.3 is the more

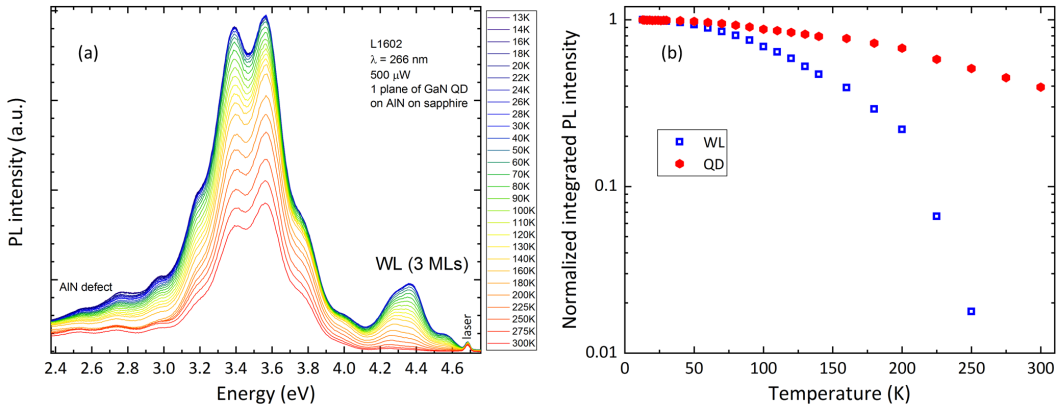

Figure 4.3 – (a) PL of a single plane of GaN QDs grown on an AlN/sapphire template as a function of sample temperature. The growth conditions should lead to an intermediate QD density in the order of 10^{10} cm^{-2}. (b) Normalized PL intensity of the QDs and the WL as a function of temperature.

prominent decrease in the intensity of the WL in comparison to the QDs. The normalized intensity of both peaks is plotted against temperature in figure 4.3, while the QDs loose only about 60% of their intensity from low temperature to 300 K, the signal from the WL rapidly drops and 98% of it is lost at 250 K. Although this result is well known and can be modeled by rate equations [162], it is an easy way to separate QW from QD features in the PL spectrum and to ensure that QDs are indeed present in the sample.

4.3 Single QD spectroscopy with AlN single crystal substrates

Perhaps one of the biggest challenges to resolve and address single GaN QDs by μ-PL is that the QD density is usually very high. Even after focusing the excitation laser spot size below 1 μm, several hundreds of QDs are probed, and individual QD lines become either inaccessible or intermixed with other QDs. As described in chapter 3, a procedure enabling the growth of very low QD densities was demonstrated when performing the growth on AlN single crystal substrates. A sample was grown with parameters that should lead to an extremely low density of QDs: the growth rate was reduced to 0.0015 ($\pm$ 0.0010) ML/s and h was also reduced to 3.5 MLs (the QD density trends presented in figure 3.12 utilized $h = 4$ MLs). The sample was capped with 50 nm of AlN. The capping procedure involved two AlN growth rates: first, 6 MLs of AlN were grown at the same T_S and the same NH_3-BEP as the QDs. Due to the low T_S and NH_3-BEP a rather low AlN growth rate of 0.011 ML/s was utilized. The rest of the AlN cap was grown with conventional growth rates (0.24 ML/s) and NH_3 flows (150 sccm), and T_S was gradually increased to 900 °C. This somewhat low value of T_S for the growth of AlN was chosen to avoid intermixing in the QD layer. No further fabrication was performed

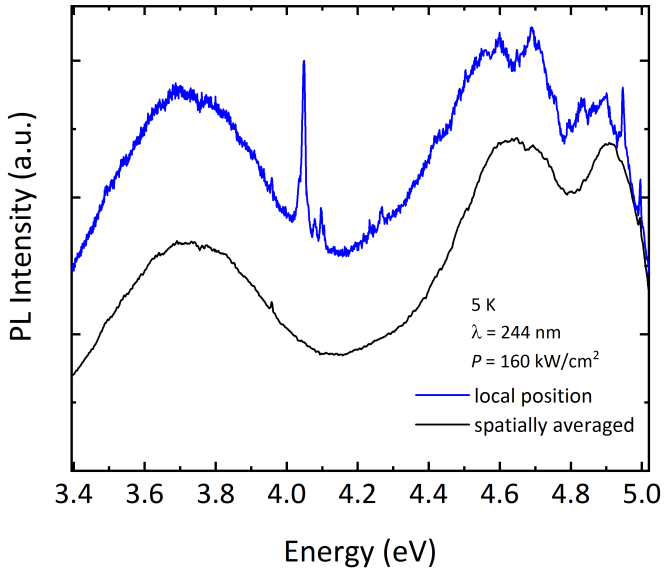

Figure 4.4 – A spatially averaged (black) and a local (blue) spectrum (vertically shifted for clarity) from a 100×100 μm^2 map. Broad peaks from the wetting layer are observed at 4.6 and 4.95 eV and a defect luminescence band from the substrate appears at 3.7 eV. The intensity of single QDs is comparable to all the other emission bands. Adapted from the supplementary material of reference [31].

on this sample. For future reference, the sample label is L1573.

The optical properties were then investigated by μ-PL, using either a 244 or 266 nm laser at a sample temperature of 5 K. A 100 × 100 μm^2 mapscan with 1 μm steps was carried out using a 244 nm laser as the excitation source. In figure 4.4, we plot the averaged spectrum over the entire mapscan (black line) and a single spectrum at a selected position (blue line). Three broad emissions can be observed on both spectra, the peak at 3.7 eV is ascribed to a defect band from the AlN substrate [163]. Indeed, the same emission band was measured for samples without any growth. The double peak structure at 4.6 and 4.95 eV corresponds to a 3 and 2 MLs thick GaN/AlN QW [164]. Such a feature is expected for the proposed growth method in chapter 3, where h_{2D-3D} was determined to be 3 MLs. The WL emission is detected over the whole investigated surface, in contrast, specific locations display sharp lines that are attributed to single GaN QDs. In particular, the selected position plotted as a blue line in figure 4.4 displays an intense sharp emission line at about 4.05 eV. The WL of each laser position in the mapscan exhibits a unique spectral fingerprint. This rich optical pattern of the WL can be understood by analyzing AFM scans of similar samples as, e.g., the AFM images from figure 3.11 in chapter 3. As seen, the WL has ML thick features such as incomplete terraces, kinks, and islands. These features provide the necessary topography for lateral confinement of excitons in the WL and thus the extensive structuring of the WL's emission spectrum.

A secondary 50 × 50 μm^2 hyperspectral map scan was recorded with the 266 nm laser

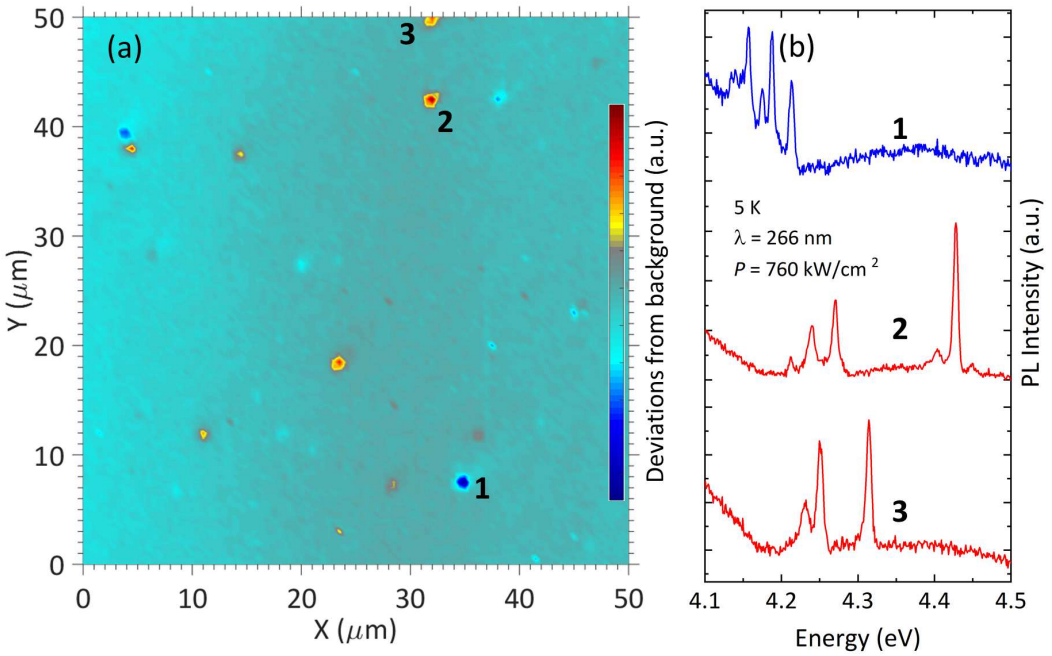

Figure 4.5 – (a) 50×50 μm^2 μ-PL map. We plot deviations from the substrate background luminescence. (b) Selected sites from the map displaying the typical QD emission (vertically shifted for clarity) found throughout the sample. Adapted from reference [31].

using a step size of 500 nm, the laser spot size was estimated at about $\simeq$ 0.5 μm in diameter. By using a 266 nm laser, the QDs are being excitated directly as the absorption from the WL is much smaller. A polychromatic μ-PL mapscan was extracted and is displayed in figure 4.5 (a). Here we plot deviations from the background luminescence within the 3.7 to 4.5 eV range. It appears that only discrete locations have QD like emission. Three of such locations are showcased with their spectrum in figure 4.5 (b). If we assume, that each of the individual emission lines corresponds to a single QD, then, a lower bound for the density of active QD emitters within the energy interval of 3.7 to 4.5 eV of 8×10^6 cm^{-2} is extracted. The sample was prepared with growth parameters that should lead to an even lower QD density than any of the uncapped samples presented in chapter 3. The growth rate was half of the lowest used for samples aimed at AFM measurements on AlN single crystal. Further on, the equivalent thickness of GaN was reduced to 3.5 MLs instead of 4 MLs. Both of these growth parameter changes are expected to yield an even lower QD density. It should be stressed that it is likely that not every QD is optically active. The presence of non-radiative centers in the dots or the statistical formation of large dots could give rise to an apparent lower QD density, as measured by μ-PL. In addition, the luminescence features related to the WL and the defect band could mask faint QD emitters.

As can be seen in from figure 4.4, there is a large background emission coming from the substrate. Such a feature makes $g^{(2)}$-measurements on single GaN QDs quite challenging.

An ideal single photon source must yield $g^{(2)}(0) = 0$. This absolute value requires the photon stream to be uncontaminated by any additional light sources at the selected energy window, i.e., any background luminescence aside from the QD transition. PL excitation spectroscopy of Alden *et al.* has demonstrated that the AlN defect luminescence at 3.7 eV has an excitation channel at 4.7 eV [163]. Furthermore, Collazo *et al.* reported an absorption coefficient ($\alpha_{4.7eV}$) in the order of 1000 cm^{-1} for the first generation of AlN substrates [165]. In contrast, the current sample employed the latest generation of AlN substrates with $\alpha_{4.7eV} < 100$ cm^{-1}. As a result, the AlN substrate luminescence at 3.7 eV intensity drops by one order of magnitude. As demonstrated in figure 4.4, the emission intensity of single QDs is comparable to the bulk defect luminescence bands of the substrate. Future substrate development aiming for lower deep luminescence is needed in order to enable more in-depth quantum-optical studies of SK GaN QD samples on AlN single crystal.

It is noticeable in the spectra that the QD linewidths are quite broad. The emission linewidths of this sample were compared to available results in the literature [36] and plotted in figure 4.6 (a). Such broadening is attributed to spectral diffusion due to a fluctuating electric field owed to defects near the QD. The defects can stochastically trap and release charges thus providing variations in the local electric field [35]. The fluctuating electric field will then shift the emission energy of the QD proportionally to the internal excitonic electric dipole. In this particular sample, an extremely low growth rate was employed to promote a low density of QDs, as a consequence the active region was exposed to the MBE environment for about 1600 s. Such a prolonged exposure of the GaN layer entails a higher probability for the incorporation of impurities, which could then act as charge trapping defects. A more extreme consequence of fluctuating electrical charges near a QD is a phenomenon known as QD blinking, which refers to the discontinuous PL emission on time scales from ms to minutes [166, 167]. QD blinking is ubiquitous in isolated colloidal QDs. In such QDs the large surface to volume ratio leads to photo-induced surface charges. Unfortunately, the large density of defects likely surrounding the QDs in our sample lead to strong blinking. Power series to identify multiexcitonic complexes were therefore useless for this sample. A plausible solution to the impurity incorporation due to the long growth times would be the use of two different growth rates: a high growth rate for the first three MLs (h_{2D-3D}), followed by a much lower one to promote a low QD density. As a result, the total exposure time of the active region to the MBE environment can be minimized while still benefiting from the positive effects of low growth rates.

In conclusion, the proposed strategy for low QD densities, relying on low GaN growth rates and AlN single crystal substrates, was confirmed to yield QD densities sufficiently low to enable the excitation of individual QDs by μ-PL. However, a strong PL background due to the AlN substrate hinders the possibility of having a clean single photon source. Nevertheless, promising advancement has been made in the growth of bulk AlN and further progress aiming at reducing undesired defect related emission might allow for a

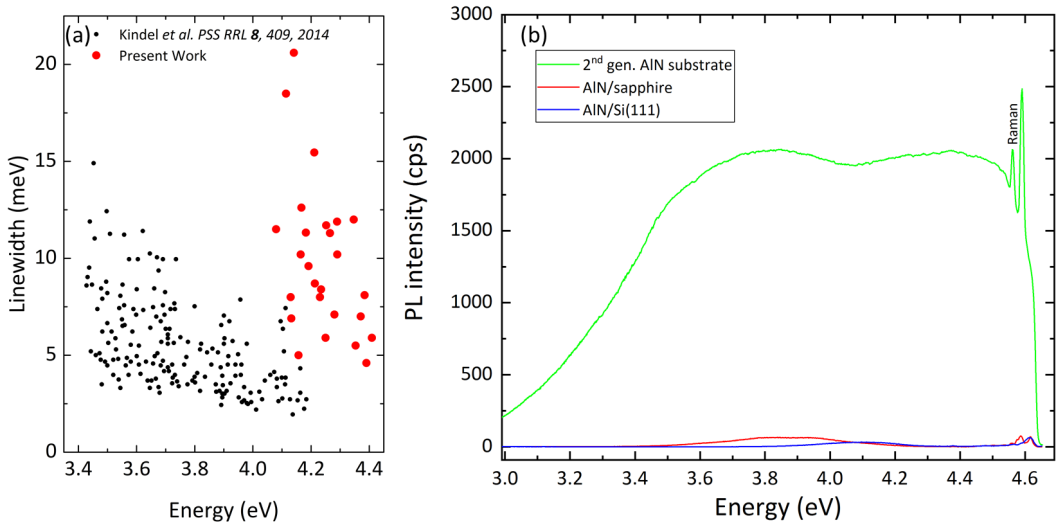

Figure 4.6 – (a) Linewidth statistics of L1573 and those found in the literature [36]. (b) Comparison of the defect related PL from the three available AlN layers excited at 266 nm.

successful implementation of GaN QDs as single photon sources with such substrates. Furthermore, the rather thick WL, inherent to SK growth further reduces the spectral window for background free QDs. Finally, the long growth times could be a disadvantage in terms of impurity incorporation as they could be the cause for the high inhomogenous broadening and QD blinking.

4.4 Single QD spectroscopy on dislocated AlN - ripening and evaporation

The defect luminescence of bare AlN substrates is compared with the other available AlN layers in figure 4.6 (b). The other available AlN layers are: 100 nm of AlN deposited by high temperature MBE on MOVPE grown AlN/sapphire templates and 100-nm-thick AlN on Si(111) developed in chapter 2. The difference in defect luminescence among the layers is striking. Furthermore, the best AlN in terms of defect luminescence is the one grown on Si(111). The intensity of the defect luminescence will depend on the density of defects and the excited volume. Because the AlN on Si(111) films are the thinnest, the number of excited defects will be minimized in these layers if we consider a similar point defect density Thus, AlN on Si(111) templates are well suited for $g^{(2)}$ measurements.

A μ-PL spectrum of a QD sample grown on AlN/sapphire utilizing ripening and evaporation (black line - L1581) is displayed in figure 4.7 along with a QD sample without ripening (red line - L1582) also grown on AlN/sapphire. The growth parameters for the sample with ripening were: $h = 4.3$ MLs, $V_{GaN} = 0.015$ ML/s, $T_S = 758$ °C and $t_r =$

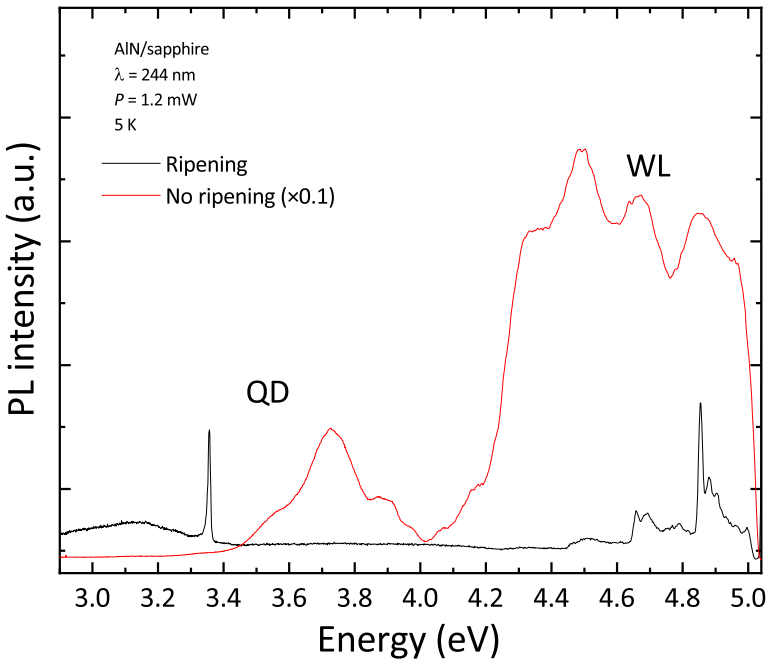

Figure 4.7 – μ-PL spectrum of a low density QD sample achieved by ripening and evaporation (black line - L1581) and a similar sample without ripening (red line - L1582). A single isolated QD can be addressed without the need for any further fabrication, the WL is highly structured when employing the ripening strategy. The spectrum without ripening was rescaled by a factor of 0.1.

320 s. The acquisition parameters are almost identical, except for the integration time. The acquisition time had to be reduced for L1582 to avoid saturation of the CCD. The spectra were normalized by acquisition time and L1582 was further rescaled by a factor 0.1. The overall brightness of the two samples is radically different. Furthermore, no sharp features are observable for L1582, whereas for L1581 a distinct single QD peak can be observed. Thus, the QD density was reduced to at least $\sim 10^8$ cm^{-2}. Finally, the WL is both dimmer and at higher energies when a ripening is employed, which confirms the hypothesis of a WL thinning during ripening.

4.5 Spectroscopy of GaN QDs on Si(111)

4.5.1 Sample description

Even if samples with extremely low QD densities can be achieved allowing individual QDs to be studied, it is also practical to perform nanofabrication in order to establish a "map" of the sample's surface. By employing electron beam lithography (EBL), the sample's area can be subdivided into a grid and hence the same location and specific QD can be addressed and recalled even after, e.g., a thermal drift when executing a series of

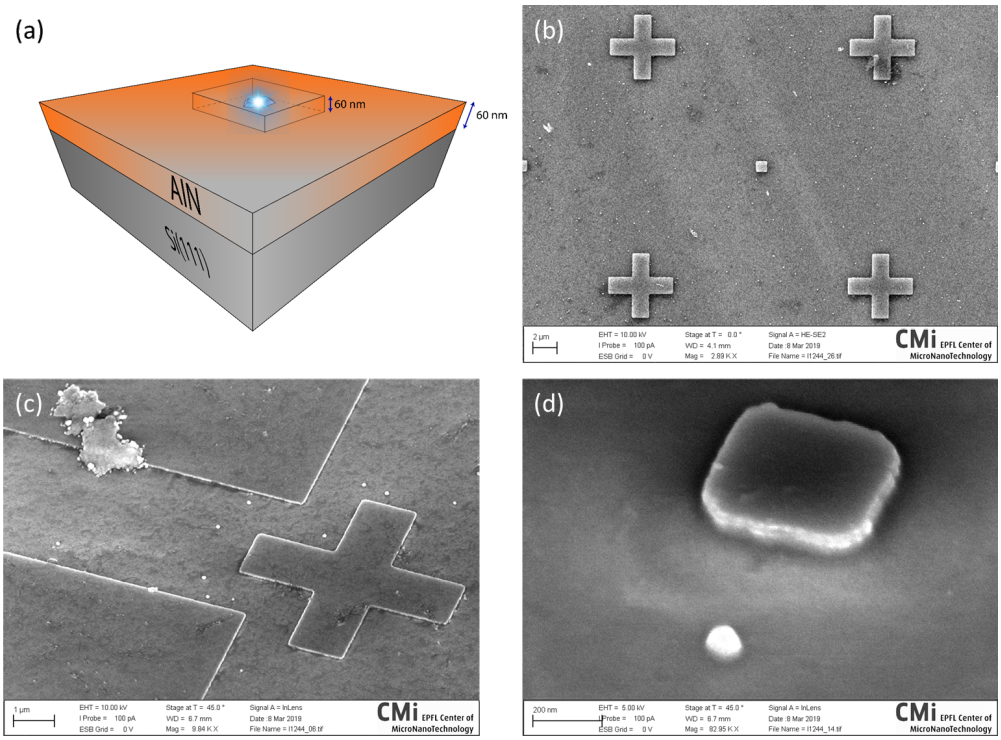

Figure 4.8 – (a) Schematic representation of the sample structure. (b) Plan view, low magnification SEM of the mesa processing and position markers. (c) and (d) Birds eye view SEM of a square mesa and a nanomesa.

temperature-dependent measurements. The sample, labeled L1244, consists of 100 nm of high temperature AlN on Si(111), followed by a plane of GaN QDs and capped with 20 nm of AlN. Finally, a secondary plane of GaN QDs was grown on top and left uncapped. The QD growth was obtained by the m-SK method. The growth conditions were: T_S = 820 °C, h = 6 MLs and t_r = 20 s[1]. The sample was then cleaved and half of it was reintroduced into the MBE chamber, then the temperature was raised to 800 °C under UHV to evaporate the surface GaN. The other half was used for AFM measurements. A small piece with the surface GaN evaporated was then processed by EBL by Dr. K. Shojiki (former LASPE postdoc)into a grid of mesas and markers. The resulting mesa structure is depicted in figure 4.8. The developed regions of the resist were etched down to a depth of about 60 nm, so that no QDs remain outside of the mesa and marker structures. Interestingly, the fabrication also yielded some smaller mesas, of about 60 nm in diameter at the top and 100 nm at the base, randomly located throughout the developed areas. These are not fabrication deposits but rather unetched nanomesas where potentially GaN QDs reside.

The sample has been characterized by optical microscopy, SEM, AFM, CL, μ-PL and

[1]A full 2 inch wafer was used, and no rotation was performed during the QD growth in order to achieve a thickness gradient. The gradient over 2 inches amounts to ± 20%.

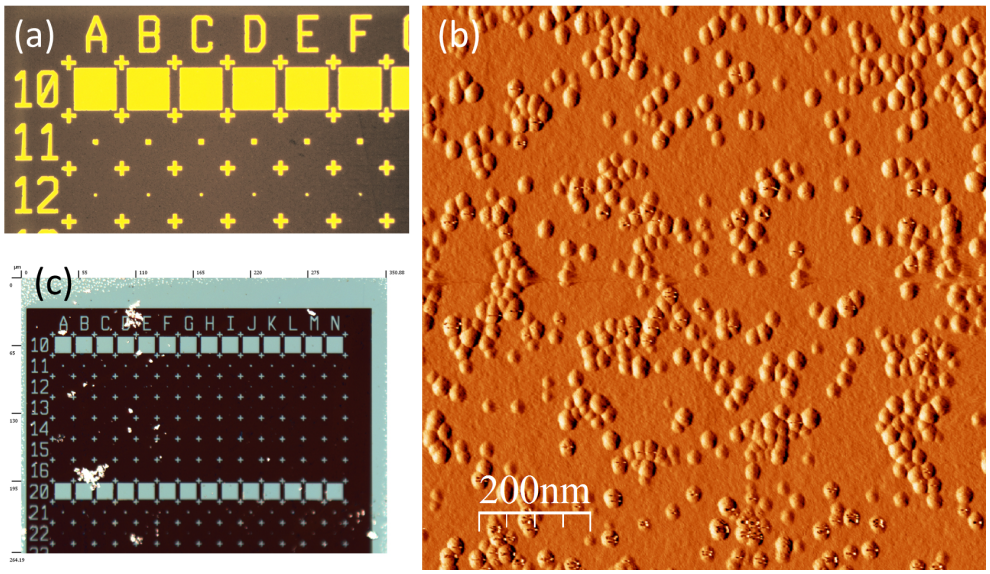

Figure 4.9 – Optical microscope photographs of the mesa fabrication at two different magnifications, (a) and (c). (b) Amplitude signal AFM of the sample's surface exhibiting clear self assembled islands.

an HBT interferometry. Optical microscopy photographs of the fabricated structure are displayed in figure 4.9, the distance between markers (crosses) is 20 μm. Mesa of different size are available, from several microns in diameter, down to 20 nm. However, the smallest ones were probably not correctly developed during the lithography process. Due to the extensive manipulation of the sample, some deposits have formed on its surface as can be seen in figure 4.9 (c). Nevertheless they do not interfere with the optical measurements. An AFM, in amplitude mode, is displayed in figure 4.9 (b) demonstrating clear GaN QDs on the surface. The size of the QDs is quite inhomogenous, which is advantageous for the study of the spectral signature of individual QD emitting at a wide range of energies.

The sample has been preliminarily investigated by CL measurements at 12 K (figure 4.10), This allows accessing emission at higher energies than those allowed by lasers. In this manner, it was possible to resolve an emission peak at 5.2 eV. This peak is ubiquitous in the sample, except for the etched portions. Also such peak could not be found on bare AlN on Si(111) samples. This high energy emssion is consistent with a GaN/AlN QW, with a thickness of 1.5 MLs [164]. We thus ascribe this transition to a thin WL induced by the ripening step.

4.5.2 μ-Photoluminescence of GaN QDs on Si(111)

The sample was mapped several times over an area of 100 $\times$ 100 μm^2 with different spectral windows at a sample temperature of 5 K with the 244 nm laser operating at

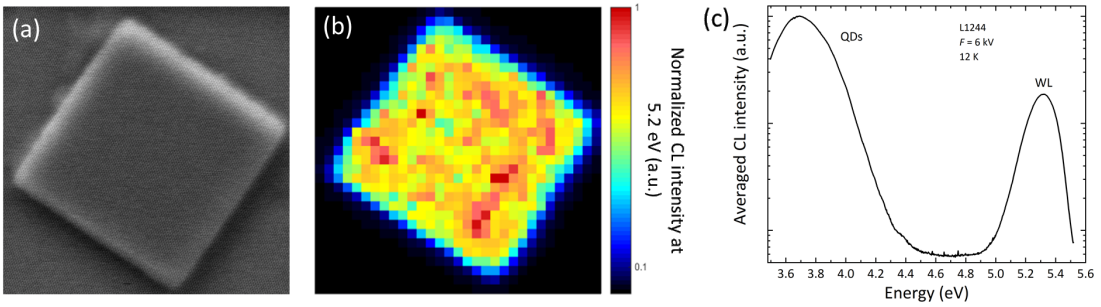

Figure 4.10 – (a) SEM image of the probed area by CL. (b) CL intensity at the energy of 5.2 eV. (c) Averaged CL spectrum. The peak at 5.2 eV corresponds to a $\sim$ 1.5 MLs thick GaN QW, i.e., the WL.

1.3 mW. From such maps, a large number of spatially separate and distinct QD spectra were obtained. By individually extracting spectra and fitting each QD line, a statistic of the QD linewidth as a function of energy was obtained. The result is plotted in figure 4.11 and once again compared with the results available in the literature [36]. The linewidths obtained in this work match convincingly those reported by Kindel *et al.* in the energy range where the measurements overlap. The use of a 244 nm laser and the occurrence of very small dots in the sample allowed us to extend the energy range up to almost 5 eV. As can be readily observed from figure 4.11, the overall trend is broad linewidths at low emission energies and sharper QD emission lines at high emission energies. The smallest linewidths were on the order of 700 μeV at an excitation power of 1 mW. Interestingly, for a given emission energy the distribution of linewidths is highly asymmetric, a sharp cut-off exists for small linewidths, while the distribution of broad peaks does not sharply cut-off. The same observation was made for GaAs/AlGaAs QDs [168].

The trend of diminishing linewidths with increasing emission energy was explained by Kindel *et al* [36]. Excitons in *c*-plane GaN/AlN QDs have an intrinsic electric dipole due to the QCSE. By definition, the electric dipole moment has a magnitude $q \cdot h$. The electric charge is fixed, but the distance h is, as a first approximation, the QD height. Hence, larger QDs emitting at lower energies will carry a larger excitonic dipole moment. The model can be further enhanced by calculating the electron and hole wavefunctions in order to obtain a spatial charge density. As a result, a more accurate determination of the excitonic dipole moment can be achieved that also considers the aspect ratio of the QD (height/diameter). The final consideration is spectral diffusion; defects near the QD can stochastically trap and release electrical charge over time scales smaller than the PL integration time. Consequently, the emission energy of the QD wavers as a result of the fluctuating electrical field. The emission energy deviation due to spectral diffusion will be greater for large QDs exhibiting large electric dipole moments.

During the analysis of the spectra of L1244 a recurring spectral trace was found. The pattern consists of four spectral lines, where the highest energy line often dominates in

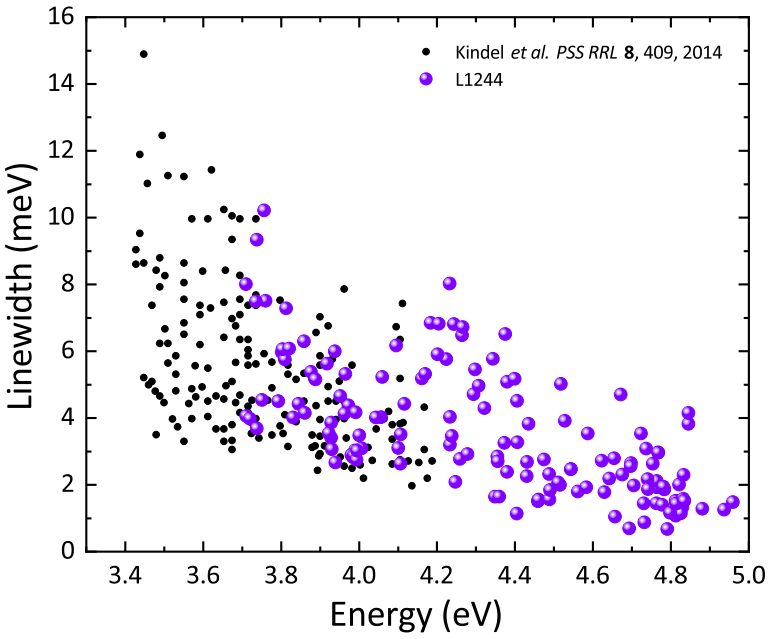

Figure 4.11 – Single QD linewidths statistics of L1244 at 5 K and those found in the literature [36].

intensity. The repetition of the same spectral signature at different energies and different sites on the sample motivated us to further study such QDs. Some of those spectra are plotted in figure 4.12 (a) along with a selected QD for which a long integration time was employed (b), labeled as QD1. For convenience, the four most prominent peaks will be labeled from low to high energy as peak 1, 2, 3 and 4.

The repetition of very similar spectral signatures at different sites of the samples suggests that each set of lines correspond to a single QD. Further proof of the hypothesis is given by spectral diffusion, which is not necessarily restricted to small time scales that broaden the linewidths, but can also be observed in time scales of seconds [153, 35]. A time series of the PL emission from QD1 is displayed in figure 4.13 (a). The energy shift of each of these peaks is then plotted as function of time in figure 4.13 (b). Upon close inspection of the spectral diffusion of each of these lines it can be concluded that they all shift at the same instant in time and with a similar amplitude. The synchronus behavior of these lines is a reaction to the same fluctuation in the local electric field. Therefore it can be concluded that all the lines in figure 4.12(b) stem from the same QD [153].

Next, we would like to address the challenge of identifying the physical nature of each of these lines. A common approach to this task is to perform an excitation power density dependent set of experiments as displayed in figure 4.14. Different excitonic complexes have various occupation probabilities as a function of excitation power. As a result, some complexes are only visible at high excitation powers and scale differently

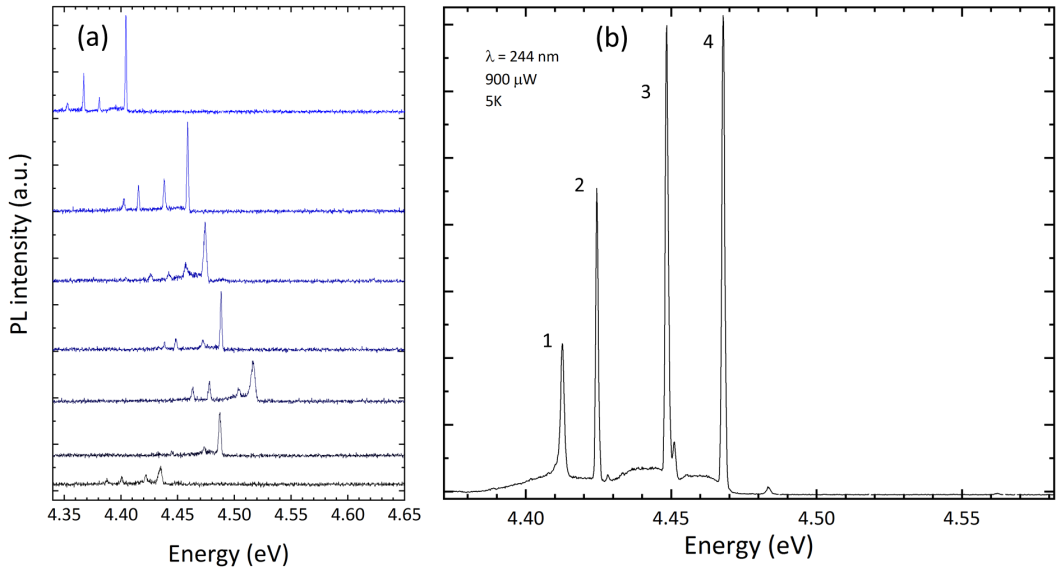

Figure 4.12 – (a) μ-PL spectra of different QDs emitting a similar PL trace. (b) Spectrum with a long integration time (120 s) of QD1.

depending on the excitation power [32]. As already pointed out, the biexciton binding energy (E^b_{XX}) can be either positive or negative [32, 151] depending on the QD size and aspect ratio. Positive and negative E^b_{XX} have been observed as well in conventional III-V semiconductor QDs [26]. It is generally accepted that whereas the exciton scales linearly with excitation power, the biexciton scales quadratically [32]. However, this is not always the case as sublinear dependencies of the exciton have been reported as well as fractional exponentials for the biexciton [151]. The common trend is that at very low power only the exciton is observed since the average carrier population is proportional to the input power and hence the probability of simultaneously populating the QD with two or more excitons is very low. As the power is increased the probability of higher order excitonic complexes increases, while simultaneously decreasing the probability of having only one exciton in the QD.

The intensity of excitons, biexcitons and higher order excitonic complexes as a function of the excitation power was quantitatively modeled by C. Kindel [169]. The transitions between states will be mediated by the absorption rate of photons or pump rate Π, and the decay rate γ_i, where the subscript i identifies the number of excitons in the QD. The luminescent intensity will be then given by $I_i = \gamma_i p_i$, where p_i is the occupation probability. The occupation probability can be rewritten in terms of pump rate and decay rate from higher order excitons:

$$I_i = \gamma_i c \prod_{j=1}^{i} \frac{\Pi}{\gamma_j} \tag{4.1}$$

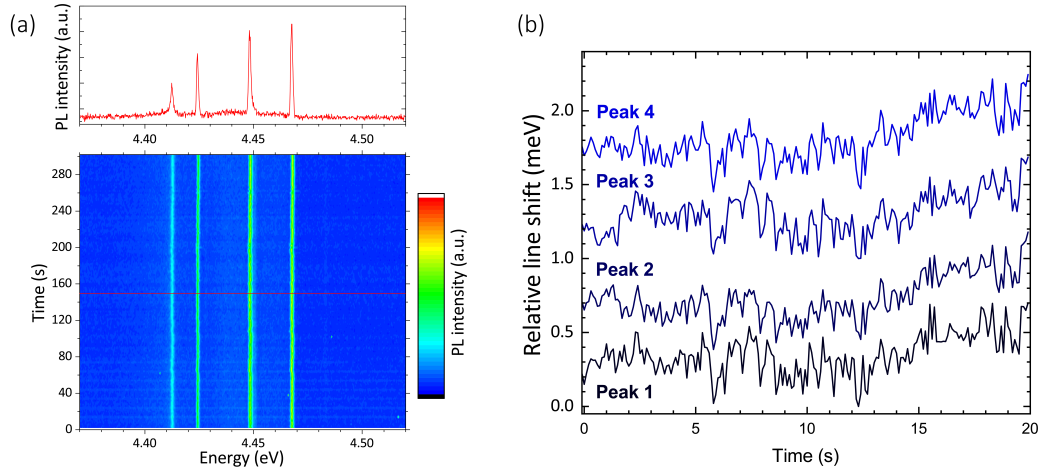

Figure 4.13 – (a) PL emission of QD1 as a function of time, small displacements in the emission energy can be observed. (b) Relative shift of each of the peaks (vertically shifted for clarity), the shifts are strongly correlated.

Here c is a renormalization factor:

$$c \equiv \left(\sum_{k=0}^{\infty} \prod_{j=1}^{k} \frac{\Pi}{\gamma_j} \right)^{-1} \tag{4.2}$$

Then, for a Poissonian distribution of p the intensity can be written in terms of the average number of excitons in the QD (μ), as:

$$I_i^{ss,\,\mathrm{pois}} = \frac{e^{-\mu}\mu^i}{(i-1)!} \tag{4.3}$$

And finally, the intensity can be written in terms of the excitation power as:

$$I_n(P) = I_0 \cdot \left(\frac{P}{P_0} \right)^n \exp\left(\frac{P}{P_0} \right) \tag{4.4}$$

where, n, I_0 and P_0 are the fitting parameters and n is different for each line. μ in equation 4.3 has been replaced by P/P_0. In the simple case of only two excitonic complexes, X and XX, n takes a value of 1 and 2 respectively.

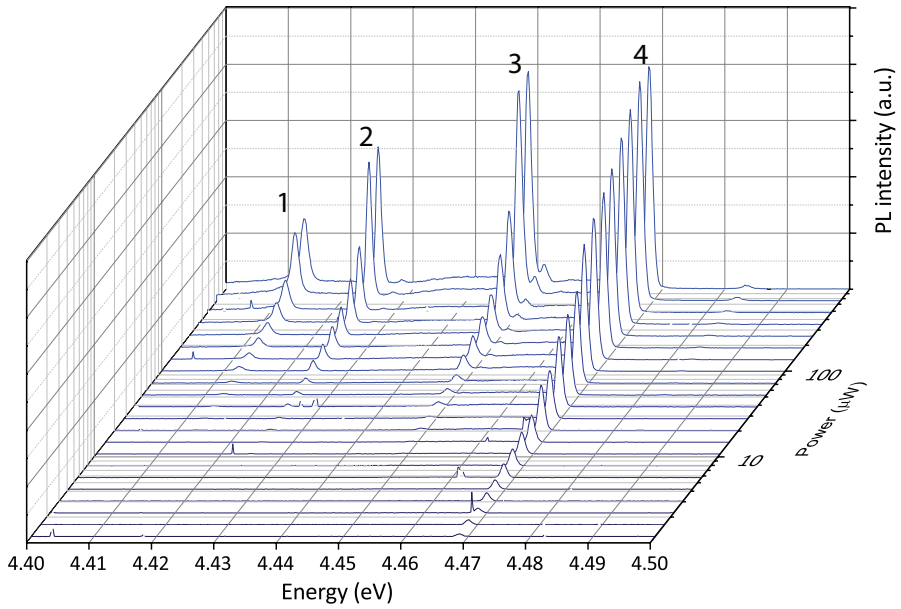

Figure 4.14 – PL spectra of QD1 as a function of excitation power. The exciton is identified as peak 4, since it is still visible at very low excitation powers.

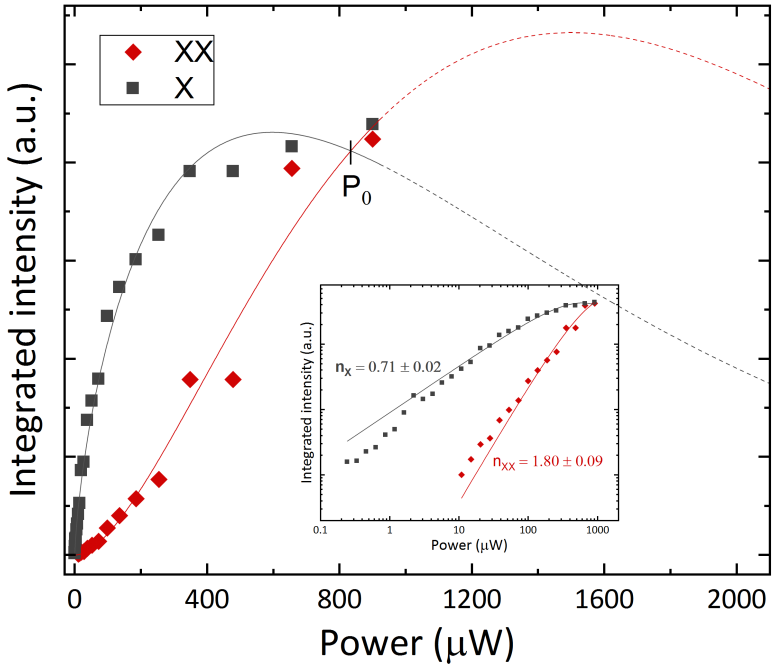

Figure 4.15 – Integrated intensity of the exciton and biexciton lines as a function of the excitation power. The lines are the result of fitting equation 4.4. The inset is the same result in a log/log plot.

From the spectrum at the lowest power, the exciton can be readily identified. It corresponds to the line at 4.467 eV, or peak 4 in figure 4.14. We have earlier shown that the inhomogeneous broadening of the spectral lines at low temperature is determined by spectral diffusion, hence, they can be fitted by a gaussian profile [170]. Finally, by fitting the integrated intensity of peak 3 and 4 to equation 4.4 (figure 4.15) we can assume that peak 3 is the biexciton. Peaks 1 and 2 remain unidentified as of the writing of this document. A plausible origin of such transition is a charged-exciton and charged-biexciton. Theoretical calculations will hopefully help us to elucidate their origin.

4.5.3 Polarization and temperature

Single photon sources should emit linearly polarized photons to enable quantum computation with linear optics [42]. Furthermore, for device integration, a single photon source operating at non-cryogenic temperatures will be better fitted for a small spatial footprint. Aside from the practical interest of such properties, the impact of temperature and polarization can help to further understand the GaN QD optical fingerprint.

Fine structure splitting

The total angular momentum of holes and electrons and the principle of angular momentum conservation set strict recombination rules for excitonic complexes. Electrons in their first excited state have a principal quantum number $n = 1$, hence their total angular momentum (j) amounts only to the spin component $s = \pm\ 1/2$. In contrast, holes have a total angular momentum $j = \pm\ 3/2$ [151]. Then, four degenerate states are produced, two of such are called *dark*, with total excitonic momentum $M = \pm\ 2$ and the other two with $M = \pm\ 1$ are called *bright*. The terms *bright* and *dark*, indicate whether the exciton can couple to one photon or not. The exchange interaction between the electron and hole mixes the *dark* states and lifts the degeneracy ($|2\rangle \pm |-2\rangle$). In a similar manner, a low confinement symmetry (elongated or asymmetric QDs) combines the *bright* states and removes the degeneracy ($|1\rangle \pm |-1\rangle$). While pure states yield circularly polarized photons, the mixed states produce linearly polarized ones [171]. As a result, the exciton's *bright* states can be separated by performing polarization dependent measurements, the energy difference between the two *bright* states is known as the fine-structure splitting (FSS). For a conventional biexciton, the ground state does not split as the total spin amounts to zero. The bright states are labeled X_1 and X_2

The hybrid biexciton

Further experiments were understood through the hybrid biexciton model proposed by Hönig *et al.* in 2014 [151]. In the conventional biexciton picture, the biexciton consists of two pairs of electron and holes occupying the lowest electron and hole orbitals, each

with paired spins. Then, the total excitonic momentum of the system will be $M = 0$. The biexciton can then decay into either of the exciton's bright states with total angular momentum $M = \pm 1$. However, for GaN QDs, the conventional biexciton is not necessarily true; the huge built in electric field will spatially separate the electrons from the holes along the *c*-axis. The carrier confinement is further differentiated by the effective mass of electrons and holes and hence the effective Bohr radius $a_* := (m_e/m_*)\,\epsilon_r a_0$. Consequently, the electrons are still strongly confined but the holes only weakly. As a result, coulombic forces and the exchange interaction become dominant for the holes. Finally, laterally separated hole states with parallel spins are energetically more favourable than those exhibiting antiparallel spins.

The radiative decay of a hybrid biexciton will be strikingly different from the conventional biexciton. In the hybrid biexciton, the two electrons have opposite spins, whereas the holes have parallel spins (see Fig. 4.16). Conservation of angular momentum will lead to an intermediate *dark*-exciton with total excitonic angular moment $M = \pm 2$, instead of the *bright* exciton with $M = \pm 1$. The process is illustrated in figure 4.16. The *dark*-exciton can then transition into a *bright* exciton through a phonon mediated spin flip. As a consequence, the bright exciton states are thermally activated by the phonon spin flip.

In figure 4.17, the cross-polarized spectra of QD1 at a sample temperature of 5K is presented. From the hybrid XX model, we would expect XX to be cross-polarized to X_1, but aligned with X_2 [151]. Indeed, we can observe a small, cross-polarized line appear at a higher energy than X_1. Further on, at the same polarization as X_1, a low intensity line appears next to XX, within the framework of the hybrid XX this line exhibits the *dark* state splitting of X. These are labeled as XX_1 and XX_2 Finally, we observe that peaks 1 and 2 share the same polarization as XX_1. A FSS of the *bright* exciton of 15 meV is deduced. The value is within the trend presented by Kindel *et al.* for the FSS in GaN/AlN QDs [152].

It is possible to further demonstrate that QD1 exhibits a hybrid XX by performing temperature dependent μ-PL measurements. Since the spin flip from the *dark* X state to a *bright* one is phonon mediated, we would expect temperature to have an important role in the intensity ratio of each transition. The μ-PL spectrum of QD1 is plotted in figure 4.18(a) as a function of the sample temperature. The excitation power was set to 1 mW. The energy and FWHM of the *bright* states and the biexciton are plotted in figure 4.18 (b). X_2 could be tracked over the whole temperature range. It redshifts by about 90 meV and broadens to 66 meV at 300 K. Interestingly, from the Varshni formula, a redshift of around 70 meV is expected for bulk GaN and 90 meV for bulk AlN (see table 1.1).

From the power series of QD1 and the corresponding analysis presented in figure 4.15, it can be concluded that at an excitation power of 1 mW, $\mu > 1$. Hence, the probability of a XX occupying the QD is larger than the probability of only having X. As a result, we

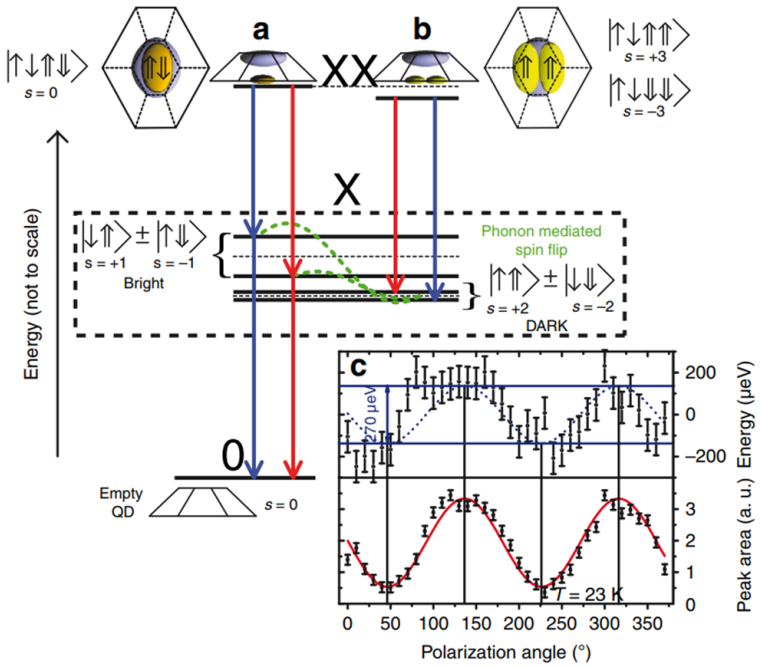

Figure 4.16 – Biexciton cascade for the conventional biexciton **a** and hybrid biexciton **b**. The hybrid biexciton decays into a dark exciton that becomes a bright exciton through a phonon mediated spin flip. Here s corresponds to the total excitonic angular momentum, whereas in the text it is written as M. Adapted from [151] with permission from Macmillan Publishers.

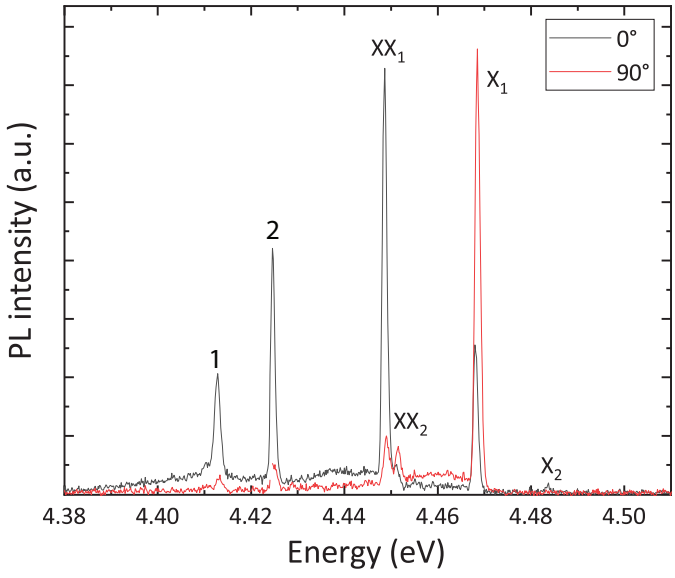

Figure 4.17 – Spectrum of QD1 at 5K for two orthogonal polarizations. Lines 1, 2, XX_1 and X_2 are cross-polarized to X_1. The low intensity line next to XX_1 corresponds to the X *dark* state splitting, and is labeled as XX_2.

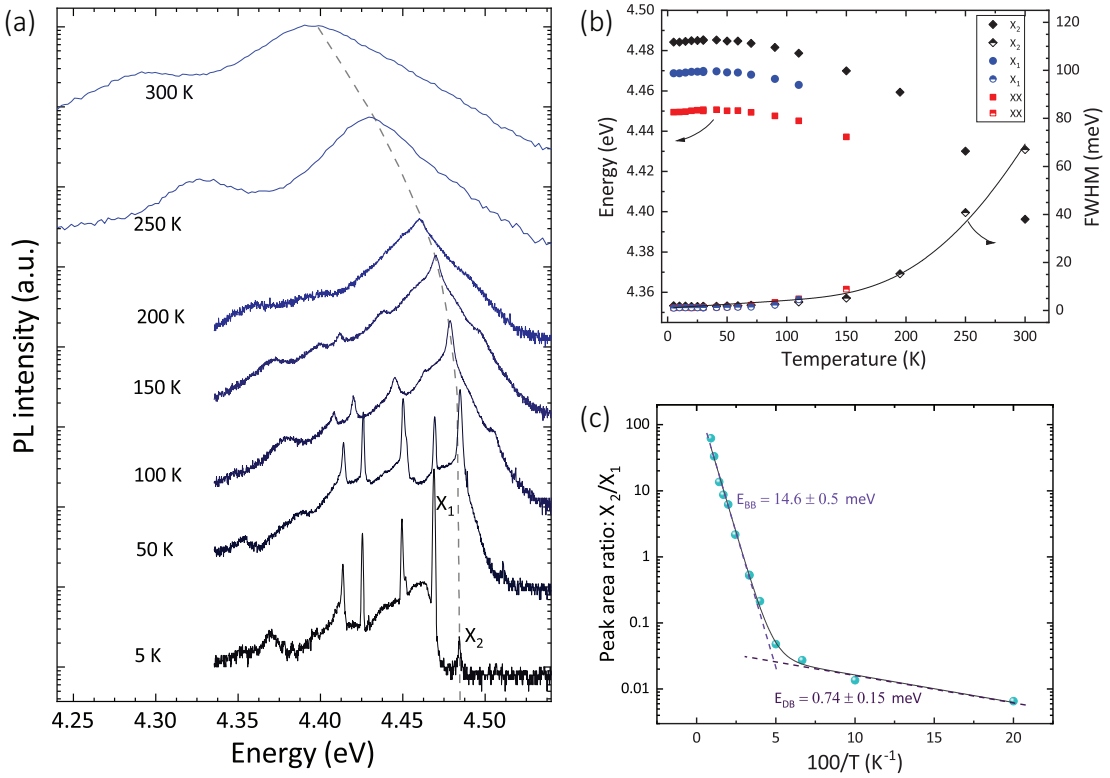

Figure 4.18 – (a) Temperature dependence of the luminescence of QD1. As the temperature is increased, the spectrum is dominated by X_2. (b) Emission and FWHM of X_1, X_2 and XX. (c) Intensity ratio X_2/X_1 and the corresponding activation energies. The activation are identified as the FSS and the *dark-bright* splitting.

expect the biexciton-exciton cascade of figure 4.16 to hold true. We can observe that as the temperature is increased, X_2 also increases in intensity and at about 40 K it matches the intensity of X_1 (not shown here). Two activation energies are obtained by the ratio: X_2/X_1. In the high temperature range, an activation energy of 14.6 meV is extracted which is ascribed to the *bright-bright* FSS. An additional activation energy is extracted at low temperature of 0.74 meV which is supposed to be the *dark-bright* splitting [151].

With the aim of studying single QDs at room temperature the same QD was tracked up to a temperature of 300 K. At 200 K, almost all lines have thermalized with the exception of X_2. Along with the increase in temperature, a clear broad line appears at 95 meV from X_2, this line corresponds to the LO-phonon of X_2 [156].

The broadening of excitonic transitions (Γ) is often modeled by the equation [172]:

$$\Gamma = \Gamma_0 + \gamma_A T + \frac{\Gamma_{\mathrm{LO}}}{\exp\left(E_{\mathrm{LO}}/k_B T\right) - 1}, \tag{4.5}$$

where Γ_0 is the linewidth at 0 K, γ_A is the coupling constant to acoustical phonons, Γ_{LO} is the coupling to longitudinal optical phonons (LO) and E_{LO} is the energy of the LO phonons. Demangeot *et al.*, modeled the broadening of GaN/AlN QDs with the linear term for temperatures up to 70 K and a value of 7.4 μeV/K was deduced for γ_A [157]. In our case, the nonlinear term was also taken into account to accurately describe the linewidth at higher temperatures. Then, from the fit of equation 4.5, and using the measured value of $E_{\mathrm{LO}} = 95$ meV, we obtain the following coupling constants: $\gamma_A = 17$ μeV/K and $\Gamma_{\mathrm{LO}} = 2.4$ eV. The result is plotted in figure 4.18(b) (black line). The value of γ_A is a factor 2 higher than the one reported by Demangeot *et al.* [157] and similar to the value for bulk GaN (13 to 16 μeV/K) [172]. Similarly, Γ_{LO} for QD1 is a factor 5 higher than bulk GaN (0.39 to 0.47 eV)[172]. An increase of the coupling strength to the LO phonon in a QD as compared to the bulk value has been reported both for GaN/AlN QDs [156] and for InAs/GaAs QDs [173].

Besides the broadening of the emission peak, the line profile itself deviates from a perfect Lorentzian with increasing temperature. As described in detail by Besombes *et al.* [174], the exciton-phonon interaction does not have a single dephasing rate, instead a more accurate description can be obtained by employing a mixed excited state (the exciton), which combines the phononic and excitonic modes. Such a behaviour is expected for any strongly confined system and QD1 is not an exception [174]. Indeed, additional phononic side bands were necessary to convincingly deconvolute the spectra during the fitting procedure.

It is difficult to directly compare intensities throughout the complete temperature series due to the huge spatial drift of the sample resulting from the thermal expansion of the sample piezostage. Nevertheless, perhaps the most important result from the temperature series is that the QD retains a bright emission such that further experiments, such as $g^{(2)}$, can be performed even at 300 K.

4.6 Room temperature excitons in GaN QDs

Linewidth statistics at 300 K are presented in figure 4.19. A clear trend cannot be extracted as in the low temperature case. Further input is being actively collected as of the writing of this document, hopefully a more complete data set could be presented in the future. The mean value amounts to 60 meV with a standard deviation of 10 meV.

As was discussed in the previous sections, a limiting feature during single GaN QD spectroscopy, and more importantly SPE, is a pronounced background emission. This problem has been successfully solved in L1244, as demonstrated in figure 4.20. Two sources of background luminescence had been previously identified: AlN defects from the underlying AlN substrate/template and the WL. Thanks to the use of thin, highly optimized AlN layers on Si(111) almost no defect luminescence is present in L1244.

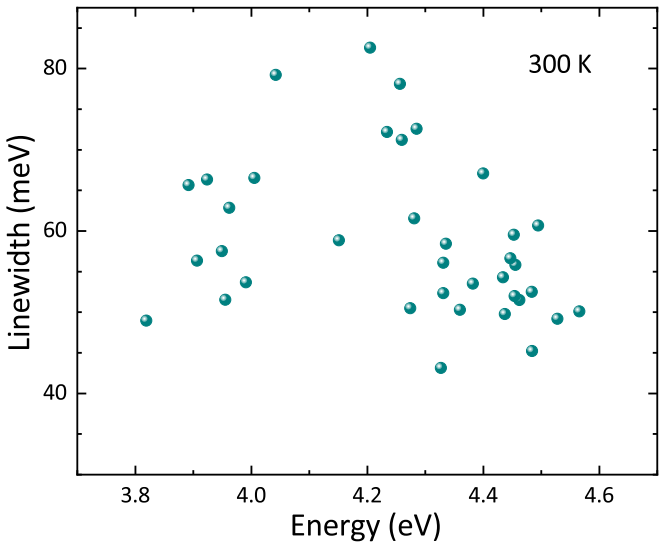

Figure 4.19 – Linewidth statistics of GaN QDs at 300 K.

Furthermore, the WL is extremely thin and is not excited with by the lasers. An overview spectrum of QD1 is presented in figure 4.20. Notice that the baseline above the laser's emission energy is at the same intensity as the rest of the spectrum's baseline. Such a nearly background free spectrum is highly desirable to achieve an "uncontaminated" photon stream at the selected spectral window and hence approach an ideal source of single photons, i.e., $g^{(2)}(0) = 0$.

The presence of non-radiative defects in the vicinity of a given QD can lead to a lower IQE compared to the ensemble. Further on, it is conceivable that non-radiative effects are different for each QD depending on its local environment; bright dots at 5 K could be dim at 300 K, while the opposite could hold true for QDs having a hybrid XX and an absences of non-radiative defects. It just happens, that QD1 is dwarfed in brightness at 300 K in comparison to other QDs with a similar emission energy. For this reason, together with the strategic importance of count rates during actual $g^{(2)}$ experiments, different QDs were studied at 300 K.

In figure 4.21, the PL spectrum as a function of excitation power of a new QD, labeled QD2 is displayed. Given the similar emission energy to QD1, it will be assumed to also follow a hybrid biexciton. At very low power, only the X line should be visible. Together with the X, a faint shoulder, 95 meV lower can also be observed. It corresponds to the LO phonon replica. As the power is increased an additional peak appears, 60 meV lower in energy than X. E^b_{XX} in the order of 60 meV are still within the trend for small GaN QDs [26]. Further analysis, similar to the one presented in figure 4.15, of the PL intensity as a function of excitation power suggests that this line could be XX. Finally, at the highest pump power, a small shoulder between X and XX appears. This line is tentatively ascribed to the FSS of X. Unfortunately, polarization-dependent measurements were

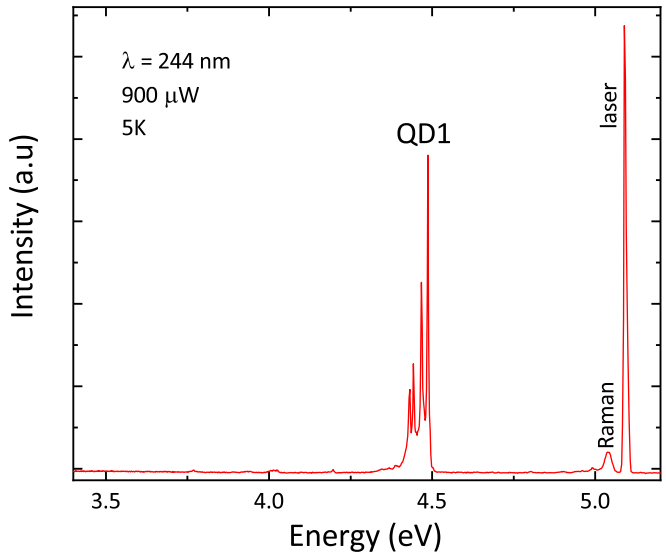

Figure 4.20 – Overview spectrum of QD1 at low temperature highlighting the low background.

carried out at a low excitation power and therefore the line assigned to X_1 cannot be resolved. However, as expected, X_2 and XX share the same linear polarization.

4.6.1 Photon statistics - single photon emission at 300 K

For a single QD, the atom like electronic structure should give rise to nonclassical light emission, i.e., photon antibunching. For simplicity, let us first consider only the transition from the first excited stated state to the ground state (X). After a photon has been emitted, the QD is necessarily in a non-radiative state, and a certain time will be needed for the QD to recover a radiative state depending on the pump rate and decay rate. As a consequence a *dead time* is expected between the emission of successive photons. The effect will not be visible if a multitude of QDs are probed or if the emission originates from a structure capable of emitting several degenerate excitons, e.g., a QW or a bulk crystal. The *dead time* and hence the QD nature of the emitter, can be evidenced by measuring the second order intensity autocorrelation function ($g^{(2)}(\tau)$). $g^{(2)}(\tau)$ measurement can also provide the fundamental recombination and excitation time of the QD [175]. For a 2 level system, and using the same notation as in section 4.5.2, $g^{(2)}(\tau)$ will be given by [169]:

$$g^{(2)}(\tau) = 1 - e^{-(\gamma_i + \Pi)|\tau|}, \tag{4.6}$$

where τ is the delay time between photon arrivals. Equation 4.6 yields 1 at long enough

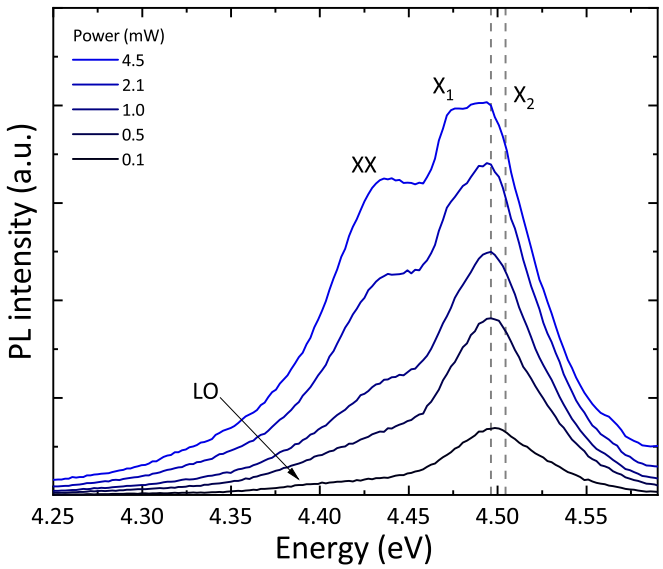

Figure 4.21 – Emission spectra of QD2 as a function of excitation power. The FSS components of the exciton (X_1 and X_2) are labeled as well as the XX and the LO phonon replica. The dashed lines delimit the spectral window used for the $g^{(2)}$ measurements.

delay time τ and a symmetric exponential decay centered around zero. The width of the downward peak is proportional to $1/(\gamma_i + \Pi)$. The recombination rate in GaN QDs depends strongly on the QD size due to the QCSE and can range from 1 μs to 400 ps for an emission energy from 2.5 eV to 4.5 eV, respectively [176]. The most important figure of merit in $g^{(2)}$ experiments is the value of the function at $\tau = 0$. This value is determined by the nature of the light source itself, for classical light $g^{(2)}(0) \geq 1$. In contrast $g^{(2)}(0) < 1$ is already an indication of non-classical light and $g^{(2)}(0) < 0.5$ is the signature of SPE [177].

Employing the 266 nm laser, $g^{(2)}$ measurements were performed on QD2 at a sample temperature of 300 K. Since the emission is quite broad ($\sim$ 60 meV), the slits of the monochromator were set to their maximum value to maximize the incoupled light reaching the detectors. At this energy, the band pass set by the monochromator and the slits amounts to about 8 meV. The spectral window for the $g^{(2)}$ measurements is plotted in figure 4.21 as dashed lines. The experiments were repeated for several excitation powers and the integration time was scaled to ensure a similar signal to noise ratio. The longest measurement, corresponding to an excitation power of 100 μW, ran for about 20 hours. A subroutine in the μ-PL's computer program performs an automatic mapping of the area around the QD after a given time, so that spatial drifts over time can be corrected.

The $g^{(2)}$ measurements are plotted in figure 4.22, the data was binned to 100 ps/channel or 400 ps/channel. A clear antibunching peak, signature of SPE, can be observed. The best value was obtained at the lowest excitation power, for which $g^{(2)}(0) = 0.17$. Additionally, three effects can be observed: a narrowing of the antibunching peak with

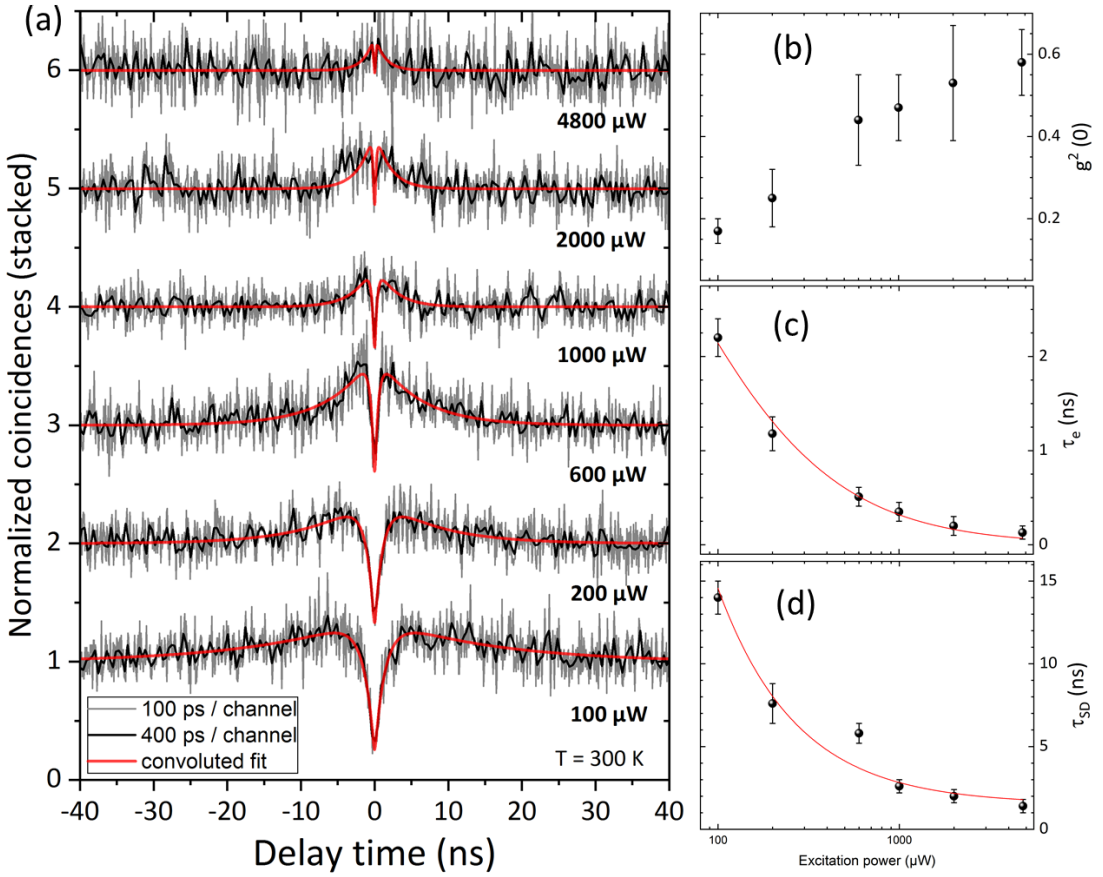

Figure 4.22 – (a) $g^{(2)}$ of QD2 as a function of excitation power at a temperature of 300 K. (b) Deconvoluted $g^{(2)}(0)$ values, (c) antibunching time constant and (d) spectral diffusion time.

rising excitation power, a superposition of photon bunching to the antibunching that narrows with increasing pump power and finally a degradation of the figure of merit $g^{(2)}(0)$, from 0.17 at 100 μW to 0.58 at 4800 μW.

Let us now address the narrowing of the antibunching peak. From equation 4.6, it can be seen that the width of the peak depends on $\frac{1}{\gamma_i+\Pi}$. As the excitation power is increased, Π should also increase. The antibunching time constant ($\tau_e = \gamma_i + \Pi$), plotted in figure 4.22(c), can be well fitted by considering $\Pi \propto$ power. Surprisingly, a spontaneous emission time at the low power limit $\tau_r = 1/\gamma_i$ of 5.8 ($\pm$ 1.6) ns is obtained. This value is one order of magnitude longer than the radiative decay time measured for a GaN QD emitting at 4.5 eV by Kako *et al.* [176]. Two possible explanations are presented:

1. The measurements of Kako *et al.* relied on a pulsed laser operating at 210 nm, and an ensemble of QDs is excited. Since the laser is pulsed, high excitation powers are likely and multiexcitonic complexes are also probed, which have faster decay times

[178]. Further on, a high excitation power can screen the electric field and hence increase the wavefunctions' overlap.

2. A difference between the lifetime of the single exciton transition in the limit of a vanishing pump rate for an InAs/GaAs QD in a bulk crystal as compared to an InAs/GaAs QD in a micro disc has been reported by Becher *et al.* [175]. For the QD in a bulk crystal a time constant of 900 ps was found, whereas the QD in the micro disc was 6 ns. The author's attributed this change to the different photonic environment. However, a comprehensive explanation is not presented. In our case, the mesa structuring could provide a similar change in photonic environment as compared to an unprocessed sample.

An additional bunching can be readily seen on all the spectra presented in figure 4.22, the width of the bunching decreases with increasing pump power. Such a feature was successfully explained by Sallen *et al.* [179]. A QD displaying a larger broadening than the spectral window for the $g^{(2)}$ experiment due to spectral diffusion will emit photons within the spectral window for a limited time. The trapping of charges near the QD will spectrally shift the QD emission in and out of the detection, this will lead to photon bunching with a characteristic time τ_{SD}. In the current data, we observe that the trapping rate of the charges is determined by the excitation power. According to Holmes *et al.* [154], the rate of spectral diffusion as a function of the excitation power can be modeled as:

$$\tau_{SD} \propto \frac{1}{\sqrt{P}}. \tag{4.7}$$

Then, as the power is increased, all the charge traps will be unoccupied and the spectral diffusion rate becomes very fast. On the other hand, when the excitation power is reduced most charges will be occupied and so the rate at which the QD is spectrally shifted is very slow. Here a constant had to be added to equation 4.7 to obtain a convincing fit. The added constant, SD_0, is then the high power limit for the spectral diffusion rate. Physically, SD_0 is tentatively explained as follows: in the high power limit we could consider that the pump power is so huge that any occupied trap will be almost immediately ionized, then SD_0 is the decay time of the uncharged state.

Finally, let us address the increase in the value of $g^{(2)}(0)$ with the excitation power. As the power is increased, the pump rate (Π) in equation 4.6 grows and the width of the antibunching peak decreases. It eventually becomes extremely sharp. The recorded measurement will be a convolution of the instrument response function (IRF) and the actual optical properties. After constructing the HBT setup, Dr. I. Rousseau (former LAPSE PhD student) measured the IRF of the system and concluded a time resolution

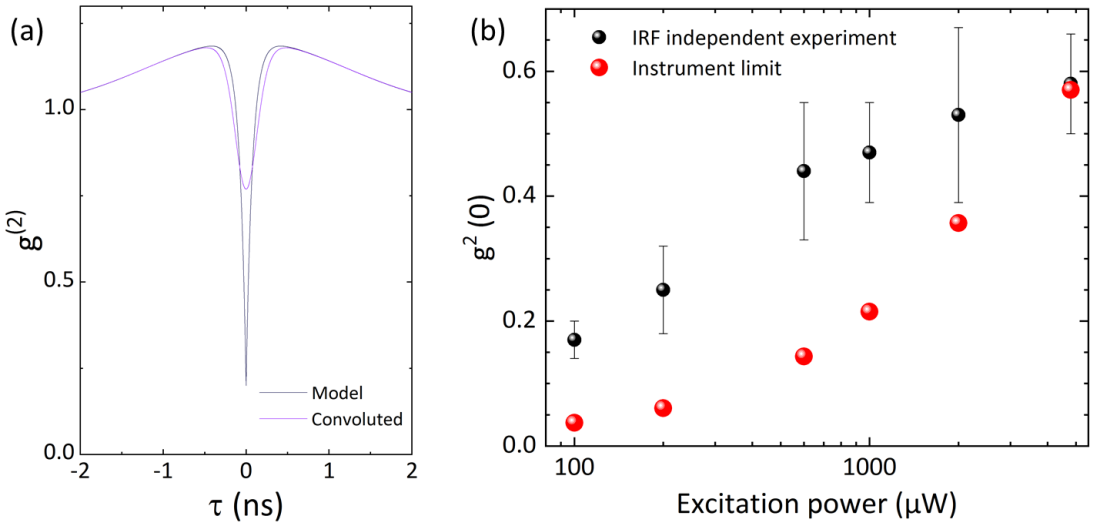

Figure 4.23 – (a) Modeled $g^{(2)}$ function with equation 4.8 and the same function convoluted with the IRF. For very high pump rates, the instrument is not capable of resolving the antibunching peak. (b) Instrument limit of $g^{(2)}(0)$ as a function of the excitation power and the deconvoluted instrument independent experimental values.

of about 250 ps [180]. Similarly, Dr. G. Callsen (Postdoc at LASPE) measured a time resolution of 220 ps for an HBT setup with identical detectors in TU-Berlin. If the width of the antibunching peak approaches the system's time resolution an increase in the $g^{(2)}(0)$ value in the raw data is expected. In order to assess the impact of the IRF on the $g^{(2)}(0)$, the values obtained in figure 4.22 (c) and (d) were used to reconstruct a modeled $g^{(2)}$ function independent of the instrument:

$$g^{(2)}(\tau) = 1 - e^{-(1/\tau_r + \alpha P)|\tau|} + A_{SD} e^{-\tau^2/2\tau_{SD}^2}, \tag{4.8}$$

where Π has been replaced by the excitation power P times a coupling constant α that was determined from the fit of τ_e, see figure 4.22 (c). A_{SD} is the amplitude of the bunching and τ_{SD} is the spectral diffusion rate. For the IRF a simple gaussian with a FWHM of 250 ps was considered. Then, the two functions were convoluted and the new theoretical $g^{(2)}(0)$ value extracted using a simple code written with *Mathematica* software (figure 4.23 (a)). To assess the degradation of the raw $g^{(2)}(0)$ value only due to the narrowing of the antibunching peak and the IRF, A_{SD} was set to zero. In figure 4.23 (b) we plot the theoretical limit for the raw values of $g^{(2)}(0)$ due to the detector resolution. It should be noted that the detector time resolution can be circumvented to obtain $g^{(2)}(0)$ independent of detector resolution. This is done by fitting the data with the convolution of $g^{(2)}(\tau)$ and the IRF. Once the fit has converged, the IRF is set to an arbitrarily small value and the $g^{(2)}(\tau)$ is simulated to obtain an instrument independent

$g^{(2)}(0)$. The reported values of $g^{(2)}(0)$ in figure 4.22 are instrument independent. As a consequence, an additional element is clearly limiting the minimization of $g^{(2)}(0)$. This is either the amplitude of the bunching peak due to spectral diffusion or an increased background from other excitonic complexes in the QD. From the PL spectrum of the QD (figure 4.21) we can observe that XX overlaps with the X_2 line at high powers. This will lead to a decrease in the single photon purity [47].

High purity single photon emission

The value of $g^{(2)}(0)$ is judged to be the most important figure of merit for a single photon source. Then, following the previous analysis the successful minimization of the raw data values will require to experimentally achieve $A_{SD} = 0$. In principle $A_{SD} = 0$ can be achieved by integrating over the entire range of energy of the optical transition [179]. However, given the limitations of our setup, this can only be achieved at low temperature where the linewidth of the optical transition is smaller than the spectral window set by the monochromator and the slits. Further on, the pump power should be minimized in order to keep a wide antibunching peak such that the raw value of $g^{(2)}(0)$ is not limited by the IRF. In figure 4.24 we display the $g^{(2)}(\tau)$ of a new QD (QD3) under 100 μW[2] of excitation power at a temperature of 5 K. The experiment had very low count rates; in the order of 600-1000 counts s^{-1}. For this reason, the total integration time exceeded 75 hours. The figure of merit was: $g^{(2)}(0) = 0.09 \pm 0.03$. This value is comparable to the state of the art in III-nitride which is 0.08 [161]. It should be noted that the structure employed by Arita *et al.* consists of a GaN QW with AlGaN barriers. At specific locations the sample exhibits interface fluctuation that provide the necessary lateral confinement for a QD-like optical trace. Due to the nature of the structure itself, the SPE is not expected to be robust with increasing temperature.

4.6.2 Absolute count rate

III-nitride QDs are often considered to be dim in comparison to their arsenide counterpart. In 2016, Aharanovich *et al.* published a review titled "Solid-state single-photon emitters" [44]. In this review they quote the maximum count rate for a variety of systems such as diamond color centers, arsenide QDs, etc. Although nitride QDs are considered in the review, no absolute count rate is provided. The correct way of comparing maximum count rates is by estimating the number of counts at the microscope objective. The only system in the review for which maximum count rates at the microscope objective is given is for arsenide QDs: 1×10^7 counts s^{-1}. In contrast, our $g^{(2)}$ experiments were performed with $\sim 10^3$ counts s^{-1}.

The HBT setup's efficiency was measured by following the 244 nm laser and measuring

[2]The laser power decreased over the duration of the experiment and reached 35 μW at the end.

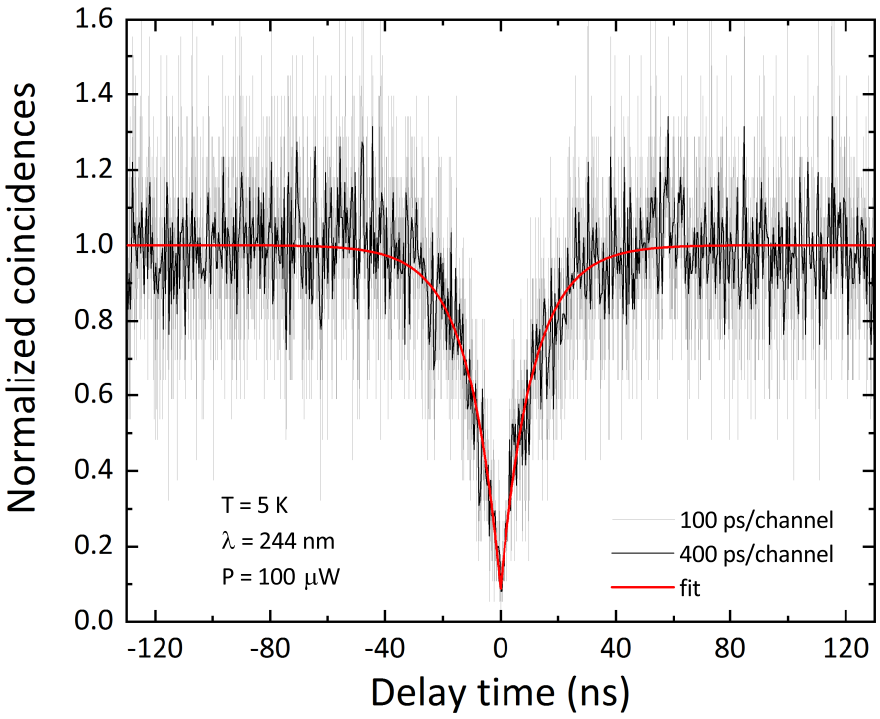

Figure 4.24 – $g^{(2)}(\tau)$ of QD3 at a temperature of 5K and low excitation power.

the power before and after each optical element. Finally, the detector's efficiency was estimated by comparing the power meter's reading to the detected counts. Table 4.1, summarizes the transmittance or efficiency of each optical element in the setup.

A photon emitted by a QD does not have to traverse all of the listed elements, those not intervening are: beam sampler - reflection, mirror - towards CCD, SPEX - 600 l/mm grating and one HBT beam splitter arm. Nevertheless, some optical elements are notorious for their low efficiency: the cryostat window, the microscope objective, the SPEX monochromator and most importantly the PMTs. For the microscope objective and the detectors, a value for the transmittance or efficiency could be estimated for a QD emitting at 275 nm (4.5 eV) by comparing our data at 244 nm to the manufacturer's transmittance curve. Then a setup efficiency of 8×10^{-5} and 1×10^{-3} is deduced for a photon at 244 nm and 275 nm, respectively.

Then for a QD emitting at 4.5 eV and an average of 3000 counts s^{-1} at each of the interferometer's arms[3] and dividing by the setup's efficiency, we can deduce an actual count rate of: $5.5 \times 10^6 \pm 3 \times 10^6$. This result, close to traditional III-V QDs, is very encouraging given that the sample is grown on a silicon substrate and held at a temperature of 300 K during the measurements.

[3]Here we considered the commonly found intensity, however count rates up to 10000 have been observed even at a sample temperature of 300 K.

Table 4.1 – Transmittance or efficiency of the optical elements of the μ-PL setup at a wavelength of 244 nm or otherwise noted.

Optical element	Transmittance or efficiency	±
Cryostat window	0.48	0.01
Mitutoyo 80× objective	0.43	0.01
Mitutoyo 80× objective at 275 nm	0.54	N/A
Mirror - into objective	0.87	0.01
Beam sampler - transmission	0.80	0.01
Beam sampler - reflection	0.13	0.01
Mirror - towards CCD	0.91	0.01
Mirror - towards HBT	0.95	0.02
Mirror - beam lowering to HBT	0.95	0.02
Mirror - beam leveling to HBT	0.95	0.01
Lens - into SPEX monochromator	0.93	0.01
SPEX - slits incoupling	0.93	0.01
SPEX - 2400 l/mm grating	0.16	0.03
SPEX - 600 l/mm grating	0.11	0.03
SPEX - slits outcoupling	0.82	0.18
Lens to HBT	0.90	0.02
HBT beam splitter - transmission	0.45	0.12
HBT beam splitter - reflection	0.58	0.08
PMT	0.009	0.003
PMT at 275 nm	0.09	N/A

5 Conclusions and outlook

In this thesis, the necessary steps to study excitons in single GaN QDs have been explored at room temperature. SPE at room temperature has been verified by the second-order autocorrelation function ($g^{(2)}$). The thesis investigates the basics of AlN growth at high temperature and demonstrates high quality AlN on Si(111). Then the focus is shifted to the epitaxy of GaN QDs. A new growth method for GaN QDs by NH_3-MBE is presented, which corresponds to true SK growth. This enabled control of the QD density over three orders of magnitude when growing on AlN single crystal substrates by changing the growth rate. A density as low as 10^8 cm^{-2} has been achieved. An additional strategy that does not require AlN single crystal substrates for the control of the QD density is also presented. Finally, the optical features of GaN QDs are proved by PL. Linewidth statistics of single QDs at 5 and 300 K, as well as temperature and power series, and $g^{(2)}$ measurements have been carried out.

The thesis begins by describing the optimization of the matrix material, i. e., AlN. The optimization of the epitaxy is performed on the most technologically relevant substrate: Si. However, the growth of III-nitrides on Si substrates is perhaps among the most challenging due to the large lattice mismatch of 19% and the extreme difference in thermal expansion coefficients. Nevertheless, high quality AlN on Si(111) is achieved with a RMS roughnesses as low as 0.3 nm over an area of 30 $\times$ 30 μm^2 by employing a cleaning procedure of the Si substrate that yields extremely flat and order surfaces together with a high substrate temperature at the frontier between step flow and layer by layer growth. The V/III ratio also plays an important role in achieving high quality layers. Small ratios lead to inversion domains and an overall low structural quality. AlN on Si(111) layers were found to be the best suited. They minimize the background emission which is detrimental for $g^{(2)}$ measurements.

Since the demonstration of GaN QDs by NH_3-MBE in the late 1990's only one growth technique has been employed to obtain GaN QD by NH_3-MBE: the modified SK growth[1]. In chapter 3, a new strategy is discussed that corresponds to true SK growth. The

SK growth is achieved by approaching T_S to the limit of GaN evaporation to enhance the diffusion length while minimizing the NH_3 pressure impinging on the surface. The phase transition from a 2D to 3D surface appears spontaneously and a critical thickness of 3 MLs is deduced. A phase diagram for the morphology of the sample is given in terms of substrate temperature and NH_3 pressure. The size and density of the QDs is demonstrated to be controllable by changing the amount of deposited GaN and the diffusion length. However, this control is limited by the presence of inhomogenous strain potential fields. Therefore, AlN layers with structural defects such as dislocations lead to a pinning of the QD density and to higher inhomogeneity of the QD sizes. Hence, by employing AlN single crystal substrates, the QD density was varied over three orders of magnitude by changing the growth rate. Alternatively, the QD density can also be reduced below the dislocation density by performing an annealing at higher temperatures. As a side effect of the annealing, the wetting layer is thinned, which is highly desirable for increasing the purity of SPE from the QDs.

The control of the QD size and density is further demonstrated by PL measurements. QDs of different sizes with luminescence energy ranging from 3.6 eV or 4.45 eV have been synthesized. Growth conditions were taken to achieve an extremely low QD density. A density of active QD emitters of 8×10^6 cm^{-2} is deduced within the energy interval of 3.7 to 4.5 eV. However, the sample suffered of high background luminescence from the substrate as well as broad QD linewidths. A second sample, consisting of GaN QDs on an AlN on Si(111) sample, was studied in depth. The linewidths were comparable to those found in the literature. Furthermore the QDs are bright even when increasing the temperature to 300 K. Multiexcitonic complexes were found in this sample, some of which could be identified with the hybrid biexciton model [151]. Then, SPE from a GaN QD at room temperature is demonstrated by performing $g^{(2)}$ measurements. The trend for the $g^{(2)}$ histogram as a function of power were described in terms of spectral diffusion and rate equations. A $g^{(2)}(0)$ of 0.09 $\pm$0.03 was obtained for a sample temperature of 5 K. Finally, the absolute brightness of the QDs was estimated to be $5.5 \times 10^6 \pm 3 \times 10^6$, close to values reported for arsenide QDs.

Outlook

Some interesting experiments on GaN single QDs can be foreseen: magneto-μ-PL, cross-correlation measurements on the various emission lines, and photon indistinguishability analysis. The two first experiments could help us to further understand the nature of the optical transitions in GaN QDs. On the other hand, GaN QDs are promising for photon indistinguishability, which is a key requirement for quantum information processing [44].

The present research paves the way towards a more sophisticated use of GaN QDs as single photon sources. Electrical injection could be attempted, although efficient p-type doping of AlN is notoriously difficult due to possible formation of nitrogen vacancies,

limited dopant solubility, and deep acceptor energy levels[181]. However it has been demonstrated to be feasible[182]. Then, a micro LED consisting of a single QD could emit single photons at room temperature under electrical injection. Another interesting avenue would be to place a single GaN QD in an optical cavity. Two types of cavities are commonly found: either a vertical cavity defined by distributed Bragg reflector or a planar cavity composed of a PhC. The vertical cavity would be challenging due to strain management and optical absorption in the Bragg reflectors. A planar PhC cavity is more realistic. For instance, promising QDs could be identified by μ-PL and an AlN regrowth could be employed to planarize the layer. Then, with the energy and position of the targeted QD known, a PhC cavity could be fabricated employing the high etching selectivity of Si(111) and III-nitrides.

A Appendix: Site Controlled Quantum Dots

Self assembled QDs, particularly SK-QDs, are considered superior in terms of quantum efficiency, to counterparts such as ML fluctuations and droplet epitaxy QDs [183]. Nevertheless, SK-QDs nucleate at random positions on the sample, which is inconvenient for further integration into photonic nanostructures. Therefore, a deterministic approach for controlling their nucleation site could prove helpful for device applications. Several approaches have been explored, among them: stressors[184], prepatterning of the substrate[185, 186] and selective area epitaxy[159, 187]. Here, we have chosen to follow the approach of prepatterning the substrate by electron beam litography, in order to create site controlled GaN/AlN QDs (SC-QD).

These results are presented as an appendix since this work was conducted by Dr. K. Shojiki. The progress discussed in this chapter was enabled by the constant assessment of the results in terms of growth and fabrication. The structural and optical characterization was mainly carried out by Dr. K. Shojiki.

The sample structure consisted in the growth of 75 nm of high temperature AlN on Si(111) by NH_3-MBE. Then, EBL was performed and shallow holes were etched into the AlN. Finally, a regrowth of a GaN QW was performed by NH_3-MBE. A transmission electron microscope image of an optimized sample is presented in figure A.1.

The successful fabrication of the nanostructure presented in figure A.1 was possible through several optimizations both in EBL fabrication and in MBE growth. Some of the challenges encountered in the process were: wafer bowing, cracks, surface contamination, etching depth control and QW thickness fluctuations.

The substrate preparation procedure presented in chapter 2 entails extremely high temperatures. Depending on the homogeneity of the thermal contact between the substrate and the Mo substrate holder, thermal gradients can appear at the edges of the substrate. As a result, wafer bowing was observed with a saddle-like shape. The EBL available at EPFL requires a constant surface height. Initially, the wafers displayed

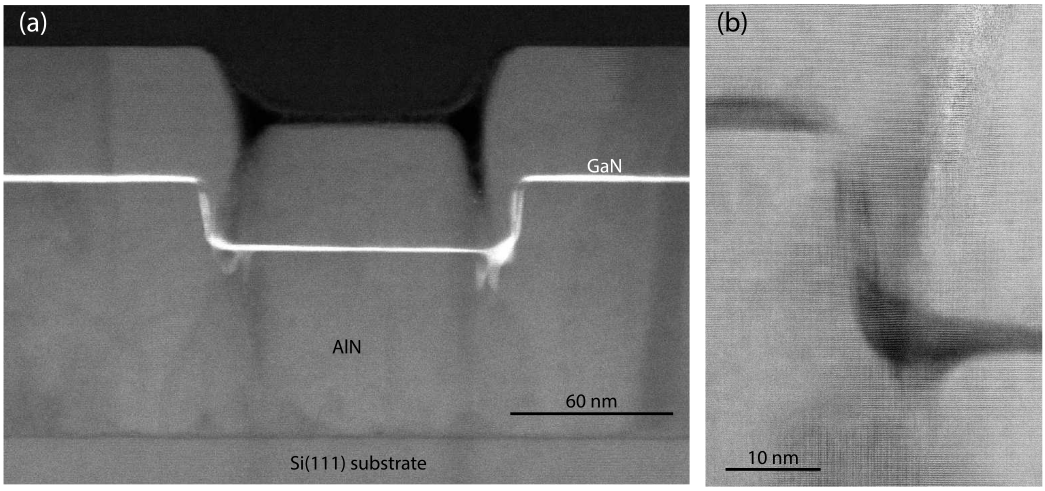

Figure A.1 – Transmission electron microscope images of the optimized SC-QD structure. (a) High-angle annular dark-field image of the overview of the structure and (b) High resolution annular bright-field image of a site controlled GaN QD.

bowing values outside the tolerance of the instrument. The problem was solved by swapping the 250 μm thick substrates for 500 μm thick ones. The increased substrate thickness results in a stiffer substrate that is less prone to deformations.

AlN on Si(111) layers exhibit high tensile strain due to the difference in TEC. It was observed that performing EBL and the subsequent dry-etching resulted in the formation of cracks in the AlN. At this initial stage, the process flow consisted of directly spin-coating the surface with *ZEP* resist, followed by EBL and inductive coupled plasma (ICP) etching in Cl_2/N_2 and finally resist removal by O_2 plasma. Along with the cracks, the reentry into the MBE chamber and heating to growth temperature revealed a blurry RHEED. The RHEED would immediately become spotty upon regrowth of only 1-2 nm of AlN. The surfaces were measured by energy dispersive X-ray (EDX) spectroscopy in a SEM microscope and oxygen and carbon impurities were identified. The surface contamination was solved by changing the process flow; an intermediate SiO_2 layer was introduced between the AlN surface and the resist. A pattern transfer from the resist to the SiO_2 was employed and the O_2 plasma step discarded. The ICP dry etching was adjusted so that it also removed the *ZEP* resist. Finally the sample was stripped of the SiO_2 layer by BHF. By following this procedure, a clean AlN surface, suitable for regrowth could be recovered. Further on, cracks were almost completely suppressed with the new process. The nanofabrication was optimized to such a degree that no regrowth interface can be observed by TEM.

The pattern itself consisted of a variety of shapes: circles, triangles and hexagons. The triangles and hexagons were either aligned with the crystallographic axes or rotated by $\pi/2$. Further on, the diameter of the etch holes was varied from 20 to 200 nm in diameter.

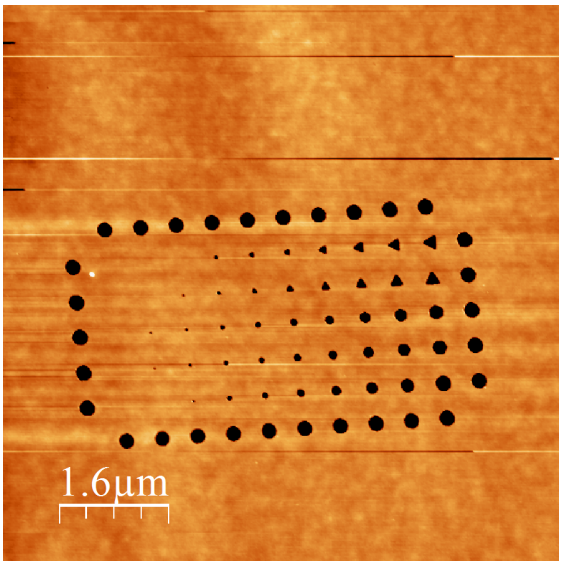

Figure A.2 – 8 × 8 μm^2 AFM image of the patterned substrate presenting the various shapes and sizes. The depth of the etch pits is around 20 nm.

Finally, the pitch between etch holes was adjusted for each characterization technique. A very small pitch, 100 to 200 nm was employed for areas aimed at TEM measurements. For AFM and CL measurements, the pitch was enlarged to 500 nm and up to 5 μm for μ-PL. An AFM image of the patterned surface is displayed in figure A.2.

Several regrowth attempts were performed on these patterned substrates either by MOVPE by Dr. J. F. Carlin or by NH_3-MBE. Various QW thicknesses were tested as well as AlGaN barriers. The best results were achieved for a 2 nm thick GaN QW with AlN barriers grown by MBE, which corresponds to the sample from figure A.1. A major issue concerning the growth of the active region were thickness fluctutations that led to localized emission outside of the patterned area, this emission appeared QD-like with sharp features. In order to minimize the QD-like features outside the patterned area, the growth conditions for the AlN top barrier and the QW were optimized. The best results were obtained when using a constant growth temperature of 830 °C for the GaN QW and the AlN top barrier. The results of chapter 3 suggest that in order to prevent roughening of the surface and hence avert spurious QD-like features the NH_3 impinging flux should be maximized. An NH_3 flow of 200 sccm was used throughout the regrowth procedure.

CL is particularly well suited for spectroscopy with a very high spatial resolution. Another important difference of between the μ-PL capabilities of our setup and CL is the excitation channel; the available lasers in the μ-PL are not sufficiently energetic to create excitons in the AlN, whereas in CL the barriers are excited. The excitons in the barrier can then transfer to the local energy minimum, i. e., the QD. As a result, the excitation rate is higher with CL. In figure A.3 an SEM of the nanostructures is presented along with the corresponding CL mapping. The mapping plots intensity for each position for

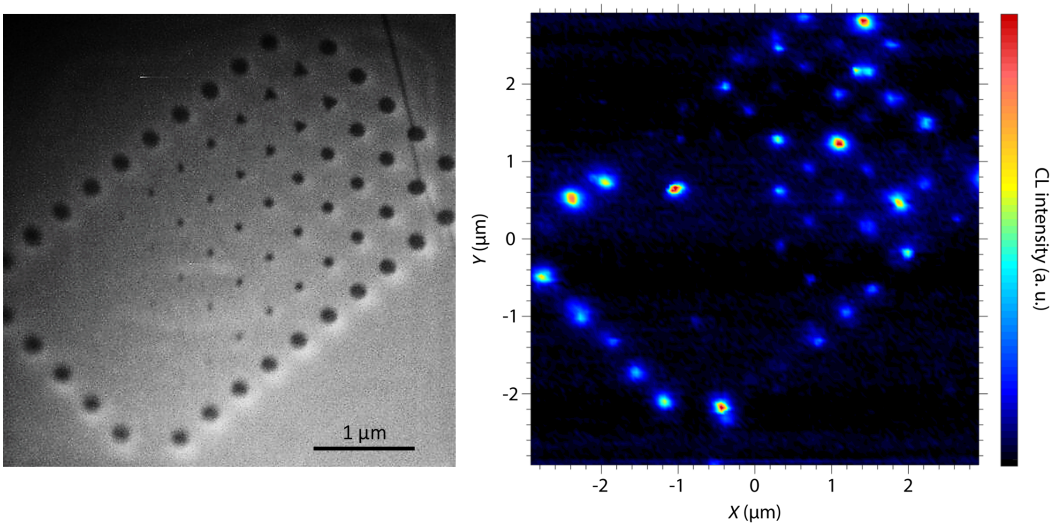

Figure A.3 – SEM and corresponding cathodoluminescence mapping of the emission intensity filtered from 4 to 5 eV. The sample temperature is 5 K.

an emission energy between 4 and 5 eV. It is clear that most of the pattern's sites are optically active. The same experiments were carried out on a sample consisting of the same patterning and regrowth but without a GaN QW. This sample does not present any emission at these energies, thus excluding a contamination, impurity or damage from the EBL as the light source. In fact, it only displays the usual blue band defect emission common to all AlN on Si layers grown throughout this thesis.

So far, the nanostructures have been demonstrated to be optically active and their position predetermined by the EBL patterning. A QD-like optical signature was suggested by μ-PL experiments. Linewidth statistics were also collected for this sample and shown in figure A.4 (a) along with those reported in chapter 4. Some outliers are found in the data of the SC-QD, but they overall fit within the trend of SK-QDs.

Given the geometry of the nanostructures, a single dip in the sample can host several QDs. The TEM images show that an m-plane QW is also present at the side walls of the dip and QD-like features are observed in the edges. As a result, the spectra are extremely complicated and an analysis similar to the one presented in chapter 4 is unrealistic. Further on, although the growth was optimized to minimize ML fluctuations in the QW that could be potentially misleading, μ-PL revealed sharp lines well outside of the patterned areas. Consequentially, most of the data analysis revolved around identifying the spectral features that could be potentially tied to SC-QDs. An exemplary μ-PL spectrum as a function of excitation power is displayed in figure A.4 (b). A peak suggesting a biexcitonic transition is marked with an arrow. Further data, such as time series and polarization would be required to identify its corresponding exciton.

In conclusion, EBL and MBE were employed to create site controlled QD-like nanostruc-

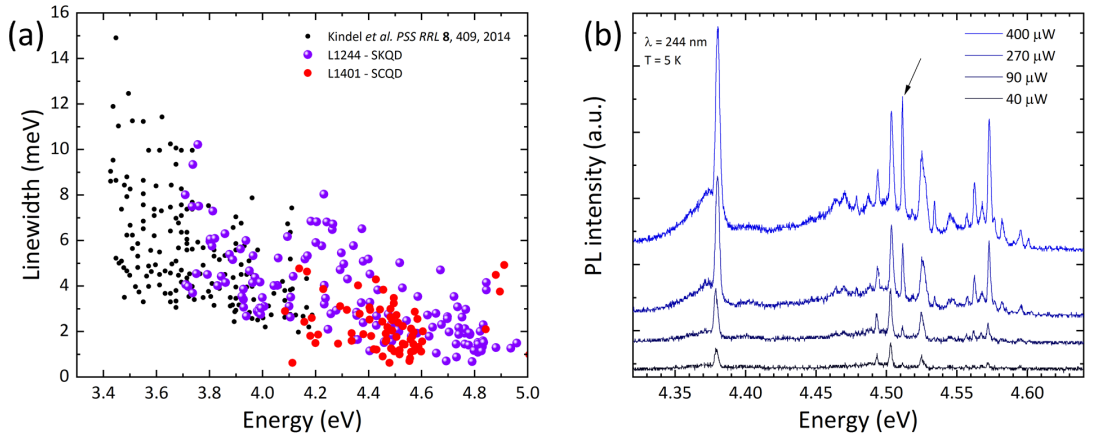

Figure A.4 – (a) Linewidth statistics at 5 K for SK-QD (black and violet dots) and of the SC-QD (red dots). (b) Exemplary μ-PL spectrum of a SC-QD position. The arrow denotes a line suggesting a biexciton.

tures on Si(111) substrates. The planar nature of the sample and the use of Si substrates renders the approach compatible with membrane photonic crystals. However, further work would be required to understand the optical features of the nanostructures and to minimize spurious emission from unpatterned areas.

B Appendix: Challenges for the MBE growth on AlN single crystal substrates

Epitaxy on AlN single crystal substrates offers the advantage of working on substrates with very low TDD ($\sim 10^3$ cm^{-2}). Dislocations have been identified to be non-radiative recombination centers and thus the reduction of the TDD is crucial for device applications such as LEDs and lasers [188, 189]. AlN single crystal substrates have only become available recently and are quite expensive. For this reason, the substrates were cut by laser ablation into 5×5 mm^2 pieces, see figure B.1 (a). During the cutting process the substrates were exposed to a contaminating environment. An optical microscopy image of a 5×5 mm^2 piece exhibiting severe surface contamination is displayed in figure B.1. A cleaning procedure was implemented based on the recommendations of provided by the supplier, HexaTech Inc. However, instead of degreasing acetone and methanol, as suggested by the supplier, the organic compounds were removed in an ultrasonic bath of *1165 resist remover* at a temperature of 90 °C. The substrates were also wet etched in 3:1 sulfuric acid : phosphoric acid at a temperature of 85 °C. The procedure was repeated several times until no traces of contamination could be observed. An optical microscopy image of a cleaned AlN piece is shown in figure B.1 (c). For future work, the substrates could be protected with a layer of SiO_2 before laser cutting. As seen in the previous appendix, an epiready surface can be recovered after removing the SiO_2 with BHF. Then the cumbersome chemical cleaning could be avoided.

MBE growth on small pieces is often performed by "glueing" the sample to a dummy substrate with In. The sample is held in place by a Van der Waals force, the procedure is compatible with UHV and high temperatures. A key requirement is needed to ensure thermal and mechanical stability, the surface of the sample and the dummy substrate have to be extremely flat. The AlN pieces proved to be too rough to enable In glueing. Substrate holders for such small pieces are not commercially available, instead special holders made out of pure Mo were designed and manufactured in the workshop of the Institute of Physics. Two designs were produced, the first one has no moving pieces and has been labeled as uniblock, see figure B.1 (d). The second one, designed by D. Martin (former LASPE engineer), employs a spring that applies a force on one of the edges

Appendix B. Appendix: Challenges for the MBE growth on AlN single crystal substrates

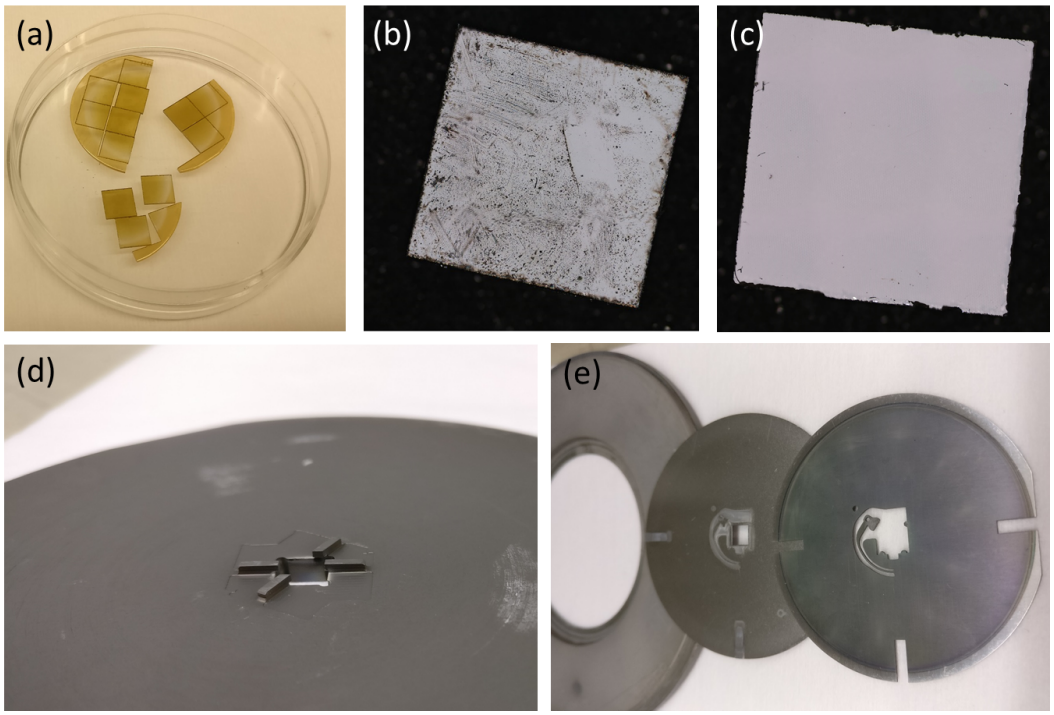

Figure B.1 – (a) 1 inch AlN single crystal substrate after laser cutting into 5 × 5 mm^2 pieces. (b) Optical microscopy image of a piece of AlN single crystal after laser cutting and after chemical cleaning (c). (d) Sample holder for 5 × 5 mm^2 pieces, labeled as uniblock. (e) Disassembled sample holder referred to as spring holder.

of the square sample. Both holders were tested to be reliable and practical with their own advantages and disadvantages. The uniblock holder requires a high precision of the sample size and shape but offers a better pyrometric temperature estimation. For the uniblock holder the emissivity of the pyrometer can be calibrated to display a realistic temperature, however for the spring holder the pyrometer's reading overestimates the temperature even when setting the emissivity to its maximum value of 1.

Bibliography

[1] B. Damilano, N. Grandjean, F. Semond, J. Massies, and M. Leroux, "From visible to white light emission by GaN quantum dots on Si(111) substrate", Appl. Phys. Lett. **75**, 962 (1999).

[2] T. C. Ralph and P. K. Lam, "A bright future for quantum communications", Nature Photonics **3**, 671 (2009).

[3] R. J. D. Tilley, Crystals and crystal structures, John Wiley & Sons (2006).

[4] R. Butté and N. Grandjean, "Effects of Polarization in Optoelectronic Quantum Structures", in C. Wood and D. Jena (Editors), "Polarization Effects in Semiconductors from Ab Initio Theory to Device Applications", page 467, Springer (2007).

[5] G. Rossbach, "High-Density Excitonic Effects in GaN Mott-Transition and Polariton Lasing", Ph.D. thesis, Lausanne (2014).

[6] R. Nowak, M. Pessa, M. Suganuma, M. Leszczynski, I. Grzegory, S. Porowski, and F. Yoshida, "Elastic and plastic properties of GaN determined by nano-indentation of bulk crystal", Appl. Phys. Lett. **75**, 2070–2072 (1999).

[7] I. Yonenaga, T. Shima, and M. H. F. Sluiter, "Nano-Indentation Hardness and Elastic Moduli of Bulk Single-Crystal AlN", Jpn. J. Appl. Phys. **41**, 4620–4621 (2002).

[8] N. Sinha, G. E. Wabiszewski, R. Mahameed, V. V. Felmetsger, S. M. Tanner, R. W. Carpick, and G. Piazza, "Piezoelectric aluminum nitride nanoelectromechanical actuators", Appl. Phys. Lett. **95**, 053106 (2009).

[9] C. Giordano, I. Ingrosso, M. Todaro, G. Maruccio, S. De Guido, R. Cingolani, A. Passaseo, and M. De Vittorio, "AlN on polysilicon piezoelectric cantilevers for sensors/actuators", Microelectron. Eng. **86**, 1204–1207 (2009).

[10] I. Vurgaftman and J. R. Meyer, "Band parameters for nitrogen-containing semiconductors", Journal of Applied Physics **94**, 3675–3696 (2003).

[11] M. Feneberg, B. Neuschl, K. Thonke, R. Collazo, A. Rice, Z. Sitar, R. Dalmau, J. Xie, S. Mita, and R. Goldhahn, "Sharp bound and free exciton lines from homoepitaxial AlN", Phys. status solidi **208**, 1520–1522 (2011).

[12] J. Wu, W. Walukiewicz, W. Shan, K. M. Yu, J. W. Ager, S. X. Li, E. E. Haller, H. Lu, and W. J. Schaff, "Temperature dependence of the fundamental band gap of InN", J. Appl. Phys. **94**, 4457–4460 (2003).

[13] C. F. Klingshirn, Semiconductor Optics, Springer (1995).

[14] M. Suzuki, T. Uenoyama, and A. Yanase, "First-principles calculations of effective-mass parameters of AlN and GaN", Phys. Rev. B **52**, 8132–8139 (1995).

[15] R. Butté, J.-F. Carlin, E. Feltin, M. Gonschorek, S. Nicolay, G. Christmann, D. Simeonov, A. Castiglia, J. Dorsaz, H. J. Buehlmann, S. Christopoulos, G. Baldassarri Höger von Hög, A. J. D. Grundy, M. Mosca, C. Pinquier, M. A. Py, F. Demangeot, J. Frandon, P. G. Lagoudakis, J. J. Baumberg, and N. Grandjean, "Current status of AlInN layers lattice-matched to GaN for photonics and electronics", J. Phys. D. Appl. Phys. **40**, 6328–6344 (2007).

[16] F. Bernardini, V. Fiorentini, and D. Vanderbilt, "Spontaneous polarization and piezoelectric constants of III-V nitrides", Phys. Rev. B **56**, R10024–R10027 (1997).

[17] V. Fiorentini, F. Bernardini, and O. Ambacher, "Evidence for nonlinear macroscopic polarization in III–V nitride alloy heterostructures", Applied Physics Letters **80**, 1204–1206 (2002).

[18] A. Zoroddu, F. Bernardini, P. Ruggerone, and V. Fiorentini, "First-principles prediction of structure, energetics, formation enthalpy, elastic constants, polarization, and piezoelectric constants of AlN, GaN, and InN: Comparison of local and gradient-corrected density-functional theory", Phys. Rev. B **64**, 045208 (2001).

[19] M. Born and K. Huang, Dynamical theory of crystal lattices, Clarendon press (1968).

[20] U. M. Christmas, A. Andreev, and D. Faux, "Calculation of electric field and optical transitions in InGaN/ GaN quantum wells", Journal of applied physics **98**, 073522 (2005).

[21] H. Morkoç, Handbook of nitride semiconductors and devices, Materials Properties, Physics and Growth, volume 1, John Wiley & Sons (2009).

[22] F. Schwabl, Quantum Mechanics, Springer Science & Business Media (2007).

[23] D. P. Williams, A. D. Andreev, and E. P. O'Reilly, "Dependence of exciton energy on dot size in GaN/AlN quantum dots", Phys. Rev. B **73**, 241301 (2006).

[24] N. Grandjean and M. Ilegems, "Visible InGaN/GaN Quantum-Dot Materials and Devices", Proc. IEEE **95**, 1853–1865 (2007).

[25] B. Daudin, "Polar and nonpolar GaN quantum dots", J. Phys. Condens. Matter **20**, 473201 (2008).

[26] M. J. Holmes, M. Arita, and Y. Arakawa, "III-nitride quantum dots as single photon emitters", Semicond. Sci. Technol. **34**, 033001 (2019).

[27] F. Widmann, J. Simon, B. Daudin, G. Feuillet, J. L. Rouvière, N. T. Pelekanos, and G. Fishman, "Blue-light emission from GaN self-assembled quantum dots due to giant piezoelectric effect", Phys. Rev. B **58**, R15989–R15992 (1998).

[28] M. Miyamura, K. Tachibana, and Y. Arakawa, "High-density and size-controlled GaN self-assembled quantum dots grown by metalorganic chemical vapor deposition", Appl. Phys. Lett. **80**, 3937–3939 (2002).

[29] J. Tersoff and F. K. LeGoues, "Competing relaxation mechanisms in strained layers", Phys. Rev. Lett. **72**, 3570–3573 (1994).

[30] C. Adelmann, B. Daudin, R. A. Oliver, G. A. D. Briggs, and R. E. Rudd, "Nucleation and Growth of GaN/AlN Quantum Dots", Phys. Rev. B **70**, 125427 (2004).

[31] S. Tamariz, G. Callsen, and N. Grandjean, "Density control of GaN quantum dots on AlN single crystal", Applied Physics Letters **114**, 082101 (2019).

[32] D. Simeonov, A. Dussaigne, R. Butté, and N. Grandjean, "Complex behavior of biexcitons in GaN quantum dots due to a giant built-in polarization field", Phys. Rev. B **77**, 075306 (2008).

[33] C. Adelmann, E. Sarigiannidou, D. Jalabert, Y. Hori, J. L. Rouvière, B. Daudin, S. Fanget, C. Bru-Chevallier, T. Shibata, and M. Tanaka, "Growth and optical properties of GaN/AlN quantum wells", Appl. Phys. Lett. **82**, 4154–4156 (2003).

[34] W. Demtröder, Laser Spectroscopy: Basic Concepts and Instrumentation, Advanced Texts in Physics, Springer Berlin Heidelberg (2002).

[35] G. Hönig, S. Rodt, G. Callsen, I. A. Ostapenko, T. Kure, A. Schliwa, C. Kindel, D. Bimberg, A. Hoffmann, S. Kako, and Y. Arakawa, "Identification of electric dipole moments of excitonic complexes in nitride-based quantum dots", Phys. Rev. B **88**, 045309 (2013).

[36] C. Kindel, G. Callsen, S. Kako, T. Kawano, H. Oishi, G. Hönig, A. Schliwa, A. Hoffmann, and Y. Arakawa, "Spectral diffusion in nitride quantum dots: Emission energy dependent linewidths broadening via giant built-in dipole moments", physica status solidi (RRL) – Rapid Research Letters **8**, 408–413 (2014).

[37] Y. Arakawa and H. Sakaki, "Multidimensional quantum well laser and temperature dependence of its threshold current", Applied Physics Letters **40**, 939–941 (1982).

[38] M. Kneissl, A Brief Review of III-Nitride UV Emitter Technologies and Their Applications, pages 1–25, Springer International Publishing, Cham (2016).

[39] J. Brault, M. A. Khalfioui, S. Matta, B. Damilano, M. Leroux, S. Chenot, M. Korytov, J. E. Nkeck, P. Vennéguès, J. Duboz, J. Massies, and B. Gil, "UVA and UVB light emitting diodes with Al_y Ga_{1-y} N quantum dot active regions covering the 305–335 nm range", Semiconductor Science and Technology **33**, 075007 (2018).

[40] T. Huault, J. Brault, F. Natali, B. Damilano, D. Lefebvre, L. Nguyen, M. Leroux, and J. Massies, "Blue-light emission from $GaN/Al_{0.5}Ga_{0.5}N$ quantum dots", Applied Physics Letters **92**, 051911 (2008).

[41] P. Lambropoulos and D. Petrosyan, Fundamentals of quantum optics and quantum information, volume 23, Springer (2007).

[42] E. Knill, R. Laflamme, and G. J. Milburn, "A scheme for efficient quantum computation with linear optics", Nature **409**, 46–52 (2001).

[43] M. A. Nielsen and I. L. Chuang, Quantum Computation and Quantum Information: 10th Anniversary Edition, Cambridge University Press (2010).

[44] I. Aharonovich, D. Englund, and M. Toth, "Solid-state single-photon emitters", Nat. Photonics **10**, 631–641 (2016).

[45] A. Schliwa, M. Winkelnkemper, A. Lochmann, E. Stock, and D. Bimberg, "In(Ga)As/GaAs quantum dots grown on a (111) surface as ideal sources of entangled photon pairs", Phys. Rev. B **80**, 161307 (2009).

[46] M. J. Holmes, S. Kako, K. Choi, M. Arita, and Y. Arakawa, "Single Photons from a Hot Solid-State Emitter at 350 K", ACS Photonics **3**, 543–546 (2016).

[47] G. Callsen, A. Carmele, G. Hönig, C. Kindel, J. Brunnmeier, M. R. Wagner, E. Stock, J. S. Reparaz, A. Schliwa, S. Reitzenstein, A. Knorr, A. Hoffmann, S. Kako, and Y. Arakawa, "Steering photon statistics in single quantum dots: From one-to two-photon emission", Phys. Rev. B **87**, 245314 (2013).

[48] M. Henini (Editor), Molecular Beam Epitaxy: From Research to Mass Production, Elsevier Science (2012).

[49] M. Knudsen, "Die maximale Verdampfungsgeschwindigkeit des Quecksilbers", Annalen der Physik **352**, 697–708 (1915).

[50] I. Langmuir, "The Vapor Pressure of Metallic Tungsten", Phys. Rev. **2**, 329–342 (1913).

[51] T. Shitara, J. Zhang, J. H. Neave, and B. A. Joyce, "Ga adatom incorporation kinetics at steps on vicinal GaAs (001) surfaces during growth of GaAs by molecular beam epitaxy", Journal of Applied Physics **71**, 4299–4304 (1992).

[52] N. Grandjean and J. Massies, "Epitaxial growth of highly strained $In_xGa_{1-x}As$ on GaAs(001): the role of surface diffusion length", Journal of Crystal Growth **134**, 51–62 (1993).

[53] P. Sohi, D. Martin, and N. Grandjean, "Critical thickness of GaN on AlN: impact of growth temperature and dislocation density", Semicond. Sci. Technol. **32**, 075010 (2017).

[54] M. A. Herman, W. Richter, and H. Sitter, Epitaxy: Physical Principles and Technical Implementation, Springer-Verlag Berlin Heidelberg (2004).

[55] G. Binnig, C. F. Quate, and C. Gerber, "Atomic Force Microscope", Phys. Rev. Lett. **56**, 930–933 (1986).

[56] J. Winkler, M. Neubert, and J. Rudolph, "A Review of the Automation of the Czochralski Crystal Growth Process", ACTA Phys. Pol. A **124**, 181 (2013).

[57] K. Hiramatsu, K. Nishiyama, M. Onishi, H. Mizutani, M. Narukawa, A. Motogaito, H. Miyake, Y. Iyechika, and T. Maeda, "Fabrication and characterization of low defect density GaN using facet-controlled epitaxial lateral overgrowth (FACELO)", Journal of Crystal Growth **221**, 316 – 326 (2000), proc Tenth Int Conf Metalorganic Vapor Phase Epitaxy.

[58] D. Zhuang, Z. Herro, R. Schlesser, and Z. Sitar, "Seeded growth of AlN single crystals by physical vapor transport", Journal of Crystal Growth **287**, 372 – 375 (2006).

[59] A. T. Schremer, J. A. Smart, Y. Wang, O. Ambacher, N. C. MacDonald, and J. R. Shealy, "High electron mobility AlGaN/GaN heterostructure on (111) Si", Applied Physics Letters **76**, 736–738 (2000).

[60] F. Semond, Y. Cordier, N. Grandjean, F. Natali, B. Damilano, S. Vézian, and J. Massies, "Molecular Beam Epitaxy of Group-III Nitrides on Silicon Substrates: Growth, Properties and Device Applications", Physica Status Solidi (a) **188**, 501–510 (2001).

[61] N. Vico Triviño, U. Dharanipathy, J.-F. Carlin, Z. Diao, R. Houdré, and N. Grandjean, "Integrated photonics on silicon with wide bandgap GaN semiconductor", Applied Physics Letters **102**, 081120 (2013).

[62] I. Roland, Y. Zeng, Z. Han, X. Checoury, C. Blin, M. El Kurdi, A. Ghrib, S. Sauvage, B. Gayral, C. Brimont, T. Guillet, F. Semond, and P. Boucaud, "Near-infrared gallium nitride two-dimensional photonic crystal platform on silicon", Applied Physics Letters **105**, 011104 (2014).

[63] N. Vico Triviño, R. Butté, J.-F. Carlin, and N. Grandjean, "Continuous Wave Blue Lasing in III-Nitride Nanobeam Cavity on Silicon", Nano Letters **15**, 1259–1263 (2015).

[64] I. Rousseau, I. Sánchez-Arribas, K. Shojiki, J.-F. Carlin, R. Butté, and N. Grandjean, "Quantification of scattering loss of III-nitride photonic crystal cavities in the blue spectral range", Phys. Rev. B **95**, 125313 (2017).

[65] N. Baron, Y. Cordier, S. Chenot, P. Vennéguès, O. Tottereau, M. Leroux, F. Semond, and J. Massies, "The critical role of growth temperature on the structural and electrical properties of AlGaN/GaN high electron mobility transistor heterostructures grown on Si(111)", J. Appl. Phys. **105**, 033701 (2009).

[66] H. Yacoub, T. Zweipfennig, H. Kalisch, A. Vescan, A. Dadgar, M. Wieneke, J. Bläsing, A. Strittmatter, S. Rennesson, and F. Semond, "Impact of AlN/Si Nucleation Layers Grown Either by NH_3-MBE or MOCVD on the Properties of AlGaN/GaN HFETs", Phys. Status Solidi **215**, 1700638 (2018).

[67] R. Liu, F. a. Ponce, a. Dadgar, and a. Krost, "Atomic arrangement at the AIN/Si (111) interface", Appl. Phys. Lett. **83**, 860–862 (2003).

[68] F. Semond, "Epitaxial Challenges of GaN on Silicon", MRS Bulletin **40**, 412 (2015).

[69] A. Krost and A. Dadgar, "GaN-Based Devices on Si", Physica Status Solidi (a) **194**, 361 (2002).

[70] S. Tamariz, D. Martin, and N. Grandjean, "AlN grown on Si(1 1 1) by ammonia-molecular beam epitaxy in the 900 - 1200 °C temperature range", J. Cryst. Growth **476**, 58 (2017).

[71] S. Yoshida, S. Misawa, and S. Gonda, "Improvements on the Electrical and Luminescent Properties of Reactive Molecular Beam Epitaxially Grown GaN Gilms by Using AlN-coated Sapphire Substrates", Applied Physics Letters **42**, 427 (1983).

[72] C. A. Tran, A. Osinski, R. F. Karlicek, and I. Berishev, "Growth of InGaN/GaN multiple-quantum-well blue light-emitting diodes on silicon by metalorganic vapor phase epitaxy", Applied Physics Letters **75**, 1494–1496 (1999).

[73] A. Dadgar, "Sixteen years GaN on Si", physica status solidi (b) **252**, 1063–1068 (2015).

[74] J. W. Yang, C. J. Sun, Q. Chen, M. Z. Anwar, M. Asif Khan, S. A. Nikishin, G. A. Seryogin, A. V. Osinsky, L. Chernyak, H. Temkin, C. Hu, and S. Mahajan, "High quality GaN–InGaN heterostructures grown on (111) silicon substrates", Applied Physics Letters **69**, 3566–3568 (1996).

[75] A. Strittmatter, A. Krost, M. Straßburg, V. Türck, D. Bimberg, J. Bläsing, and J. Christen, "Low-pressure metal organic chemical vapor deposition of GaN on silicon(111) substrates using an AlAs nucleation layer", Applied Physics Letters **74**, 1242–1244 (1999).

[76] T. Takeuchi, H. Amano, K. Hiramatsu, N. Sawaki, and I. Akasaki, "Growth of single crystalline GaN film on Si substrate using 3C-SiC as an intermediate layer", J. Cryst. Growth **115**, 634–638 (1991).

[77] A. E. Romanov and J. S. Speck, "Stress relaxation in mismatched layers due to threading dislocation inclination", Applied Physics Letters **83**, 2569–2571 (2003).

[78] M. A. Sanchez-Garcia, E. Calleja, E. Monroy, F. J. Sanchez, F. Calle, E. Muñoz, and R. Beresford, "The effect of the III/V ratio and substrate temperature on the morphology and properties of GaN- and AlN-layers grown by molecular beam epitaxy on Si(1 1 1)", Journal of Crystal Growth **183**, 23 (1998).

[79] S. A. Nikishin, V. G. Antipov, S. Francoeur, N. N. Faleev, G. a. Seryogin, V. A. Elyukhin, and S. Zollner, "High-quality AlN grown on Si(111) by gas-source molecular-beam epitaxy with ammonia", Applied Physics Letters **75**, 484 (1999).

[80] F. Semond, B. Damilano, S. Vézian, N. Grandjean, M. Leroux, and J. Massies, "GaN grown on Si(111) substrate: From two-dimensional growth to quantum well assessment", Applied Physics Letters **75**, 82 (1999).

[81] M. Yoshimura, E. Takahashi, and T. Yao, "Initial stages of the nitridation of the Si(111) surface observed by scanning tunneling microscopy", Journal of Vacuum Science and Technology B: Microelectronics and Nanometer Structures **14**, 1048 (1996).

[82] Y. Nakada, I. Aksenov, and H. Okumura, "GaN heteroepitaxial growth on silicon nitride buffer layers formed on Si (111) surfaces by plasma-assisted molecular beam epitaxy", Applied Physics Letters **73**, 827 (1998).

[83] N. Yamabe, H. Shimomura, T. Shimamura, and T. Ohachi, "Nitridation of Si(111) for growth of 2H-AlN(0001)/β-Si3N4 /Si(111) structure", Journal of Crystal Growth **311**, 3049 (2009).

[84] V. Mansurov, X. Xu, M. Pandikunta, R. Uddin, and S. Nikishin, "Reflection high energy electron diffraction investigation and comparison of the initial stage during molecular beam epitaxy of AlN on Si(111) and Si(110) substrates", Journal of Vacuum Science and Technology B: Microelectronics and Nanometer Structures **29**, 03C129 (2011).

[85] S. Vézian, A. Le Louarn, and J. Massies, "Selective epitaxial growth of AlN and GaN nanostructures on Si(111) by using NH_3 as nitrogen source", Journal of Crystal Growth **303**, 419 (2007).

[86] A. Le Louarn, S. Vézian, F. Semond, and J. Massies, "AlN buffer layer growth for GaN epitaxy on (111) Si: Al or N first?", Journal of Crystal Growth **311**, 3278 (2009).

[87] W. Kern and D. A. Puotinen, "Cleaning solutions based on hydrogen peroxide for use in silicon semiconductor technology", RCA Rev **31**, 187 (1970).

[88] A. Ishizaka and Y. Shiraki, "Low Temperature Surface Cleaning of Silicon and Its Application to Silicon MBE", Journal of The Electrochemical Society **133**, 666 (1986).

[89] F. Xie, P. Von Blanckenhagen, J. Wu, J. W. Liu, Q. Z. Zhang, Y. C. Chen, and E.-G. Wang, "Contamination of Si surfaces in ultrahigh vacuum and formation of SiC islands", Applied Surface Science **181**, 139 (2001).

[90] Y. Kobayashi, Y. Shinoda, and K. Sugii, "Thermal Desorption from Si(111) Surfaces with Native Oxides Formed During Chemical Treatments", Jpn. J. Appl. Phys. **29**, 1004–1008 (1990).

[91] M. J. Kim and R. W. Carpenter, "Composition and structure of native oxide on silicon by high resolution analytical electron microscopy", Journal of Materials Research **5**, 347 (1990).

[92] A. Le Louarn, "Premiere étape de la croissance de GaN sur Si(111) : la nucléation d'AlN", Ph.D. thesis, Universite de Nice-Sophia Antipolis (2006).

[93] R. E. Schlier and H. E. Farnsworth, "Structure and Adsorption Characteristics of Clean Surfaces of Germanium and Silicon", J. Chem. Phys. **30**, 917–926 (1959).

[94] K. Takayanagi, Y. Tanishiro, M. Takahashi, and S. Takahashi, "Structural analysis of Si(111) 7x7 by UHV transmission electron diffraction and microscopy", J. Vac. Sci. Technol. A Vacuum, Surfaces, Film. **3**, 1502–1506 (1985).

[95] A. V. Zotov and A. A. Saranin, "DAS model", Glossary of nanotechnology and related terms Url: http://eng.thesaurus.rusnano.com/wiki/article14156, Visited on 2019.01.08.

[96] N. Grandjean, J. Massies, F. Semond, S. Y. Karpov, and R. A. Talalaev, "GaN evaporation in molecular-beam epitaxy environment", Appl. Phys. Lett. **74**, 1854 (1999).

[97] C. S. Gallinat, G. Koblmüller, J. S. Brown, and J. S. Speck, "A growth diagram for plasma-assisted molecular beam epitaxy of In-face InN", J. Appl. Phys. **102**, 064907 (2007).

[98] N. Grandjean, J. Massies, P. Vennéguès, M. Leroux, F. Demangeot, M. Renucci, and J. Frandon, "Molecular-beam epitaxy of gallium nitride on (0001) sapphire substrates using ammonia", J. Appl. Phys. **83**, 1379 (1998).

[99] N. A. Kaufmann, L. Lahourcade, B. Hourahine, D. Martin, and N. Grandjean, "Critical impact of Ehrlich–Schwöbel barrier on GaN surface morphology during homoepitaxial growth", J. Cryst. Growth **433**, 36–42 (2016).

[100] M.A. Sanchez-Garcia and E. Calleja and E. Monroy and F.J. Sanchez and F. Calle and E. Muñoz and R. Beresford, "The effect of the III/V ratio and substrate temperature on the morphology and properties of GaN- and AlN-layers grown by molecular beam epitaxy on Si(1 1 1)", Journal of Crystal Growth **183**, 23 – 30 (1998).

[101] M. Mesrine, N. Grandjean, and J. Massies, "Efficiency of NH_3 as nitrogen source for GaN molecular beam epitaxy", Applied Physics Letters **72**, 350 (1998).

[102] J. R. Lang and J. S. Speck, "NH_3-rich growth of InGaN and InGaN/GaN superlattices by NH 3-based molecular beam epitaxy", J. Cryst. Growth **346**, 50–55 (2012).

[103] B. Heying, X. H. Wu, S. Keller, Y. Li, D. Kapolnek, B. P. Keller, S. DenBaars, and J. S. Speck, "Role of threading dislocation structure on the x-ray diffraction peak widths in epitaxial GaN films", Applied Physics Letters **68**, 643 (1996).

[104] M. Pandikunta, O. Ledyaev, V. Kuryatkov, and S. A. Nikishin, "Structural analysis of N-polar AlN layers grown on Si (111) substrates by high resolution X-ray diffraction", Physica Status Solidi (C) **11**, 487–490 (2014).

[105] S. Nakamura, "GaN Growth Using GaN Buffer Layer", Japanese Journal of Applied Physics **30**, L1705 (1991).

[106] H. Lahrèche, P. Vennéguès, B. Beaumont, and P. Gibart, "Growth of high-quality GaN by low-pressure metal-organic vapour phase epitaxy (LP-MOVPE) from 3D islands and lateral overgrowth", Journal of Crystal Growth **205**, 245 – 252 (1999).

[107] G. Callsen, M. R. Wagner, J. S. Reparaz, F. Nippert, T. Kure, S. Kalinowski, A. Hoffmann, M. J. Ford, M. R. Phillips, R. F. Dalmau, R. Schlesser, R. Collazo, and Z. Sitar, "Phonon pressure coefficients and deformation potentials of wurtzite AlN determined by uniaxial pressure-dependent Raman measurements", Physical Review B **90**, 205206 (2014).

[108] S. Figge, H. Kröncke, D. Hommel, and B. M. Epelbaum, "Temperature dependence of the thermal expansion of AlN", Applied Physics Letters **94**, 101915 (2009).

[109] Y. Okada and Y. Tokumaru, "Precise determination of lattice parameter and thermal expansion coefficient of silicon between 300 and 1500 K", Journal of Applied Physics **56**, 314–320 (1984).

[110] T. Böttcher, S. Einfeldt, S. Figge, R. Chierchia, H. Heinke, D. Hommel, and J. S. Speck, "The role of high-temperature island coalescence in the development of stresses in GaN films", Applied Physics Letters **78**, 1976–1978 (2001).

[111] A. Ekimov, A. Efros, and A. Onushchenko, "Quantum size effect in semiconductor microcrystals", Solid State Commun. **56**, 921–924 (1985).

[112] N. N. Ledentsov, "Quantum dot laser", Semiconductor Science and Technology **26**, 014001 (2010).

[113] C. Santori, D. Fattal, J. Vučković, G. S. Solomon, and Y. Yamamoto, "Indistinguishable photons from a single-photon device", Nature **419**, 594–597 (2002).

[114] N. Akopian, N. H. Lindner, E. Poem, Y. Berlatzky, J. Avron, D. Gershoni, B. D. Gerardot, and P. M. Petroff, "Entangled Photon Pairs from Semiconductor Quantum Dots", Physical Review Letters **96**, 130501 (2006).

[115] V. Giovannetti, S. Lloyd, and L. Maccone, "Advances in quantum metrology", Nature Photonics **5**, 222–229 (2011).

[116] Y. Yin and A. P. Alivisatos, "Colloidal nanocrystal synthesis and the organic–inorganic interface", Nature **437**, 664–670 (2005).

[117] K. Reyes, P. Smereka, D. Nothern, J. M. Millunchick, S. Bietti, C. Somaschini, S. Sanguinetti, and C. Frigeri, "Unified model of droplet epitaxy for compound semiconductor nanostructures: Experiments and theory", Phys. Rev. B **87**, 165406 (2013).

[118] V. A. Shchukin and D. Bimberg, "Spontaneous ordering of nanostructures on crystal surfaces", Rev. Mod. Phys. **71**, 1125–1171 (1999).

[119] P. Alivisatos, "The use of nanocrystals in biological detection", Nature Biotechnology **22**, 47–52 (2004).

[120] S. Coe-Sullivan, W. Liu, P. Allen, and J. S. Steckel, "Quantum Dots for LED Downconversion in Display Applications", ECS Journal of Solid State Science and Technology **2**, R3026–R3030 (2013).

[121] O. Shchekin and D. Deppe, "1.3 μm InAs quantum dot laser with $T_0 = 161$ K from 0 to 80 °C", Applied Physics Letters **80**, 3277–3279 (2002).

[122] D. Ellis, A. Bennett, C. Dangel, J. Lee, J. Griffiths, T. Mitchell, T.-K. Paraiso, P. Spencer, D. Ritchie, and A. Shields, "Independent indistinguishable quantum light sources on a reconfigurable photonic integrated circuit", Applied Physics Letters **112**, 211104 (2018).

[123] F. Tinjod and H. Mariette, "Self-assembled quantum dot formation induced by surface energy change of a strained two-dimensional layer", Phys. status solidi **241**, 550–557 (2004).

[124] E. Martinez-Guerrero, F. Chabuel, B. Daudin, J. L. Rouvière, and H. Mariette, "Control of the morphology transition for the growth of cubic GaN/AlN nanostructures", Appl. Phys. Lett. **81**, 5117–5119 (2002).

[125] F. Tinjod, B. Gilles, S. Moehl, K. Kheng, and H. Mariette, "II–VI quantum dot formation induced by surface energy change of a strained layer", Appl. Phys. Lett. **82**, 4340–4342 (2003).

[126] J. Gérard, J. Génin, J. Lefebvre, J. Moison, N. Lebouché, and F. Barthe, "Optical investigation of the self-organized growth of InAs/GaAs quantum boxes", J. Cryst. Growth **150**, 351–356 (1995).

[127] J. Brown, F. Wu, P. M. Petroff, and J. S. Speck, "GaN quantum dot density control by RF-plasma molecular beam epitaxy", Appl. Phys. Lett. **84**, 690–692 (2004).

[128] B. Damilano, J. Brault, and J. Massies, "Formation of GaN quantum dots by molecular beam epitaxy using NH_3 as nitrogen source", J. Appl. Phys. **118**, 24304 (2015).

[129] S. Sergent, B. Damilano, T. Huault, J. Brault, M. Korytov, O. Tottereau, P. Vennéguès, M. Leroux, F. Semond, and J. Massies, "Study of the growth mechanisms of GaN/(Al, Ga)N quantum dots: Correlation between structural and optical properties", J. Appl. Phys. **109**, 053514 (2011).

[130] V. G. Mansurov, Y. G. Galitsyn, A. Y. Nikitin, K. S. Zhuravlev, and P. Vennéguès, "Investigation of growth mechanisms of GaN quantum dots on (0001)AlN surface by ammonia MBE", Phys. status solidi **3**, 1548–1551 (2006).

[131] D. Simeonov, E. Feltin, J.-F. Carlin, R. Butté, M. Ilegems, and N. Grandjean, "Stranski-Krastanov GaN/AlN quantum dots grown by metal organic vapor phase epitaxy", J. Appl. Phys. **99**, 083509 (2006).

[132] G. Schmidt, C. Berger, P. Veit, S. Metzner, F. Bertram, J. Bläsing, A. Dadgar, A. Strittmatter, J. Christen, G. Callsen, S. Kalinowski, and A. Hoffmann, "Direct evidence of single quantum dot emission from GaN islands formed at threading dislocations using nanoscale cathodoluminescence: A source of single photons in the ultraviolet", Appl. Phys. Lett. **106**, 252101 (2015).

[133] G. Koblmüller, S. Fernández-Garrido, E. Calleja, and J. S. Speck, "In situ investigation of growth modes during plasma-assisted molecular beam epitaxy of (0001) GaN", Applied Physics Letters **91**, 161904 (2007).

[134] N. Grandjean, J. Massies, P. Vennéguès, M. Leroux, F. Demangeot, M. Renucci, and J. Frandon, "Molecular-beam epitaxy of gallium nitride on (0001) sapphire substrates using ammonia", Journal of Applied Physics **83**, 1379–1383 (1998).

[135] H. Mariette, "Formation of self-assembled quantum dots induced by the Stranski–Krastanow transition: a comparison of various semiconductor systems", Comptes Rendus Phys. **6**, 23–32 (2005).

[136] N. P. Kobayashi, T. R. Ramachandran, P. Chen, and A. Madhukar, "In situ, atomic force microscope studies of the evolution of InAs three dimensional islands on GaAs(001)", Applied Physics Letters **68**, 3299–3301 (1996).

[137] D. Leonard, K. Pond, and P. M. Petroff, "Critical layer thickness for self-assembled InAs islands on GaAs", Phys. Rev. B **50**, 11687–11692 (1994).

[138] T. Konishi, E. Clarke, C. W. Burrows, J. J. Bomphrey, R. Murray, and G. R. Bell, "Spatial regularity of InAs-GaAs quantum dots: quantifying the dependence of lateral ordering on growth rate", Scientific Reports **7**, 42606 (2017).

[139] B. Alloing, C. Zinoni, V. Zwiller, L. H. Li, C. Monat, M. Gobet, G. Buchs, A. Fiore, E. Pelucchi, and E. Kapon, "Growth and characterization of single quantum dots emitting at 1300 nm", Appl. Phys. Lett. **86**, 101908–131102 (2005).

[140] J. L. Rouvière, J. Simon, N. Pelekanos, B. Daudin, and G. Feuillet, "Preferential nucleation of GaN quantum dots at the edge of AlN threading dislocations", Cit. Appl. Phys. Lett. Cond. AlN J. Appl. Phys. J. Appl. Phys. **75**, 2632–2254 (1999).

[141] C. Zhao, Y. Xing, C. Zhou, and P. Bai, "Experimental examination of displacement and strain fields in an edge dislocation core", Acta Mater. **56**, 2570–2575 (2008).

[142] C. D. Lee, Y. Dong, R. M. Feenstra, J. E. Northrup, and J. Neugebauer, "Reconstructions of the AlN(0001) surface", Phys. Rev. B **68**, 205317 (2003).

[143] N. Gmeinwieser and U. T. Schwarz, "Pattern formation and directional and spatial ordering of edge dislocations in bulk GaN: Microphotoluminescence spectra and continuum elastic calculations", Phys. Rev. B **75**, 245213 (2007).

[144] P. B. Joyce, T. J. Krzyzewski, G. R. Bell, T. S. Jones, S. Malik, D. Childs, and R. Murray, "Effect of growth rate on the size, composition, and optical properties of InAs/GaAs quantum dots grown by molecular-beam epitaxy", Phys. Rev. B **62**, 10891–10895 (2000).

[145] V. Shchukin, N. Ledentsov, A. Hoffmann, D. Bimberg, I. Soshnikov, B. Volovik, V. Ustinov, D. Litvinov, and D. Gerthsen, "Entropy-Driven Effects in Self-Organized Formation of Quantum Dots", Phys. status solidi **224**, 503–508 (2001).

[146] I. Bryan, Z. Bryan, S. Mita, A. Rice, J. Tweedie, R. Collazo, and Z. Sitar, "Surface kinetics in AlN growth: A universal model for the control of surface morphology in III-nitrides", J. Cryst. Growth **438**, 81–89 (2016).

[147] T. Bretagnon, P. Lefebvre, P. Valvin, R. Bardoux, T. Guillet, T. Taliercio, B. Gil, N. Grandjean, F. Semond, B. Damilano, A. Dussaigne, and J. Massies, "Radiative lifetime of a single electron-hole pair in GaN/AlN quantum dots", Phys. Rev. B **73**, 113304 (2006).

[148] J. Simon, N. T. Pelekanos, C. Adelmann, E. Martinez-Guerrero, R. André, B. Daudin, L. S. Dang, and H. Mariette, "Direct comparison of recombination dynamics in cubic and hexagonal GaN/AlN quantum dots", Phys. Rev. B **68**, 035312 (2003).

[149] S. Kako, K. Hoshino, S. Iwamoto, S. Ishida, and Y. Arakawa, "Exciton and biexciton luminescence from single hexagonal GaN/AlN self-assembled quantum dots", Applied Physics Letters **85**, 64–66 (2004).

[150] S. Kako, C. Santori, K. Hoshino, S. Götzinger, Y. Yamamoto, and Y. Arakawa, "A gallium nitride single-photon source operating at 200 K.", Nat. Mater. **5**, 887–892 (2006).

[151] G. Hönig, G. Callsen, A. Schliwa, S. Kalinowski, C. Kindel, S. Kako, Y. Arakawa, D. Bimberg, and A. Hoffmann, "Manifestation of unconventional biexciton states in quantum dots", Nat. Commun. **5**, 5721 (2014).

[152] C. Kindel, S. Kako, T. Kawano, H. Oishi, Y. Arakawa, G. Hönig, M. Winkelnkemper, a. Schliwa, a. Hoffmann, and D. Bimberg, "Exciton fine-structure splitting in GaN/AlN quantum dots", Phys. Rev. B - Condens. Matter Mater. Phys. **81**, 2–5 (2010).

[153] R. Bardoux, T. Guillet, P. Lefebvre, T. Taliercio, T. Bretagnon, S. Rousset, B. Gil, and F. Semond, "Photoluminescence of single GaN/AlN hexagonal quantum dots on Si(111): Spectral diffusion effects", Phys. Rev. B **74**, 195319 (2006).

[154] M. Holmes, S. Kako, K. Choi, M. Arita, and Y. Arakawa, "Spectral diffusion and its influence on the emission linewidths of site-controlled GaN nanowire quantum dots", Phys. Rev. B **92**, 115447 (2015).

[155] I. a. Ostapenko, G. Hönig, S. Rodt, A. Schliwa, A. Hoffmann, D. Bimberg, M. R. Dachner, M. Richter, A. Knorr, S. Kako, and Y. Arakawa, "Exciton acoustic-phonon coupling in single GaN/AlN quantum dots", Phys. Rev. B - Condens. Matter Mater. Phys. **85**, 3–6 (2012).

[156] G. Callsen, G. M. O. Pahn, S. Kalinowski, C. Kindel, J. Settke, J. Brunnmeier, C. Nenstiel, T. Kure, F. Nippert, A. Schliwa, A. Hoffmann, T. Markurt, T. Schulz, M. Albrecht, S. Kako, M. Arita, and Y. Arakawa, "Analysis of the exciton–LO-phonon coupling in single wurtzite GaN quantum dots", Phys. Rev. B **92**, 235439 (2015).

[157] F. Demangeot, D. Simeonov, A. Dussaigne, R. Butté, and N. Grandjean, "Homogeneous and inhomogeneous linewidth broadening of single polar GaN/AlN quantum dots", physica status solidi c **6**, S598–S601 (2009).

[158] P. Lefebvre and B. Gayral, "Optical properties of GaN/AlN quantum dots", Comptes Rendus Physique **9**, 816–829 (2008).

[159] M. J. Holmes, K. Choi, S. Kako, M. Arita, and Y. Arakawa, "Room-Temperature Triggered Single Photon Emission from a III- Nitride Site-Controlled Nanowire Quantum Dot", Nano Lett. **14**, 982–986 (2014).

[160] M. Holmes, S. Kako, K. Choi, P. Podemski, M. Arita, and Y. Arakawa, "Measurement of an exciton Rabi rotation in a single GaN/Al_xGa_{1-x}N nanowire-quantum dot using photoluminescence spectroscopy: Evidence for coherent control", Phys. Rev. Lett. **111**, 057401 (2013).

[161] M. Arita, F. Le Roux, M. J. Holmes, S. Kako, and Y. Arakawa, "Ultraclean Single Photon Emission from a GaN Quantum Dot", Nano Letters **17**, 2902–2907 (2017).

[162] Z. Gačević, A. Das, J. Teubert, Y. Kotsar, P. K. Kandaswamy, T. Kehagias, T. Koukoula, P. Komninou, and E. Monroy, "Internal quantum efficiency of III-nitride quantum dot superlattices grown by plasma-assisted molecular-beam epitaxy", Journal of Applied Physics **109**, 103501 (2011).

[163] D. Alden, J. S. Harris, Z. Bryan, J. N. Baker, P. Reddy, S. Mita, G. Callsen, A. Hoffmann, D. L. Irving, R. Collazo, and Z. Sitar, "Point-Defect Nature of the Ultraviolet Absorption Band in AlN", Phys. Rev. Appl. **9**, 054036 (2018).

[164] S. M. Islam, V. Protasenko, K. Lee, S. Rouvimov, J. Verma, H. G. Xing, and D. Jena, "Deep-UV emission at 219 nm from ultrathin MBE GaN/AlN quantum heterostructures", Appl. Phys. Lett. **111**, 091104 (2017).

[165] R. Collazo, J. Xie, B. E. Gaddy, Z. Bryan, R. Kirste, M. Hoffmann, R. Dalmau, B. Moody, Y. Kumagai, T. Nagashima, Y. Kubota, T. Kinoshita, A. Koukitu, D. L. Irving, and Z. Sitar, "On the origin of the 265 nm absorption band in AlN bulk crystals", Applied Physics Letters **100**, 191914 (2012).

[166] T. D. Krauss and J. J. Peterson, "A charge for blinking", Nat. Mater. **11**, 14–16 (2012).

[167] A. L. Efros and D. J. Nesbitt, "Origin and control of blinking in quantum dots", Nat. Nanotechnol. **11**, 661–671 (2016).

[168] K. Kuroda, T. Kuroda, K. Watanabe, T. Mano, G. Kido, N. Koguchi, and K. Sakoda, "Distribution of exciton emission linewidth observed for GaAs quantum dots grown by droplet epitaxy", J. Lumin. **130**, 2390–2393 (2010).

[169] C. H. Kindel, "Study on Optical Polarization in Hexagonal Gallium Nitride Quantum Dots", Ph.D. thesis, The University of Tokyo (2010).

[170] A. Berthelot, I. Favero, G. Cassabois, C. Voisin, C. Delalande, P. Roussignol, R. Ferreira, and J. M. Gérard, "Unconventional motional narrowing in the optical spectrum of a semiconductor quantum dot", Nat. Phys. **2**, 759–764 (2006).

[171] R. Seguin, A. Schliwa, S. Rodt, K. Pötschke, U. W. Pohl, and D. Bimberg, "Size-Dependent Fine-Structure Splitting in Self-Organized InAs/GaAs Quantum Dots", Phys. Rev. Lett. **95**, 257402 (2005).

[172] A. J. Fischer, W. Shan, G. H. Park, J. J. Song, D. S. Kim, D. S. Yee, R. Horning, and B. Goldenberg, "Femtosecond four-wave-mixing studies of nearly homogeneously broadened excitons in GaN", Phys. Rev. B **56**, 1077–1080 (1997).

[173] R. Heitz, I. Mukhametzhanov, O. Stier, A. Madhukar, and D. Bimberg, "Enhanced Polar Exciton-LO-Phonon Interaction in Quantum Dots", Phys. Rev. Lett. **83**, 4654–4657 (1999).

[174] L. Besombes, K. Kheng, L. Marsal, and H. Mariette, "Acoustic phonon broadening mechanism in single quantum dot emission", Phys. Rev. B **63**, 155307 (2001).

[175] C. Becher, A. Kiraz, P. Michler, A. Imamoğlu, W. V. Schoenfeld, P. M. Petroff, L. Zhang, and E. Hu, "Nonclassical radiation from a single self-assembled InAs quantum dot", Phys. Rev. B **63**, 121312 (2001).

[176] S. Kako, M. Miyamura, K. Tachibana, K. Hoshino, and Y. Arakawa, "Size-dependent radiative decay time of excitons in GaN/AlN self-assembled quantum dots", Applied Physics Letters **83**, 984–986 (2003).

[177] M. Fox, Quantum optics: an introduction, volume 15, Oxford University Press (2006).

[178] G. Callsen, "Advanced optical signatures of single, wurtzite GaN quantum dots: From fundamental exciton coupling mechanisms towards tunable photon statistics and hybrid-quasiparticles", Ph.D. thesis, Technischen Universität Berlin (2015).

[179] G. Sallen, A. Tribu, T. Aichele, R. André, L. Besombes, C. Bougerol, M. Richard, S. Tatarenko, K. Kheng, and J.-P. Poizat, "Subnanosecond spectral diffusion measurement using photon correlation", Nat. Photonics **4**, 696–699 (2010).

[180] I. M. Rousseau, "III-Nitride Semiconductor Photonic Nanocavities on Silicon", Ph.D. thesis, Lausanne (2018).

[181] Y. Zhang, W. Liu, and H. Niu, "Native defect properties and p-type doping efficiency in group-IIA doped wurtzite AlN", Phys. Rev. B **77**, 035201 (2008).

[182] Y. Taniyasu, M. Kasu, and T. Makimoto, "An aluminium nitride light-emitting diode with a wavelength of 210 nanometres", Nature **441**, 325–328 (2006).

[183] P. Lodahl, S. Mahmoodian, and S. Stobbe, "Interfacing single photons and single quantum dots with photonic nanostructures", Rev. Mod. Phys. **87**, 347–400 (2015).

[184] A. Strittmatter, A. Holzbecher, A. Schliwa, J.-H. Schulze, D. Quandt, T. D. Germann, A. Dreismann, O. Hitzemann, E. Stock, I. A. Ostapenko, S. Rodt, W. Unrau, U. W. Pohl, A. Hoffmann, D. Bimberg, and V. Haisler, "Site-controlled quantum dot growth on buried oxide stressor layers", Phys. Status Solidi **209**, 2411–2420 (2012).

[185] C. Schneider, M. Strauß, T. Sünner, A. Huggenberger, D. Wiener, S. Reitzenstein, M. Kamp, S. Höfling, and A. Forchel, "Lithographic alignment to site-controlled quantum dots for device integration", Appl. Phys. Lett. **92**, 183101 (2008).

[186] A. Mohan, P. Gallo, M. Felici, B. Dwir, A. Rudra, J. Faist, and E. Kapon, "Record-Low Inhomogeneous Broadening of Site-Controlled Quantum Dots for Nanophotonics", Small **6**, 1268–1272 (2010).

[187] A. Lundskog, C.-W. Hsu, K. Fredrik Karlsson, S. Amloy, D. Nilsson, U. Forsberg, P. Olof Holtz, and E. Janzén, "Direct generation of linearly polarized photon emission with designated orientations from site-controlled InGaN quantum dots", Light Sci. Appl. **3**, e139–e139 (2014).

[188] T. Sugahara, H. Sato, M. Hao, Y. Naoi, S. Kurai, S. Tottori, K. Yamashita, K. Nishino, L. T. Romano, and S. Sakai, "Direct Evidence that Dislocations are Non-Radiative Recombination Centers in GaN", Jpn. J. Appl. Phys. **37**, L398–L400 (1998).

[189] D. Cherns, S. J. Henley, and F. A. Ponce, "Edge and screw dislocations as nonradiative centers in InGaN/GaN quantum well luminescence", Appl. Phys. Lett. **78**, 2691–2693 (2001).

Sebastian Tamariz

Contact Information

Full Name: Sebastian Pascal Tamariz Kaufmann
Date of birth: 23 June 1988
Nationality: Swiss and Mexican
Mailing Address: Ave. de Montoie 37, Lausanne, Switzerland
Phone: (+41) 78 933 86 56
Email: sebastian.tamariz@epfl.ch
Personal email: s.tamariz.k@gmail.com

Education

2015–2019 **Doctorate in Photonics**, *École polytechnique fédérale de Lausanne (EPFL)*, Institute of Physics, Laboratory of Advanced Semiconductors for Photonics and Electronics (LASPE).

2012–2014 **Master in Materials Science and Engineering**, *National Autonomous University of Mexico (UNAM)*, Institute of Materials Research (IIM).
Graduated with Honours

2006–2011 **Bachelor in Physics**, *National Autonomous University of Mexico (UNAM)*, Faculty of Sciences.

PhD Thesis

Title GaN Quantum Dots for Room Temperature Excitonic Physics

Master's Thesis

Title *Ab initio* calculation of electronic properties of the amorphous and crystalline alloy of Gallium, Aluminium and Nitrogen (Al_x Ga_{1-x} N).

Bachelor's Thesis

Title Deposition and photoacoustic characterization of Yttrium Iron Garnet (YIG) thin films.

Publications

- **S. Tamariz**, G. Callsen, N. Grandejan *Density control of GaN quantum dots on AlN single crystal*, Applied Physics Letters **114**, 082101 (2019)
- **S. Tamariz**, G. Callsen, J. Stachurski, K. Shojiki, N. Grandjean *Dynamics of GaN QDs as single photon emitters at room temperature* – in preparation
- **S. Tamariz**, G. Callsen, J. Stachurski, A. Schliwa, N. Grandjean *High order exitonic complexes in GaN QDs* – in preparation
- K. Shojiki, **S. Tamariz**, G. Callsen, N. Grandjean *Position-controlled GaN nanostructures embedded in AlN films grown on Si substrate* – in preparation
- **S. Tamariz**, D. Martin, N. Grandjean *AlN grown on Si (1 1 1) by ammonia-molecular beam epitaxy in the 900-1200 °C temperature range*, Journal of Crystal Growth, **476**, 58, (2017)
- **S. P. Tamariz-Kaufmann**, A. A. Valladares, A. Valladares and R. M. Valladares. *First-principles calculation of the electronic and topological properties of crystalline and amorphous* $Al_xGa_{1-x}N$, Journal of Non-Crystalline Solids, **420**, 7, (2015)

Interests

Nanoscale semiconductor materials and devices

Electronic structure and quantum physics

III-Nitride photonic and electronic technologies

Skills

Experimental	Molecular Beam Epitaxy, Photoluminescence, micro-Photoluminescence, Cathodoluminescence, Atomic Force Microscopy, Scanning Electron Microscopy, Pulsed Laser Deposition, Sputtering, X-ray diffraction
Computational	Materials Studio, OriginLab, DMol^3, Mathematica, FORTRAN, MATLAB, Adobe Illustrator, MS Office suite

Language Skills

Spanish	**Mother tongue**
English	**Near native**
French	**Fluent**
German	**Intermediate**

Teaching Experience

2010 - present	Teaching assistant for undergraduate physics courses

References

- *Prof.* Nicolas Grandjean, Institute of Physics (IPHYS), École polytechnique fédérale de Lausanne (EPFL)
  email: nicolas.grandjean@epfl.ch
- *Prof.* Ariel A. Valladares, Institute in Materials Research (IIM), National Autonomous University of Mexico (UNAM).
  email: valladar@unam.mx
- *Prof.* Rosalba Castañeda, Center for Applied Science and Technological Development (CCADET), National Autonomous University of Mexico (UNAM).
  email: rosalba.castaneda@ccadet.unam.mx

**Ce document a été imprimé au Centre d'impression EPFL,
imprimerie climatiquement neutre, certifiée myClimate.**